UNIVERSIDADE FEDERAL DE SÃO CARLOS

CENTRO DE CIÊNCIAS EXATAS E TECNOLÓGICAS

PROGRAMA DE PÓS-GRADUAÇÃO EM FÍSICA

RAMAN SPECTROSCOPY AS A RELIABLE TOOL FOR STRAIN ANALYSIS IN III-NITRIDE SUPERLATTICES

FERNANDO MAIA DE OLIVEIRA

ORIENTADOR: DR. MARCIO DALDIN TEODORO

Setembro de 2021

UNIVERSIDADE FEDERAL DE SÃO CARLOS

CENTRO DE CIÊNCIAS EXATAS E TECNOLÓGICAS

PROGRAMA DE PÓS-GRADUAÇÃO EM FÍSICA

RAMAN SPECTROSCOPY AS A RELIABLE TOOL FOR STRAIN ANALYSIS IN III-NITRIDE SUPERLATTICES

FERNANDO MAIA DE OLIVEIRA

Tese submetida ao Programa de Pós-Graduação em Física da Universidade Federal de São Carlos como parte dos requisitos para a obtenção do título de Doutor em Física.

ORIENTADOR: DR. MARCIO DALDIN TEODORO

Setembro de 2021

UNIVERSIDADE FEDERAL DE SÃO CARLOS

Centro de Ciências Exatas e de Tecnologia
Programa de Pós-Graduação em Física

Folha de Aprovação

Defesa de Tese de Doutorado do candidato Fernando Maia de Oliveira, realizada em 02/09/2021.

Comissão Julgadora:

Prof. Dr. Márcio Daldin Teodoro (UFSCar)

Prof. Dr. Angelo Malachias de Souza (UFMG)

Prof. Dr. Jose Pedro Rino (UFSCar)

Prof. Dr. Carlos Luis Trallero Giner (UConn)

Prof. Dr. Ariano de Giovanni Rodrigues (UFSCar)

O presente trabalho foi realizado com apoio da Coordenação de Aperfeiçoamento de Pessoal de Nível Superior - Brasil (CAPES) - Código de Financiamento 001.

O Relatório de Defesa assinado pelos membros da Comissão Julgadora encontra-se arquivado junto ao Programa de Pós-Graduação em Física.

Acknowledgements

To Prof. Dr. Marcio Daldin Teodoro, for accepting me in his amazing research group, for his excellent orientation even in times of pandemic, and for the incredible opportunities he has managed to happen for his students.

To Prof. Dr. Yuriy Mazur, for receiving me in his laboratory, for his supervision and for promoting an environment of growth and development of new skills.

To Dr. Andrian Kuchuk for performing the XRD analysis, for fundamental discussions and for his constantly updated set of references.

To Prof. Dr. Morgan Ware, the academic great-grandson of Raman, for the training on micro-Raman spectroscopy.

To Dr. Pjush Gosh for growing the superlattices used in this study and for introducing me to the world of MBE.

To Dr. Mourad Benamara for acquiring the TEM and EDS data, and allowing me to access his laboratory for sample preparation.

To Dr. Hryhorii Stanchu for the training on sample preparation for TEM.

To Dr. Gregory Salamo and Ms. Emily Ebbing for opening the doors of science for so many international students and researchers.

To the financial support of Conselho Nacional de Desenvolvimento Científico e Tecnológico (CNPq), process code 141000/2017-1; Coordenação de Aperfeiçoamento de Pessoal de Nível Superior – Brasil (CAPES) – Finance Code 001, process code 88881.361801/2019-01; and University of Arkansas.

To my family and all the colleagues and friends I have made along the way.

And thank you to the committee members for promptly accepting to evaluate and contribute to this study.

Resumo

Desde a sua descoberta, o efeito Raman tem sido um ótimo aliado na investigação estrutural de uma ampla variedade de materiais, da macro à nanoescala. Entretanto, apesar da incrível sensibilidade de técnicas baseadas em desvio Raman em detectar características associadas à vibrações atômicas, um limite de acurácia em resultados é imposta pela imprecisão em determinar os parâmetros associados ao método tradicional de interpretação de desvios Raman. Nesta formulação, uma associação linear é considerada entre a tensão estrutural sentida pelo material e o desvio Raman, cuja dependência é definida por um conjunto de potenciais de deformação e constantes elásticas que possuem valores específicos para o material em análise, dependendo por exemplo de sua simetria cristalina. Esta tese de doutorado apresenta um método alternativo para realizar com maior precisão a análise de tensão estrutural em nanoestruturas usando desvio Raman. Para isso, seis superredes de 30 períodos de AlN e GaN foram fabricadas usando a técnica de epitaxia por feixes moleculares assitida por plasma, definindo diferentes espessuras de GaN entre amostras distintas. As superredes foram analisadas por difração de raio x, apresentando uma distribuição de tensões planares distensiva e compressiva. Usando microscopia óptica, um mosaico de fraturas foi observado promovendo a redução da tensão distensiva em partes das estrutras. O desvio Raman foi adquirido em diferentes posições de cada superrede, sendo então usado na calibração de um modelo de correlação linear baseado no fenômeno de coerência de rede com resultados de difração de raio x. Usando o modelo não linear a técnica de micro-Raman foi empregada para realizar o mapeamento uni- e bidimensional das superredes, evidenciando a distribuição de valores de tensões ao redor das linhas de fraturas estruturais. Uma dependência da tensão sentida em relação à distância de linas de fratura foi também verificada, exibindo um valor de tensão residual aproximadamente constante após alguns micrômetros da linha de fratura. Os valores máximos e mínimos das tensões planares distensiva em camadas de AlN e compressiva em camadas de GaN são também dependentes da espessura de GaN empregada em cada superrede. Esta interpretação alternativa do desvio Raman permite não só a aquisição de valores mais precisos de tensão estrutrural em superredes, mas apresenta também aplicabilidade para uma ampla gama de heteroestruturas em nanoescala.

Palavras-chave: Efeito Raman, Superrrede, Nitreto de Gálio, Nitreto de Alumínio.

Abstract

Since its discovery, the Raman effect has been a great ally in the structural investigation of a wide variety of materials, from macro to nanoscale. However, despite the remarkable sensitivity of techniques based on Raman shift in detecting features associated to atomic vibrations, a limit of accuracy in results is imposed by the imprecision in determining the parameters associated to the traditional method of interpretation of Raman shift. In this formulation, a linear association is considered between strain and Raman shift, which dependency is defined by a set of deformation potentials and elastic constants that have specific values for the material in analysis, depending for instance on its crystalline symmetry. This doctoral thesis presents an alternative method for performing more accurately strain analysis of nanostructures using Raman shift. To do so, a set of six 30-period AlN/GaN were fabricated using plasma-assisted molecular beam epitaxy, defining different thickness of GaN among distinct samples. The superlattices were analyzed by x-ray diffraction, displaying a distribution of in-plane tensile and compressive strain. By using optical microscopy, a mosaic of cracks was observed promoting the reduction of tensile strain in parts of the structure. The Raman shift was acquired in different positions of each superlattice, and then used to calibrate a nonlinear correlation model based on the phenomenon of lattice coherence with results from x-ray diffraction. Using the nonlinear model, the technique of micro-Raman was employed to perform one- and two-dimensional strain mappings of the superlattices, evidencing the distribution of values of strain around the lines of structural cracks. A strain dependence with the distance to cracks was also verified, exhibiting an approximately constant value of residual strain after a few micrometers apart from any line of crack. The maximum and minimum values of in-plane tensile strain in the layers of AlN and in-plane compressive strain in the layers of GaN are also dependent on the thickness of GaN employed in each superlattice. This alternative interpretation of Raman shift allows not only the acquisition of more precise values of strain for nitrides superlattices, but it also shows applicability for a wide range of heterostructures in nanoscale.

Keywords: Raman effect, Superlattice, Gallium Nitride, Aluminum Nitride.

Contents

List of Figures

List of Tables

List of Abbreviations and Symbols

Å ..... Angstrom

a_i ..... Deformation potential

a_{xx} ..... In-plane lattice constant

b_i ..... Deformation potential

$Ammonia - MBE$ ..... Ammonia Assisted Molecular Beam Epitaxy

AlN ..... Aluminum Nitride

A_1 ..... Polar mode with symmetry A

c ..... Epitaxial lattice constant

C_{ij} ..... Elastic constant

EDS ..... Energy-Dispersive X-Ray Spectroscopy

E_1 ..... Polar mode with symmetry E

E_2^{High} ..... High frequency nonpolar mode with symmetry E

E_2^{Low} ..... Low frequency nonpolar mode with symmetry E

GaN ..... Gallium Nitride

InN ..... Indium Nitride

K ..... Proportionality constant

LO ..... Longitudinal Optical

MBE ..... Molecular Beam Epitaxy

min ..... Minute

N ..... Nitrogen

nm ..... Nanometer

$PAMBE$ ..... Plasma Assisted Molecular Beam Epitaxy

PL ..... Photoluminescence Spectroscopy

R ..... Mechanical/vibrational ratio

s ..... Second

TEM ..... Transmission Electron Microscopy

TO ..... Transversal Optical

XRD ..... X-Ray Diffration

α ..... Polarizability

ϵ ..... Strain

ε ..... Dielectric Constant

ω_0 ..... Unstrained Raman mode

Chapter 1: Introduction

The mechanical description of nanomaterials is imperative for elaborating reliable devices in the semiconductor industry. Strain, as a key feature to be determined when evaluating structural integrity, has its information usually accessed by measuring deformations promoted by a stressed condition. In this context, the Raman effect can be used to quantify changes in atomic vibrations in response to stress, and using a correlation model, the Raman shift can be used to investigate strain. In particular, the micro-Raman technique represents a suitable tool to study the distribution of strain in the micrometric spatial scale. However, the imprecision in determining each elastic constant used in the traditional linear interpretation of Raman shift limits the accuracy of strain analyses. Therefore, by developing a nonlinear model in the light of the Raman effect assuming harmonic approximation, this doctoral thesis presents an alternative method for studying in-plane strain distribution in nanostructures at microscale.

1.1 Objectives

This research aims to provide a reliable tool to perform strain analysis of nanostructures at microscale. To do so, the following goals were set:

- Succeed in growing a set of six 30-period AlN/GaN superlattices with different thicknesses of GaN.
- Measure the thicknesses, in-plane lattice constant and strain in AlN and GaN layers of each superlattice using x-ray diffraction.
- Track the atomic vibrational modes in AlN and GaN layers of each superlattice using Raman spectroscopy.
- Compare the in-plane strain calculated using the standard linear interpretation of Raman shift with strain values acquired by x-ray diffraction.
- Formulate a correlation model in the scope of harmonic approximation to describe in-plane strain based on a nonlinear dependence on Raman shift.
- Evaluate the model's reliability in describing results reported in references from the literature.
- Use the nonlinear model to perform one- and two-dimensional strain mapping of superlattices at microscale.

1.2 Text structure

In order to provide a clear view of this research, by describing the topics covered, methodologies used and results achieved during its complete development, the main text of this doctoral thesis is organized as follows: in $Chapter\ 2$, a review about Raman effect in III-nitrides is presented, considering also fundamental aspects of the theory of elasticity applied to crystals with hexagonal symmetry; in $Chapter\ 3$, the fabrication and characteristics of III-nitride superlattices is discussed, highlighting interesting properties of these materials. The phenomenon of lattice coherence is then evaluated in the case of AlN/GaN superlattices, also considering mechanisms of stress relief in nanostructures; in $Chapter\ 4$, the experimental details concerning the growth of the set of superlattices investigated in this study is presented, as well as a brief description about each experimental technique; in $Chapter\ 5$, the results of this research are reported, leading to the elaboration, test and application of an alternative method for studying in-plane strain distribution in nanostructures at microscale.

Chapter 2: Raman effect in III-nitride semiconductors

This chapter presents a review about Raman effect in III-nitrides, covering fundamental aspects of the theory of elasticity in the case of crystals with hexagonal symmetry. The origin of different modes of atomic vibration are discussed, as well as their applicability in the mechanical and electrical studies of materials.

2.1 Raman effect

The interaction between light and matter has always enlightened the curious minds of scientists through the last centuries. In 1869, while studying the presence of contaminants in air, the Irish physicist John Tyndall evidenced the change in the color of white light when shining it through an enclosed gas medium.[1,2] Two years later, this effect was mathematically described by the British scientist John William Strutt, known as Lord Rayleigh, when explaining the colors of the sky as a result of polarized sunlight scattering in the atmosphere.[2] In 1887, the German physicist Heinrich Rudolf Hertz evidenced the change in voltage measured in solid metal electrodes when illuminating them with ultraviolet light, which would much later be known as the photoelectric effect.[3] In 1922, while studying X-ray radiation, the American physicist Arthur Compton discovered that the characteristics of the radiation, such

as its wavelength and frequency, could be changed by the light interacting with free electrons.[4] The description of this phenomenon, namely Compton effect, was assured by considering photons as small packages of light interacting inelastically with electrons, which existence had been brough to public attention only a few decades earlier thanks to the work of the British scientist Joseph John Thomson.[5] At that time, the advances in the understanding of light polarization in terms of environment features, such as the refractive index of the medium, were also supported by the mathematical framework of the Scottish scientist James Clerk Maxwell from decades earlier.[6] However, some natural phenomena presumably associated with light scattering were still unclear while based only on an elastic point of view of interactions. As an example, in 1928 after wondering about the origin of the color of the sea by considering the spectral role played by water molecules while contesting Lord Rayleigh's version of a simple reflection of the sky, the Indian physicist Chandrasekhara Venkata Raman set up a series of experiments to analyze the characteristics of light scattering in different media.[7] Raman evidenced that some small portion of the light was scattered as a different color, while most of the light remained unchanged, which lead him to envision an optical cause most likely resemblant to the inelastic Compton effect. Described by Raman as a new type of secondary radiation, this effect was not limited to liquids, being surprisingly evidenced in a large variety of materials, such as gases, crystals and even amorphous solids.[7] The origin of such phenomenon was initially attributed to molecular agitation, which apparent isotropic optical behavior was supposed to be free of polarized restraints, commonly associated with well oriented crystalline solids. For his extensive investigations on scattered light leading to the discovering of this new effect, Raman was awarded with the Nobel Prize in Physics in 1930.[7]

The experimental visualization of the effect was also independently reported by Russian physicists in the same year using crystals, and the theoretical prediction of an inelastic scattering of photons had been previously reported by the Austrian physicist Adolf Smekal.[8] In a parallel to the Compton effect, Smekal considered the restriction imposed by momentum conservation to the interaction of matter and radiation, suggesting that there would be a quantum of energy exchanged between the atom or molecule and the incident photon. In his approach, the frequency of the scattered radiation would be either lower, in the case the atom or molecule is receiving an amount of energy during the event of interaction with light, or higher, if the atom or molecule is less energetic than its initial state. In 1934, a theoretical study on Raman scattering based on the polarizability of molecules was published by the Czech physicist George Placzek.[9] His study considered the mechanical approach in the understanding

of the origin of fluorescence elaborated by the Irish mathematician and physicist George Gabriel Stokes, taking into account the exchange of energy during the oscillation of atoms and molecules.[10] The deviation in frequency of the scattered light to lower values would generate spectral lines known as Stokes lines, meaning that an exchange of energy had occurred from the light to the atomic or molecular system. On the other way, if the scattered light presented a higher frequency than its initial value, this process would produce spectral lines known as anti-Stokes lines, which origin comes from the exchange of energy from the atomic or molecular system to the light. In 1933, while investigating molecular absorbance and fluorescence the Polish physicist Aleksander Jablonski created a schematic diagram in order to represent the transition between energetic states during events of fluorescence.[11,12] Figure 1 presents the correspondent Jablonski diagram for events of Raman and Rayleigh scattering.

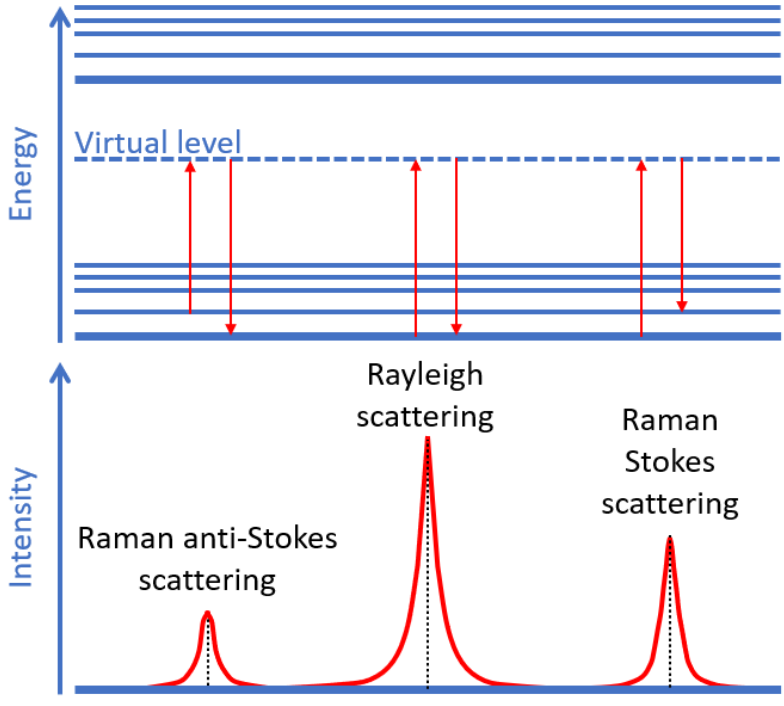

Figure 1 - Jablonski diagram for events of Raman anti-Stokes scattering, Raman Stokes scattering and Rayleigh scattering.

In the diagram, each energy level is represented by a horizontal line, and the higher the location of the line, the higher is its value of energy. The most intense curve characterizes the elastic event of Rayleigh scattering. Here the molecule is excited by the incident light from its ground state to a virtual level, which a priori have undefined energy once they are not represented by eigenfunctions of the Hamiltonian of the molecular system.[12] The molecule then relaxes to its ground state emitting a photon of same energy as the incident radiation. The inelastic process

of Stokes scattering, represented by a medium intensity curve in the diagram, involves the molecule being excited from its ground state to a virtual state, followed by the molecule relaxation to a vibrational level above its ground state. In this case some amount of energy was in the end of the process accumulated by the molecule, that emits a photon which is less energetic than the incident radiation. And the inelastic process of anti-Stokes scattering, represented by the low intensity curve in the diagram, involves the molecule being initially already excited at a vibrational level that is energetically situated above its ground state, previously to the interaction with the radiation. The molecule is then excited to a virtual level by the incident light and in the process of deexcitation instead of returning to its original vibrational state, the molecule relaxes to its ground state emitting a photon which is more energetic than the incident radiation. The curves shown in the diagram are not in scale once the inelastic scattering is far less intense than the elastic events.[13,14] Considering that the Raman effect takes place in only a small portion of the scattered light when compared to the more probable Rayleigh scattering, once roughly an inelastic event happens to one every a million scattered photons, and that the system is supposed to be free of the action of external events, such as fire and strong magnetic fields, then an even smaller part of the inelastic scattered radiation should present a higher energy than its initial state, once just a few molecules were vibrationally excited prior to the light excitation.[12,15] For this reason, when acquiring the Raman spectrum of a material, it was very clear that Stokes lines were most likely to be spectrally more intense and easier to analyze than anti-Stokes lines, which sometimes were insufficiently weak to overcome the signal-to-noise ratio that is intrinsic to the detection limit of the equipment.[12] In a nonspontaneous approach, the anti-Stokes lines can be magnified by exciting the material using light which frequency is chosen in a way that a resonance between excitation and a specific molecular vibration is achieved.[15] The investigation of Stokes lines generated in a spontaneous event of Raman scattering is therefore simpler and efficient enough to allow the study of a wide range of materials.

The classical theory of Raman scattering considers the scattered light as produced by an induced electric dipole, whose oscillation is modulated by the electric field of the incident radiation. The concept of molecular electric dipoles was elaborated in 1912 by the Dutch scientist Peter Joseph William Debye in his investigations about the distribution of charges in asymmetric molecules.[16] His studies considered aspects of the electric environment of the separated charges, such as their dielectric character and also the temperature of the medium. In his honor, the debye unit D is universally used as unit of dipole moment, and it is equivalent

to $c^{-1}10^{-21}\ Cm^2/s$, where c is the speed of light in vacuum.[16] Debye's theory was fundamentally influenced by the model of quantized lattice vibrations reported in 1907 by the German physicist Albert Einstein.[17] In his work, the atomic oscillations are declared responsible for determining the thermal behavior of materials, such as their specific heat. The energy of these vibrations was postulated to be quantized, similarly to the optical analog photons also reported by Einstein only two years earlier in 1905.[18] These quantized lattice vibrations received the name phonons in 1930 by the Russian physicist Yakov Frenkel.[19] Considering a diatomic system of charges $+q$ and $-q$ exhibiting an oscillatory displacement Δx and separated by a distance d as shown in Figure 2, its dipole moment $\vec{\mu}$ can be defined as:

$$\vec{\mu} = q\vec{d}$$

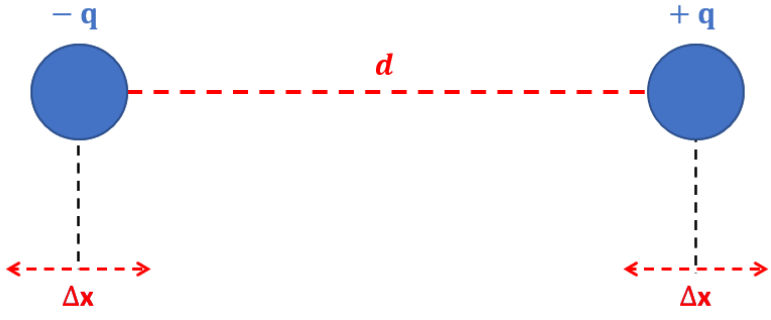

Figure 2 - Two oscillating charges separated by a distance d.

The spatial separation of charges in a molecule allows its susceptibility to the electric field of an incoming radiation.[12,20] Even materials with no permanent asymmetric charge distribution can be affected by the electric field if their polarizability is capable of assuming different values over time, such as during a displacement of its charge centers.[20,21] In this case, the material's mode of oscillation is considered Raman active, once its instantaneous dipole moment changes during vibrations. If an oscillation of the multiatomic system does not represents change in its polarizability, then this material's mode of oscillation would be considered Raman inactive. The frequency ν of vibration of an electric dipole is related to its dipole moment $\vec{\mu}$ during a time t by:

$$\vec{\mu} = \vec{\mu}_0 \cos(2\pi\nu t)$$

Here, $\vec{\mu}_0$ is the amplitude of dipole moment and $\vec{\mu}$ is the resulting vector taken as the difference between the system's instantaneous and permanent dipole moments.[21] The incident radiation's electric field shifts the local charge centers in opposite directions, which incites and modulates

the time-dependent values of spontaneous charge displacement. The induced dipole moment, which represents its instantaneous values and directions over time, can be described as explicitly conditional to the incident radiation's electric field by:

$$\vec{\mu} = \vec{\vec{\alpha}} \otimes \vec{E}$$

Here, $\vec{E}$ represents the electric field of the incident radiation and $\vec{\vec{\alpha}}$ is a second rank tensor that symbolizes the electric polarizability, which reflects how flexible and malleable is the charge distribution within the molecular system.[21] The second rank order is required because there are two independent spatial directions being considered during the event of interaction between light and matter: the incoming time-dependent electric field has its defined direction for each incident photon; and the oscillatory dipole has its own defined direction along which its moment of electric dipole is oscillating. These two directions can be controlled by using polarizers in order to select the proper direction of incident and scattered light, as well as by rotating the material under analysis.[22,23] Mathematically, the polarizability associated to the phenomenon of spontaneous Raman scattering is considered symmetric ($\alpha_{ij} = \alpha_{ji}$, $i,j = x,y,z$), leading the electric field to act upon the six resulting independent terms ($\alpha_{xx}, \alpha_{yy}, \alpha_{zz}, \alpha_{xy}, \alpha_{yz}, \alpha_{zx}$). This is exceptionally not held valid for nonspontaneous resonant Raman events. Each element of polarizability can be expanded as a Taylor series in terms of normal coordinates r_k, harmonically defined by $r_k = (r_k)_0 \cos(2\pi\nu_k t)$ which simplifies the mechanical description of instantaneous charge displacements under independent modes of oscillation, and whose dependence is given by:

$$\alpha_{ij} = (\alpha_{ij})_0 + \sum_k \left(\frac{\partial \alpha_{ij}}{\partial r_k}\right)_0 r_k + \cdots$$

In this relation, the expansion is taken until the kth coordinate and the system is considered under equilibrium.[24] The assumption of minor displacements leads to negligible terms of higher order, therefore, the time-dependent electric field $\vec{E} = \vec{E}_0 \cos(2\pi\nu_0 t)$ will result in a dipole moment which magnitude is given by:

$$|\vec{\mu}| = \alpha_0 E_0 \cos(2\pi\nu_0 t) + \frac{1}{2}\left(\frac{\partial \alpha}{\partial r_k}\right)_0 (r_k)_0 E_0 \{\cos[2\pi(\nu_0 - \nu_k)t] + \cos(2\pi(\nu_0 + \nu_k)t)\}$$

This expression makes clear that three different frequencies are coexistent in the oscillatory system: the first (ν_0) generates Rayleigh elastic scatterings exhibiting the same wavelength as

the incident light; the second $(\nu_0 - \nu_k)$ produces Stokes lines due to inelastic scattering, which wavelength is larger than that of the incident light; and the third $(\nu_0 + \nu_k)$ generates anti-Stokes lines exhibiting smaller wavelength than the incident light.[20,25]

Besides being affect by light, the atomic oscillations are also modulated by its natural modes of vibrations, which are intrinsically dependent on the masses and force constants associated to the atomic bonding strength, type of bonding and spatial configuration.[25,26] Classically, an electric dipole can be seen as a mechanical harmonic oscillator, which charge displacement is affected by the time dependent electric field of the incident radiation. In the 17th century, the English scientist Robert Hooke postulated the fundamental principles that reign the mechanical behavior of elastic systems.[27] His description of the laws of elasticity laid the ground for studies on strain and stress, which are of the utmost importance when investigating atomic and molecular vibrations. Hooke's investigations, a priori, were devoted to the analysis of unidimensional deformation in springs submitted to loads. His findings lead to the assumption of apparent linearity between applied load and structural deformation, whose relation would be controlled by a proportionality constant, or elastic constant k, characteristic for the system and described by:

$$\vec{F}_{el} = -k\vec{x}$$

Here, the applied force $\vec{F}_{el}$ promotes an antiparallel deformation $\vec{x}$.[27,28] This expression represents a first order approximation of a more complex and general mechanical behavior respecting the elastic limits of rupture of the material, where the elastic behavior is still prevalent. Beyond those limits the structure would face irreversible processes, such as the formation of cracks, which eventually leads to the material's rupture, entering in a regime called plastic behavior where the linear elastic formulation is no longer valid.[29,30] Also in the 17th century, the English scientist Isaac Newton postulated the laws governing the motion of bodies, considering the forces these bodies are being submitted to.[28] Since the publication, his studies guaranteed the development of innumerable technologies, whose applications go beyond the scope of mechanics of macroscale rigid bodies. In special, his second law of motion relates the rate of change of a body's momentum according to the applied force, as described by:

$$\vec{F} = \frac{d}{dt}(m\vec{v})$$

Here, the momentum $\vec{p}$ is explicitly shown as the product between the body's mass m and speed $\vec{v}$.[28] Hooke's and Newton's theories are both fundamental in the understanding of atomic and molecular oscillations, and therefore they are essential for describing the mechanical aspects of Raman scattering events. Considering a diatomic system of oscillating charge centers $+q$ and $-q$, exhibiting masses m_1 and m_2 separated by a distance d at equilibrium, the application of a force $\vec{F}_{el}$ originated in the system's interaction with the incoming radiation's electric field would promote a displacement $\vec{x}$ along the direction defined by the system's induced electric dipole $\vec{\mu}$.[12,28] The resulting change in momentum evidenced in the system due to the oscillation can be expressed by:

$$\vec{F} = m\frac{d^2}{dt^2}[\vec{x}(t)] = -k\vec{x}(t)$$

In this expression, $m = [(m_1^{-1})^{-1} + (m_2^{-1})^{-1}]^{-1}$ is the system's reduced mass and k is its force constant. The use of a reduced mass simplifies the mathematical treatment by condensing the analysis of two separate bodies into a single diatomic system. The time dependence of displacement can be therefore defined by solving the second order differential equation:

$$\frac{d^2}{dt^2}[\vec{x}(t)] + \frac{k}{m}\vec{x}(t) = 0$$

A general oscillatory solution in the form $\vec{x}(t) = x_0\cos(\omega t + \varphi_0)\hat{\jmath}$ can be used, where $\omega = 2\pi\nu$ represents the angular frequency of oscillation, φ_0 is an arbitrary phase and $\hat{\jmath}$ is the unit vector along the direction of oscillation.[28] The effect of mass m and force constant k to the angular frequency ω can be evidenced by taking the second derivative of the proposed solution:

$$\frac{d^2}{dt^2}[\vec{x}(t)] = -\omega^2 x_0\cos(\omega t + \varphi_0)\hat{\jmath} = -\omega^2\vec{x}(t) \therefore \omega = \sqrt{\frac{k}{m}}$$

This expression can be used to illustrate the mass-dependent behavior observed when analyzing vibrational modes of different isotopes from the same element. Heavier isotopes present more neutrons in their nucleus than lighter isotopes, and this extra mass leads to a slower frequency of vibration.[26] The force constant k of a diatomic molecule is associated to its bond strength, which is strictly dependent on the number of electrons in the bonding. Therefore, the shift in the light's frequency due to the Raman effect, known as Raman shift, is

dependent on the mass of each atom and also on the type of bonding that holds the molecule united.[20,25]

Due to the small deviation commonly observed in the scattered light's energy during events of Raman scattering, it is useful to employ a more sensitive unit of energy which variation highlights the changing details within a small range of energy scale. This unit, called reciprocal centimeter (cm^{-1}), can be fundamentally related to the electron-volt unit (eV) by:

$$1eV = \frac{e}{100hc}\, cm^{-1}$$

In this relation, the constant $e = 1.602\ x\ 10^{-19}\ C$ is the elementary electric charge, $h = 6.626\ x\ 10^{-34}\ m^2Kg/s$ is the Planck's constant and $c = 299792458\ m/s$ is the speed of light in vacuum.[12] Therefore, a change as small as $0.1\ meV$ in the energy of the scattered light would result in a Raman shift in the order of $1\ cm^{-1}$. When measured in reciprocal centimeters this quantity is known as wavenumber $\tilde{\nu} = \nu/c$, in contrast to the radiation's wavelength $\lambda = c/\nu$ which is usually described in units of meters, such as nanometers in the case of a radiation in the visible spectral range. The wavenumber scale indicates how many complete wave cycles occur in the space of one centimeter.[12]

It is interesting to note that the Raman shift evidenced in the experiment corresponds to a spectral deviation from the incident light's initial energy.[20] As an example, the calibration of many systems of Raman spectroscopy is made by evaluating the Raman shift exhibited by a known material used as a reference, such as an unstrained substrate of silicon, according to the excitation of an arbitrary laser. So, if the laser initially presents a red wavelength of $632.8\ nm$, such as helium-neon lasers, and after the interaction with the substrate of silicon part of its wavelength is redshifted to $654.3\ nm$ as a result from a process of Raman scattering, then a characteristic vibrational mode of silicon will be evidenced displaying high intensity in the wavenumber of approximately $520.7\ cm^{-1}$, as expected for one of the specific vibrations between atoms of silicon (Si-Si).[31] Using a different laser for excitation, such as a neodymium-doped laser whose emission happens in the green wavelength of $532\ nm$, the same vibrational mode would be observed in the wavenumber of $520.7\ cm^{-1}$, but in this case the scattered light would present a wavelength of $547.2\ nm$, representing a redshift of only $15\ nm$, which is a smaller deviation than the $22\ nm$ evidenced with a helium-neon laser. The different wavelength values of redshifts observed for distinct lasers can be mathematically justified by the fact that the difference between the inverse of two quantities is not the same for any pair of

quantities, once the inverse function does not change linearly over its argument. Physically, despite two distinct excitation radiations being transferring the same amount of energy to the oscillatory system during an event of Stokes scattering, in this case approximately $65\ meV$, leading to the same shift in wavenumbers perceived experimentally, this reduced amount of energy does not lead to the same variation in wavelength because the variation in the light's wavelength does not change linearly with its corresponding energy due to their inverse proportionality scaled by the speed of light.[20,21]

The analogy between the Raman effect and an oscillating dipole also evidences the fact that the Raman intensity is dependent on the wavelength of the incident radiation. Considering the radiation emitted by an electric dipole, the Raman scattering intensity can be specified by the following relation:[21]

$$I_{Raman} = \frac{h(\nu_0 - \nu_i)^4}{8\pi^2 c\nu_i\left(1 - e^{-\frac{hc\nu_i}{kT}}\right)}\left(45{a_i}^2 + 7{b_i}^2\right) \therefore\ I_{Raman} \propto {\lambda_0}^{-4}$$

Here, ν_0 represents the frequency of the incident radiation and λ_0 its wavelength, ν_i is a fundamental vibrational frequency at a temperature T, c is the speed of light and a_i and b_i are parameters associated with transitions between vibrational states.[20,21,25] Alternative expressions can be used to explicit another appropriate dependences, such as the incident light's excitation intensity.[20] Furthermore, due to its exponentially thermal character, the ratio between scattering intensities originated from Stokes and anti-Stokes events allows the thermometric study of a material's temperature.[32] The scattering intensity depends on the fourth power of the incident light's frequency ν_0, which means that the dependence with the incident light's wavelength λ_0 will be inversely proportional to its fourth power, once the radiation's frequency and wavelength are reciprocally related by $c = \lambda\nu$. Therefore, the shorter the wavelength of the incident radiation, the higher is its energy and also the greater is the number of scattered photons that go through a spontaneous process of Raman interaction with the atomic system.[20,21] In the case of nonspontaneous Raman events, such as when a particular wavelength of excitation coincides with its correspondent specific value of energy for a molecular vibration in the material, the Raman intensity increases displaying values even higher than if using more energetic excitation sources.[15,21] This process is called resonance enhancement and it allows a great advantage in sensitivity when investigating very small concentrations of compounds, such as the detection of certain substances in another material.[15,33]

Many developments in the study of the Raman effect were achieved in the decades following Raman's Nobel laureate award ceremony, in the fields of technique, theory and applications, and more than 700 publications about the effect were issued in the first 7 years of its discovery.[34,35] Several investigations were devoted to the identification and understanding of molecular structures, allowing scientists to obtain information about their vibrational behavior. The applicability and universality of the Raman effect was extended well beyond the scope of spectroscopic physics, reaching scientific and commercial areas of chemistry, geology, biology and medical studies, among others.[35] In 1998, in recognition to its unnumerable uses and fundamental nature, the Raman effect was honorably acknowledged as an International Historical Chemical Landmark by the Indian Association for Cultivation of Science and the American Chemical Society.[34]

2.2 Theory of elasticity for hexagonal symmetry

The vibrational behavior of a multiatomic system is intrinsically determined by its number and type of atoms, how these atoms are distributed, and which type of chemical bonding is keeping the system under a stable configuration.[25,36] External factors, such as temperature[32], pressure[37] and presence of external electromagnetic fields[38] also have influence in events of molecular vibration. For crystals of any geometry, the allowed modes of vibration with each neighboring atom are defined by the atomic disposition within the structure, as well as their bonding strength and angles.[36] The forces acting on each atom that constitutes the material, such as the interaction felt by sharing electrons, a local oscillation due to thermal excitation or even a resonance with incident electric or magnetic fields, will all eventually lead to directional stresses that propagate along the material.[25,39,40] In 1807, roughly a hundred years after Robert Hooke's description of the laws that reign the elastic behavior of linear systems, the British scientist Thomas Young showed that solid bodies followed similar mechanical laws.[41] Whilst investigating the applicability of Hooke's law in higher-dimensional media, Young considered the mechanical relation between stress and strain in the understanding of stiffness and deformation of three-dimensional solid materials stablishing the so called generalized Hooke's law.[41] Precedingly to Young, the idea of a relation between the surface pressure felt by a body and its consequent volume deformation had been brought up to public attention by the Swiss scientist Leonhard Euler, in his works on critical loads and structural stability.[42] The mechanical stress σ is defined by the local force felt by a body per unit of its

area where the force is being applied, and it is measured in pascals $P = kgm^{-1}s^{-2}$ that represents a unit of pressure; on the other hand, the mechanical strain ϵ is associated to the body's deformation in response to its stressed condition, and it is defined by the change in its size as a result from the applied force, compared to its initial relaxed state, being therefore unitless once it represents a rational relative displacement from its original form. In his lectures[41], Young classified the seven basic structural effects a body can be submitted to: compression (there is a force causing the reduction of the body's size), extension (a force causes the enlargement of the body's size), torsion (there are forces twisting the body), flexure (three or more forces are bending the body), detrusion (transverse forces are applied on a fixed position on the body, comparable to a scissoring movement), alteration (forces promote a permanent deformation that might lead to sedimentation) and rupture (the permanent separation of parts of the body caused by forces overcoming its strength limits).[28,41] The structural effects of compression and extension can be studied under similar mechanic laws once the directional stress and the consequent size reduction or enlargement are felt parallel to the applied force. The material's resistance to structural modification is strictly dependent on its elasticity, defined by Young as the body's passive strength, which is also responsible for defining the limits of its structural rupture. Rotational modifications, such as torsion, flexure and detrusion require additional angular considerations once the applied forces produce shear stresses along the material.[41] Therefore, it is important to highlight the distinction between normal stresses, which act towards or opposite to the surface where the force is being applied; and shear stresses, which occur alongside to the surface of the material. Earthquakes are great examples of stresses being relieved at the Earth's crust. The horizontal movement of tectonic plates eventually leads to structural faults, originating local multidirectional stresses and matter displacement. As an example, the North American Plate and the Pacific Plate are moving alongside each other leading to a constant situation of shear stress at the coastline of California, on the other hand the Eurasian Plate and the Indian Plate are moving towards each other, promoting a condition of normal stress across China.[43,44] Mathematically, stress is represented by a second rank tensor $\vec{\vec{\sigma}}$, once its nature is dependent on the directions of both force and surface where the force is being applied. Each one of its elements $\sigma_{i,j}$ is associated to one possible relative orientation established between the normal vector $\vec{n}$ directed outwards the surface, and the resulting force $\vec{F}$. In Young's theory, in order to consider the infinitesimal stress contributions on every fragment of volume of a material, the generalized Hooke's law developed by Young takes into account the assumed three-dimensional freedom faced by a

stressed body on its way to release such tension.[27,41,45] A priori, his theory neglects secondary effects that might restrict the material's movement and eventual transformation, assuming also that there is compositional homogeneity along all the volumetric structure. Despite the apparent simplicity, the generalized Hooke's law has found innumerable applications in solving engineering problems throughout the centuries.[27] Considering a system metrically described by cartesian coordinates, a unitary fragment of a material can be represented by an elemental cube, which infinitesimal dimensions are defined by vectors according to their projections on the $\hat{x}$, $\hat{y}$, $\hat{z}$ axes, as shown in Figure 3.[46]

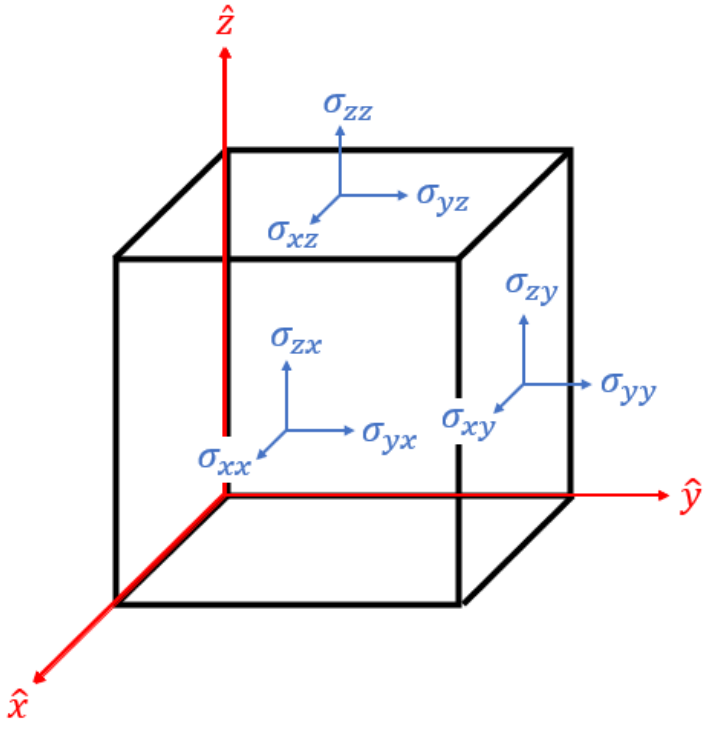

Figure 3 - Components of stress.

In the figure, the elements of stress represented by σ_{ij} symbolize the components $\sigma_{i,j}$ acting along the direction $\hat{\imath}$ on the surface which normal vector is defined along the direction $\hat{\jmath}$. As an example, the element $\sigma_{z,y}$ is acting along the $\hat{z}$ direction on the surface which normal is defined towards the $\hat{y}$ direction, while the element $\sigma_{x,y}$ is acting along the $\hat{x}$ direction on the same surface. Therefore, the balance among the elements $\sigma_{i,j}$ determines the resulting movement of the body.[46] In special, the nonequilibrium condition between $\sigma_{i,j}$ and $\sigma_{j,i}$ determines the rotational movement of the body; meanwhile the elements $\sigma_{i,j}$ for all $i = j$ are associated with movements of compression and extension resulted from normal stresses; and elements $\sigma_{i,j}$ for

$i \neq j$ are responsible for the presence of shear stresses. Under these considerations, it is useful to assume the symmetry $\sigma_{i,j} = \sigma_{j,i}$ in order to neglect movements of rotation once it simplifies the mechanical description for cases of tensile stress and compressive stress.[46] Therefore, in this case there are in total six components of stress to be considered: three associated to normal stresses ($\sigma_{x,x}$, $\sigma_{y,y}$ and $\sigma_{z,z}$), and three responsible for shear stresses ($\sigma_{x,y}$, $\sigma_{y,z}$ and $\sigma_{z,x}$). Each component can be seen as a local pressure caused by a resulting force, which acts on each portion of the body's volume. In matrix notation, the explicit components of the total stress for a three-dimensional system can be expressed as:

$$\overleftrightarrow{\sigma} = \begin{bmatrix} \sigma_{xx} & \sigma_{xy} & \sigma_{xz} \\ \sigma_{yx} & \sigma_{yy} & \sigma_{yz} \\ \sigma_{zx} & \sigma_{zy} & \sigma_{zz} \end{bmatrix}$$

The consequent change in the body's size as a result from the force being applied can be defined by elemental displacements along each axis.[46,47] A priori, the modification in the body's size happens only when the distance between two or more positions within the body vary. This condition is illustrated as a two-dimensional diagram in Figure 4, that represents the movement of two points A and B within the material.

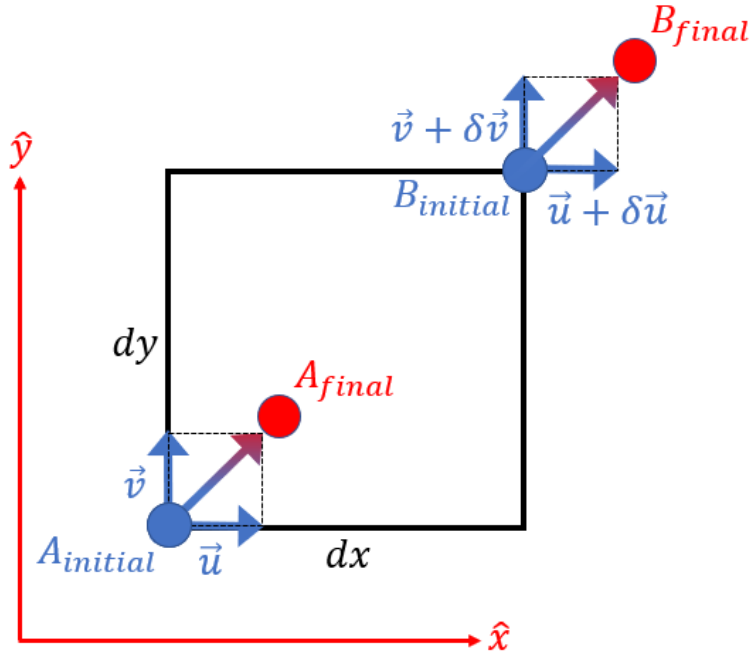

Figure 4 - Displacement of two points A and B within a body.

In this system, under the effect of an external force, the point A within the body is displaced from its initial position $A_{initial}$ to a final position A_{final}, traveling a distance given by the

module of the displacement vector $\vec{r}_A = \vec{u} + \vec{v}$. As a consequence, another arbitrary point B within the body will be moved from its initial position $B_{initial}$, firstly located $\sqrt{(dx)^2 + (dy)^2}$ away from point A, to its final position at B_{final}, according to its displacement vector defined by $\vec{r}_B = \vec{u} + \delta\vec{u} + \vec{v} + \delta\vec{v}$. In this vector, the components $\delta\vec{u}$ and $\delta\vec{v}$ represent the occurrence of deformation. Here, the condition of change in size defines that in the situation that $\delta\vec{u} + \delta\vec{v} = 0$, then there will be no modifications in the material's dimensions as a result of the application of a force.[28,46] In this case, once $\delta\vec{u}$ and $\delta\vec{v}$ are perpendicular to each other due to the right angle between its unitary vectors defined along the axes $\hat{x}$ and $\hat{y}$ and therefore there are no components of $\delta\vec{u}$ and $\delta\vec{v}$ that share the same axis, then the only case for no change in size is when both $\delta\vec{u}$ and $\delta\vec{v}$ are null vectors, which represents a movement of translation without deformation.[28,46] Considering a three-dimensional system, its vector position for an elemental unit of volume is given by $\vec{r} = x\hat{\imath} + y\hat{\jmath} + z\hat{k}$. When a particular point within the system is moved to $\vec{r} = (x+u)\hat{\imath} + (y+v)\hat{\jmath} + (z+w)\hat{k}$, where $\vec{t} = u\hat{\imath} + v\hat{\jmath} + w\hat{k}$ refers to the vector of translation, the elements of the resulting deformation $\delta\vec{r} = dx\hat{\imath} + dy\hat{\jmath} + dz\hat{k}$ in every direction according to the displacement $\delta\vec{t}$ can be obtained by:

$$\delta u = \vec{\nabla}u \cdot \delta\vec{\mathrm{r}} = \left(\frac{\partial}{\partial x}\hat{\imath} + \frac{\partial}{\partial y}\hat{\jmath} + \frac{\partial}{\partial z}\hat{k}\right)u \cdot \left(dx\hat{\imath} + dy\hat{\jmath} + dz\hat{k}\right) = \frac{\partial u}{\partial x}dx + \frac{\partial u}{\partial y}dy + \frac{\partial u}{\partial z}dz$$

$$\delta v = \vec{\nabla}v \cdot \delta\vec{\mathrm{r}} = \left(\frac{\partial}{\partial x}\hat{\imath} + \frac{\partial}{\partial y}\hat{\jmath} + \frac{\partial}{\partial z}\hat{k}\right)v \cdot \left(dx\hat{\imath} + dy\hat{\jmath} + dz\hat{k}\right) = \frac{\partial v}{\partial x}dx + \frac{\partial v}{\partial y}dy + \frac{\partial v}{\partial z}dz$$

$$\delta w = \vec{\nabla}w \cdot \delta\vec{\mathrm{r}} = \left(\frac{\partial}{\partial x}\hat{\imath} + \frac{\partial}{\partial y}\hat{\jmath} + \frac{\partial}{\partial z}\hat{k}\right)w \cdot \left(dx\hat{\imath} + dy\hat{\jmath} + dz\hat{k}\right) = \frac{\partial w}{\partial x}dx + \frac{\partial w}{\partial y}dy + \frac{\partial w}{\partial z}dz$$

In this relation, it was considered the orthogonality of the unit vectors ($\hat{\imath} \perp \hat{\jmath} \perp \hat{k}$) leading to vanishing scalar products between elements defined along different axes.[46] Therefore, by defining strain $\overleftrightarrow{\epsilon}$ as the variation in size according to the material's original configuration, the multidirectional total strain can be expressed as:[40]

$$\overleftrightarrow{\epsilon} = \left[\frac{\partial u}{\partial x}\right]_{\hat{\imath},\hat{\imath}} + \left[\frac{\partial u}{\partial y}\right]_{\hat{\imath},\hat{\jmath}} + \left[\frac{\partial u}{\partial z}\right]_{\hat{\imath},\hat{k}} + \left[\frac{\partial v}{\partial x}\right]_{\hat{\jmath},\hat{\imath}} + \left[\frac{\partial v}{\partial y}\right]_{\hat{\jmath},\hat{\jmath}} + \left[\frac{\partial v}{\partial z}\right]_{\hat{\jmath},\hat{k}} + \left[\frac{\partial w}{\partial x}\right]_{\hat{k},\hat{\imath}} + \left[\frac{\partial w}{\partial y}\right]_{\hat{k},\hat{\jmath}} + \left[\frac{\partial w}{\partial z}\right]_{\hat{k},\hat{k}}$$

In matrix notation, the components of the total strain can be defined by:

$$\overleftrightarrow{\epsilon} = \begin{bmatrix} \epsilon_{xx} & \epsilon_{xy} & \epsilon_{xz} \\ \epsilon_{yx} & \epsilon_{yy} & \epsilon_{yz} \\ \epsilon_{zx} & \epsilon_{zy} & \epsilon_{zz} \end{bmatrix}$$

Or alternatively, using a vectorial notation developed by the physicist Woldemar Voigt in the 19th century, the total three-dimensional strain can be expressed as:[25,48]

$$\epsilon = \begin{bmatrix} \epsilon_{xx} \\ \epsilon_{yy} \\ \epsilon_{zz} \\ 2\epsilon_{yz} \\ 2\epsilon_{zx} \\ 2\epsilon_{xy} \end{bmatrix}$$

The components $\epsilon_{i,j}$ of normal strain can then be obtained by:

$$\epsilon_{xx} = \frac{\partial u}{\partial x};\ \epsilon_{yy} = \frac{\partial v}{\partial y};\ \epsilon_{zz} = \frac{\partial w}{\partial z}$$

Likewise, the components of shear strain can be expressed by:

$$\epsilon_{xy} = \frac{\partial v}{\partial x} + \frac{\partial u}{\partial y};\ \epsilon_{yz} = \frac{\partial w}{\partial y} + \frac{\partial v}{\partial z};\ \epsilon_{zx} = \frac{\partial u}{\partial z} + \frac{\partial w}{\partial x}$$

The relation between stress $\overleftrightarrow{\sigma}$ and strain $\overleftarrow{\epsilon}$ evidenced by Young for small displacements allows the expression of the total stress associated to every direction within a system.[25,28] It results from a combination of the material's elements of strain according to a proportionality constant, known as elastic constant, which is strictly dependent on the considered directions for every element of strain. The elastic constant is defined by a fourth rank tensor $\overleftrightarrow{C}$ known as stiffness tensor, therefore the generalized Hooke's law can then be expressed by:[49]

$$\sigma_{ij} = C_{ijkl}\epsilon_{kl}$$

A fourth order notation is required once the elastic behavior of a general solid material is considered prevalently anisotropic, unless otherwise defined in the case of specific symmetric conditions.[28] It means that mechanical features such as the speed of sound in a material and its piezoelectricity are directionally dependent on the elastic character of the medium that constitutes the material.[28] The total amount of 81 possible combinations for the subindexes of C_{ijkl} can be reduced considering the symmetries of ϵ_{ij} and σ_{ij}, which leads to: $C_{ijkl} = C_{ijlk} = C_{jikl} = C_{jilk}$.[48,50–53] In matrix notation, the elements of elastic constant that define the stiffness tensor for a material in cartesian coordinates can then be expressed as:

$$\overleftrightarrow{C} = \begin{bmatrix} C_{xxxx} & C_{xxyy} & C_{xxzz} & C_{xxyz} & C_{xxzx} & C_{xxxy} \\ C_{yyxx} & C_{yyyy} & C_{yyzz} & C_{yyyz} & C_{yyzx} & C_{yyxy} \\ C_{zzxx} & C_{zzyy} & C_{zzzz} & C_{zzyz} & C_{zzzx} & C_{zzxy} \\ C_{yzxx} & C_{yzyy} & C_{yzzz} & C_{yzyz} & C_{yzzx} & C_{yzxy} \\ C_{zxxx} & C_{zxyy} & C_{zxzz} & C_{zxyz} & C_{zxzx} & C_{zxxy} \\ C_{xyxx} & C_{xyyy} & C_{xyzz} & C_{xyyz} & C_{xyzx} & C_{xyxy} \end{bmatrix}$$

Here, in the elements C_{ijkl} the subindexes ij are associated to the directions of stress, meaning that the stress is acting along the direction $\hat{\imath}$ on the surface whose normal vector is defined along the direction $\hat{\jmath}$. Additionally, the subindexes kl are related to the directions of strain considering the variation in the material's dimension along the $\hat{k}$ and $\hat{l}$ directions. Using a reduced tensorial notation by defining the identities $xx \equiv 1$, $yy \equiv 2$, $zz \equiv 3$, $yz \equiv 4$, $zx \equiv 5$, $xy \equiv 6$ to express in a simpler way the 36 elements of the elastic constant for a solid body, the matrix notation of the stiffness tensor becomes:[48,49]

$$\overleftrightarrow{C} = \begin{bmatrix} C_{11} & C_{12} & C_{13} & C_{14} & C_{15} & C_{16} \\ C_{21} & C_{22} & C_{23} & C_{24} & C_{25} & C_{26} \\ C_{31} & C_{32} & C_{33} & C_{34} & C_{35} & C_{36} \\ C_{41} & C_{42} & C_{43} & C_{44} & C_{45} & C_{46} \\ C_{51} & C_{52} & C_{53} & C_{54} & C_{55} & C_{56} \\ C_{61} & C_{62} & C_{63} & C_{64} & C_{65} & C_{66} \end{bmatrix}$$

Therefore, by applying the reduced notation the generalized Hooke's law can then be written as:

$$\sigma_i = C_{ij}\epsilon_j \,, \qquad i,j = \{xx, yy, zz, yz, zx, xy\}$$

As a reciprocal analog to the relation defined by the fourth rank elastic stiffness tensor $\overleftrightarrow{C}$ between stress and strain, the fourth rank elastic compliance tensor $\overleftrightarrow{S}$ establishes the relation between strain and stress.[46,48,54] The generalized Hooke's law considering the elastic compliance becomes:

$$\epsilon_i = S_{ij}\sigma_j\,, \qquad i,j = \{xx, yy, zz, yz, zx, xy\}$$

The elements S_{ij} of compliance can be obtained from the elastic constants C_{ij} of stiffness by using the transformation given by:

$$S_{ij} = (-1)^{i+j}\frac{det\left[\overleftrightarrow{C}\right]\Big|_{i,j}}{det\left[\overleftrightarrow{C}\right]}$$

Here, the element S_{ij} of compliance is obtained by suppressing the row i and column j of the original stiffness tensor $\overleftrightarrow{C}$, taking the determinant and dividing it by the original determinant of the stiffness tensor. If the total amount of $i + j$ is an even number the resulting ratio keeps its sign, otherwise the sign is reversed. Basically, this method calculates the inverse element S_{ij} that corresponds to the original matrix which elements are given by C_{ij}.[49]

The symmetry of crystalline solids simplifies their elastic description by reducing the number of independent terms required for their stiffness and compliance tensors.[49,55,56] In special, the geometrical character of a crystal can be evaluated according to three operations of symmetry: rotation (1-fold to 6-fold rotations), inversion (1-fold to 6-fold inversions) and reflection (mirroring). In crystals there are 32 possible combinations of symmetry operations, each one of them defining one group of crystal class with its specific properties of symmetry.[55,56] In order to classify all the possible crystalline scenarios, the German scientist Carl Hermann and the French scientist Charles-Victor Mauguin elaborated a system of identification of symmetry operations, which was recognized in 1935 as part of the International Tables for Crystallography and it is known as the Hermann-Mauguin notation.[57] For example, a rectangular solid has 3 perpendicular mirror planes, 3 perpendicular axes of 2-fold rotation and 1 center of symmetry, which are all characteristics of a class known as rhombic-dipyramidal, such as the mineral topaz.[58,59] Every three-dimensional macroscopic crystal preserves the geometric information of its fundamental building blocks, defined as unit cell, and by propagating its unit cell periodically over a length of space, the crystal can be built. According to the shape of crystalline structures they can be classified in six different crystal families: triclinic (irregular lengths of axes and different angles between them), monoclinic (irregular lengths of axes and two right angles between axes), orthorhombic (irregular lengths of axes and all the axes are mutually perpendicular to each other), tetragonal (two axes of equal length and all the axes are mutually perpendicular to each other), hexagonal (three axes of

equal length at an angle of 120 degrees between each other and all these three axes are perpendicular to a fourth axis) and isometric (all axes have equal length and equal angles between them).[59,60] Therefore, the knowledge of the symmetry group at which a crystal belongs allows the simplification of its mechanical description by reducing the number of independent elastic constants required to describe many of its directional dependent properties.[60] In particular, due to its high abundancy in Earth's crust and outstanding performance in electronic systems, the semiconductor silicon has been extensively explored in several industries, assuming a strong presence in the world economy. The mineral silicon has a highly symmetrical crystalline geometry, known as diamond cubic, in which the atomic arrangement of the same element follows a repeating pattern of same lengths and angles, belonging to the isometric family of crystals.[59] Other examples of cubic crystals are the semiconductors germanium and gallium arsenide, that just like silicon, due to their high symmetry their stiffness tensor is formed by only three independent terms (C_{11}, C_{12} and C_{44}) instead of thirty-six.[59] This simplicity of representation allows to express all the non-null terms as a function of the independent constants, as is shown in the reduced matrix form of the generalized Hooke's law for these semiconductors:[59]

$$\begin{bmatrix} \sigma_{xx} \\ \sigma_{yy} \\ \sigma_{zz} \\ \sigma_{yz} \\ \sigma_{zx} \\ \sigma_{xy} \end{bmatrix} = \begin{bmatrix} C_{11} & C_{12} & C_{12} & 0 & 0 & 0 \\ C_{12} & C_{11} & C_{12} & 0 & 0 & 0 \\ C_{12} & C_{12} & C_{11} & 0 & 0 & 0 \\ 0 & 0 & 0 & C_{44} & 0 & 0 \\ 0 & 0 & 0 & 0 & C_{44} & 0 \\ 0 & 0 & 0 & 0 & 0 & C_{44} \end{bmatrix} \begin{bmatrix} \epsilon_{xx} \\ \epsilon_{yy} \\ \epsilon_{zz} \\ 2\epsilon_{yz} \\ 2\epsilon_{zx} \\ 2\epsilon_{xy} \end{bmatrix}$$

The current limitations of efficiency faced in the development of technologies based on silicon, such as the viable miniaturization of circuits considering its atomic size and the stability at high temperatures, it all leads scientists to envision materials to be used in the next generation of powerful devices.[61] Hexagonal crystals formed by elements of the families III-V of the periodic table, such as gallium nitride, aluminum nitride and indium nitride have displayed remarkable features in innumerable and diverse applications, going from deep ultraviolet light emitting diodes until high efficiency battery chargers.[62,63] These semiconductors can also be found in their cubic form, known as zinc blend structure, which geometrically differs from the hexagonal arrangement, known as wurtzite structure, fundamentally by the stacking sequence

of atomic planes.[64–67] The following diagram in Figure 5 presents a comparison between the atomic configurations of a cubic zinc blend structure and a hexagonal wurtzite structure for a semiconductor nitride, such as gallium nitride:[65–67]

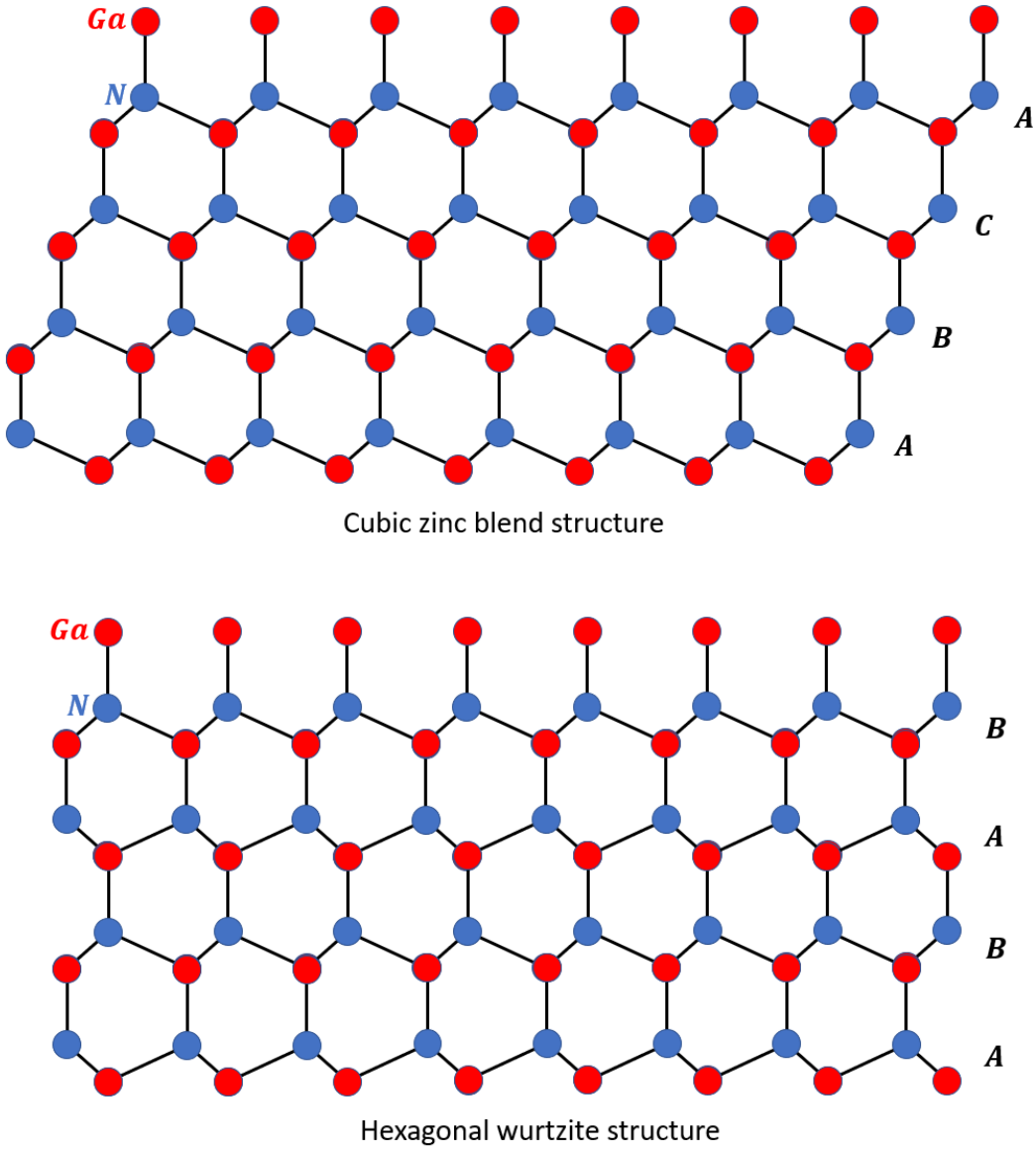

Figure 5 - Comparison between the cubic zinc blende structure and the hexagonal wurtzite structure of gallium nitride, exhibiting the atomic stacking pattern for each case: $A-B-C-A-\cdots$ for the cubic structure, and $A-B-A-B-\cdots$ for the hexagonal structure.

In both structures the atoms of gallium could be replaced by any other group-III atom in the representation of another III-V compound. For either cubic or hexagonal structures each group-III atom is tetrahedrally coordinated with four atoms of nitrogen, as well as each nitrogen atom is coordinated with four group-III atoms.[68] In the cubic structure each atomic layer is repeated

every four layers ($\boldsymbol{A}-B-C-\boldsymbol{A}-B-C-\boldsymbol{A}-\cdots$) along the cubic direction $[111]$. On the other hand, in hexagonal structures each atomic layer repeats itself every three layers ($\boldsymbol{A}-B-\boldsymbol{A}-B-\boldsymbol{A}-\cdots$) along the hexagonal direction $[0001]$.[65] This distinctive pattern of atomic planes disposition has its origin in the symmetric character of tetrahedral coordination. For wurtzite III-nitride crystals with hexagonal symmetry, each tetrahedron formed by a central group-III atom and four atoms of nitrogen at the extremities is symmetrically inter-coordinated with another tetrahedron constituted by a central atom of nitrogen surrounded by four group-III atoms.[65,69] Therefore, for hexagonal crystals there is a mirroring symmetry for alternating atoms between layers A and B. Cubic crystals do not exhibit this reflective character between every consecutive atomic layer, once the pair of layers A and B, as well as the pairs B and C, and C and A, exhibit tetrahedrons that are antisymmetrically coordinated with each other.[70] This can be seen in the following diagram in Figure 6 for each structural case of gallium nitride:[65,69,71]

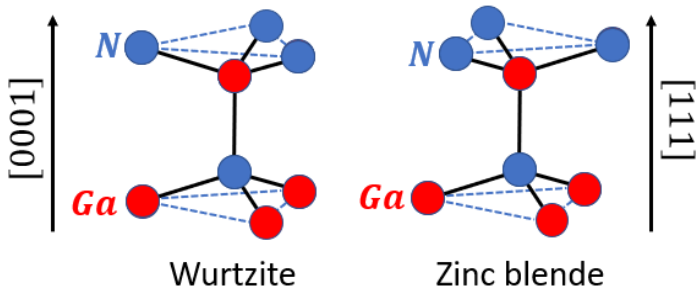

Figure 6 - Atomic coordination in wurtzite and zinc blend structures of gallium nitride.

In the case of crystals with hexagonal geometry, the stiffness tensor can be represented by five independent elements of elastic constant: C_{11}, C_{12}, C_{13}, C_{33} and C_{44}, instead of thirty-six.[55,56] In the reduced notation, the generalized Hooke's law for hexagonal crystals is expressed by:[72]

$$\begin{bmatrix}\sigma_{xx}\\ \sigma_{yy}\\ \sigma_{zz}\\ \sigma_{yz}\\ \sigma_{zx}\\ \sigma_{xy}\end{bmatrix}=\begin{bmatrix}C_{11} & C_{12} & C_{13} & 0 & 0 & 0\\ C_{12} & C_{11} & C_{13} & 0 & 0 & 0\\ C_{13} & C_{13} & C_{33} & 0 & 0 & 0\\ 0 & 0 & 0 & C_{44} & 0 & 0\\ 0 & 0 & 0 & 0 & C_{44} & 0\\ 0 & 0 & 0 & 0 & 0 & \frac{C_{11}-C_{12}}{2}\end{bmatrix}\begin{bmatrix}\epsilon_{xx}\\ \epsilon_{yy}\\ \epsilon_{zz}\\ 2\epsilon_{yz}\\ 2\epsilon_{zx}\\ 2\epsilon_{xy}\end{bmatrix}$$

The stiffness tensor of a material determines how it mechanically responds to structural events, such as actions of tensioning, stretching and bending.[55,72] The deformational behavior of a material can be investigated by its stress-strain curve, that represents a very useful tool in solving engineering problems. In particular, two characteristic regimes can be evidenced: the first one is the elastic regime, which is characterized by the material deforming according to the linear Hooke's law of deformation, meaning that the deformation increases linearly with the magnitude of the force applied on the material.[28,73] The second regime is known as plastic regime, and it starts when the magnitude of the applied force is more than enough to produce irreversible deformations on the material, which resulting deformation no longer can be stablished using a linear dependence.[28] Figure 7 exemplifies the engineering stress-strain curve of a solid body, indicating particular moments during the deformation of a material before its eventual rupture:[74,75]

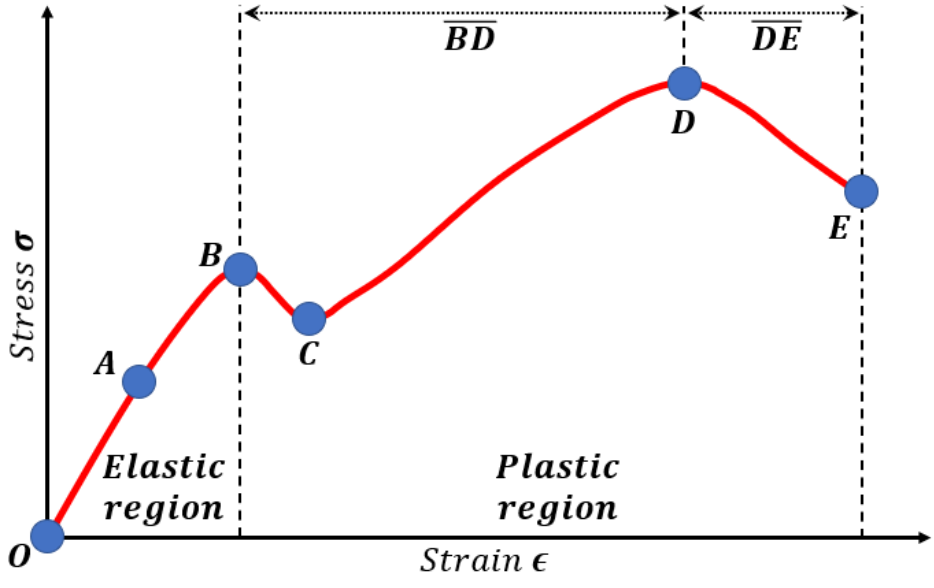

Figure 7 - Example of a stress-strain curve of a solid body, indicating the stages of: O (point of initial application of force), A (point of elastic limit), B (upper yield limit), C (lower yield stress point), BD (strain hardening), D (ultimate stress point), DE (necking), E (limit of rupture).

In the stress-strain curve, the linear proportionality between stress and strain is evidenced from the moment when the force is starting to be applied on the material (O) until the point of elastic limit (A). After the elastic limit, any additional stress causes irreversible deformations in the material. In the upper yield limit (B) the material suffers a permanent deformation, usually

about 0.2% of its original size, officially entering in the regime of plastic behavior.[30] The lower yield stress point (C) defines the minimum stress required to hold the material's deformation. The ultimate stress point (D) is the maximum amount of stress a body can safely withstand before starting an eventual situation of fracture. During the plastic regime the material suffers an irreversible strengthening defined by the region of strain hardening ($\overline{BD}$). During the necking phase ($\overline{DE}$) the material's cross-sectional area starts to shrink leading to an apparent decrease in stress before the material's rupture. The area under the stress-strain curve represents the stored strain energy density during an interval of deformation, and can be expressed by:[29,30]

$$Area = \frac{1}{2}\sigma\epsilon$$

By considering the volume Ω_0 of a single unit cell of a crystal, in cartesian coordinates the strain energy U is defined by:[12]

$$U = \frac{1}{2}\Omega_0 \sum_{i,j} \sigma_{i,j}\epsilon_{i,j}$$

For simplification when in the eventuality of shear stresses, the components of strain can be represented as parameters $e_1 = \epsilon_{xx}$, $e_2 = \epsilon_{yy}$, $e_3 = \epsilon_{zz}$, $e_4 = 2\epsilon_{yz}$, $e_5 = 2\epsilon_{zx}$, $e_6 = 2\epsilon_{xy}$. Therefore, for hexagonal crystals the generalized Hooke's law becomes:[48]

$$\begin{bmatrix}\sigma_1\\ \sigma_2\\ \sigma_3\\ \sigma_4\\ \sigma_5\\ \sigma_6\end{bmatrix} = \begin{bmatrix} C_{11} & C_{12} & C_{13} & 0 & 0 & 0 \\ C_{12} & C_{11} & C_{13} & 0 & 0 & 0 \\ C_{13} & C_{13} & C_{33} & 0 & 0 & 0 \\ 0 & 0 & 0 & C_{44} & 0 & 0 \\ 0 & 0 & 0 & 0 & C_{44} & 0 \\ 0 & 0 & 0 & 0 & 0 & \frac{C_{11}-C_{12}}{2} \end{bmatrix} \begin{bmatrix} e_1\\ e_2\\ e_3\\ e_4\\ e_5\\ e_6 \end{bmatrix}$$

In this representation the components of stress $\sigma_{i,j}$ were also defined using Voigt's reduced notation. Therefore, the strain energy can be expressed as:[46,48]

$$U = \frac{1}{2}\Omega_0 \begin{bmatrix} \sigma_1 \\ \sigma_2 \\ \sigma_3 \\ \sigma_4 \\ \sigma_5 \\ \sigma_6 \end{bmatrix} [e_1 \quad e_2 \quad e_3 \quad e_4 \quad e_5 \quad e_6]$$

$$\therefore$$

$$U = \frac{1}{2}\Omega_0 \left[C_{11}{e_1}^2 + C_{11}{e_2}^2 + C_{33}{e_3}^2 + C_{44}{e_4}^2 + C_{44}{e_5}^2 + \frac{1}{2}(C_{11} - C_{12}){e_6}^2 + 2C_{12}e_1e_2 + 2C_{13}e_1e_3 + 2C_{13}e_2e_3 \right]$$

The slope of the stress-strain curve represents the modulus of elasticity of the material, also known as Young's modulus E, that quantifies how easily strain can be developed in the material under stress, and it is defined by:[12,46]

$$E = \frac{\sigma_{ij}}{\epsilon_{ij}}, \qquad i = j$$

As a function of the Young's modulus, the density of strain energy can be expressed by:[45]

$$\frac{U}{V} = \frac{\sigma^2}{2E}$$

The shear stiffness of a material can be expressed by its shear modulus G, which represents the ratio between the shear stress and shear strain of a material:[12,28]

$$G = \frac{\sigma_{ij}}{\epsilon_{ij}}, \qquad i \neq j$$

The relation between the variation in pressure of a body in respect to its change in volume is denominated bulk modulus B, and it can be expressed as:[12,28,76]

$$B = -V\frac{dP}{dV}$$

Using the elastic constants of the stiffness tensor for hexagonal crystals in Voigt's reduced notation, the bulk modulus can be expressed by:[52]

$$B = \frac{C_{33}(C_{11} + C_{12}) - 2(C_{13})^2}{C_{11} + C_{12} - 4C_{13} + 2C_{33}}$$

The relative deformation of a material in the direction perpendicular to the applied stress can be evidenced by the ratio between the transverse and longitudinal strains. This quantity is known as Poisson's ratio ν of the material, and it is defined as:[77]

$$\nu = -\frac{d\epsilon_i}{d\epsilon_j}, \qquad i \perp j$$

Due to their direct dependence with the relation between strain and stress for any class of materials, the Young's modulus E, the bulk modulus B, the shear modulus G and the Poisson's ratio ν constitute a very useful set of elastic parameters that allows to characterize the elastic behavior of a mechanical system.[28,50,51,72]

2.3 Atomic vibrations in wurtzite crystals

The symmetry and periodicity of geometric figures have always stood out as recurrent subjects for works of arts and sciences. In the ancient Mediterranean, the fascination for frequent shapes found in the nature and the necessity of measure standardization in fields such as astronomy, architecture and manufacturing production, lead the Greek mathematician Euclid of Alexandria to develop the first official mathematical framework of geometry.[78] His treatise entitled "The Elements" that covers the foundation for axiomatic systems, theorems and postulates, originally published in 300 B.C., had been a required textbook in several universities until the 20th century, laying the ground for innumerable studies associated to the symmetry properties of bodies and systems.[78] Particularly, the repetitive pattern evidenced in the art of filling a plane using figures without leaving gaps, which process is known as tessellation, had found considerable attention in 1891 by the works of the Russian crystallographer Evgraf Fedorov.[79] Fedorov elaborated the mathematical proof that there are exactly 17 distinct groups of planar symmetries, also called the two-dimensional wallpaper groups, that obey the isometry operations of Euclidean planes, given by: translation (symmetrical by spatial displacement), rotation (symmetrical under revolution), reflection (symmetrical by mirroring) and glide reflection (symmetrical by displacing and mirroring).[78,80] As an example, the hexagonal tiling evidenced in honeycomb cells belongs to the wallpaper group named $p6m$, that among other properties has isometry of rotation occurring at angles

multiples of 60 degrees, which can also be observed in the graphene structure, in basalt columns and in the eyes of arthropods.[81] As an expansion from the two-dimensional conjecture of symmetries, Fedorov determined also the 230 space groups in three-dimensional systems, which are used to geometrically describe all possible crystal symmetries.[82] Each element of a space group can be assembled by the translational symmetry of its unit cell, which contains all the overall symmetry configurations displayed by the whole crystal. In special, there are 27 space groups associated to hexagonal crystals, and among them the group $C_{6v}^{4}(P6_3mc)$ defines the symmetry properties of wurtzite crystals, such as the hexagonal form of semiconductor nitrides.[83] In this group's name, the classification C_{6v}^{4} uses a notation developed by the German mathematician Arthur Moritz Schoenflies and it means that the elements of this group exhibit a 6-fold rotation axis with 6 vertical mirror planes containing the axes.[59] Additionally, the classification $P6_3mc$ uses the Hermann-Mauguin notation, evidencing that the crystal has a 6-fold screw rotation which axis is defined along the hexagonal direction $[0001]$ parallel to its lattice parameter c with a family of mirror planes which normal is $\{100\}$, and also a family of glide planes which normal is $\{120\}$.[59] In wurtzite crystals, this atomic distribution can be considered as formed by the interpenetration of two hexagonal close packed lattices that exhibit parallel c-axes, which are spatially displaced from each other. In group-III nitrides, one of the lattices is constituted by group-III atoms surrounded by four atoms of nitrogen, while the other interpenetrating lattice is constituted by nitrogen atoms surrounded by four group-III atoms.[60,84] Using Cartesian three-dimensional coordinates with the unitary vector $\hat{a}$ defined along the y-axis, the distance between two basis atoms of each lattice, such as each distinct central atoms in different tetrahedrons, is given by the vector $\vec{r} = \frac{2}{3}\vec{a}_1 + \frac{1}{3}\vec{a}_2 + \frac{1}{2}\vec{a}_3$, where $|\vec{a}_1| = |a \cdot \hat{a}_1| = a$ and $|\vec{a}_2| = |a \cdot \hat{a}_2| = a$, with a being the basal lattice parameter and $\hat{a}_1$ and $\hat{a}_2$ the unitary vectors defined at $\frac{2\pi}{3}$ radians apart along the basal plane, and $|\vec{a}_3| = |c \cdot \hat{a}_3| = c$, with c being the axial lattice parameter and $\hat{a}_3$ the unitary vector perpendicular to the basal plane and parallel to the hexagonal $[0001]$ direction.[85–87] In this configuration, the volume occupied by a single atom is defined by $V_{hcp} = \frac{\sqrt{3}}{4}a^2c$, and ideally, the distance represented by the modulus of the vector $\vec{r}$, given by $|\vec{r}| = \left|\frac{2}{3}\vec{a}_1 + \frac{1}{3}\vec{a}_2 + \frac{1}{2}\vec{a}_3\right|$, is equivalent to one complete length of basal lattice parameter a.[88] As displayed in Figure 8 for the case of gallium nitride, hexagonal group-III nitrides have four atoms per unit cell coordinated tetrahedrally by polar covalent bonds in sp^3 hybridized orbitals.[85,89]

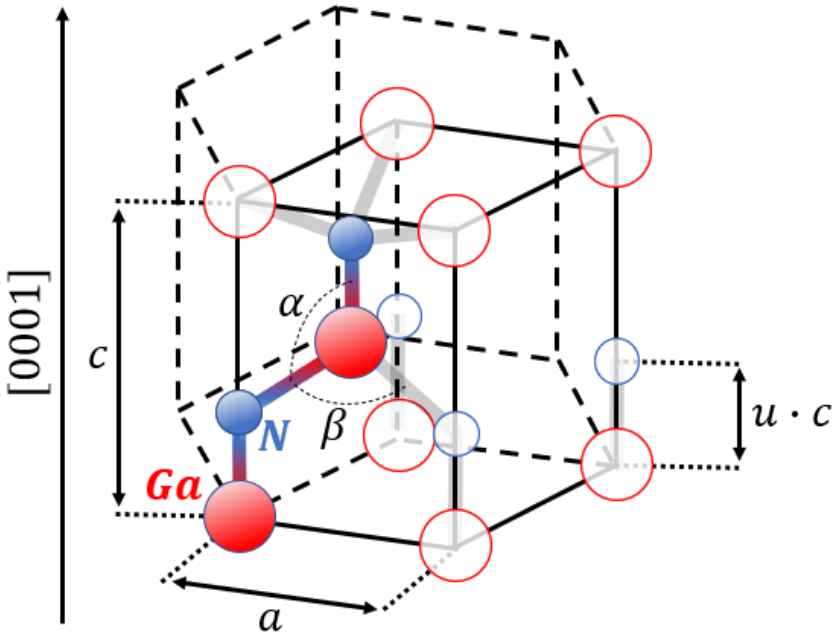

Figure 8 - Unit cell of wurtzite gallium nitride containing two atoms of gallium and two atoms of nitrogen located according to the lattice parameters a and c, and the internal parameter u along the hexagonal direction [0001].

In this figure the lattice parameters a and c are mutually perpendiculars, with the c-axis explicitly defined parallel to the hexagonal direction [0001], and the internal parameter u represents the ratio between the anion-cation bond length and the lattice parameter c.[87,90] For an ideal wurtzite structure, the axial ratio between lattice parameters a and c is $c/a = \sqrt{8/3} \cong 1.633$, and the internal parameter has a value of $u = 3/8 = 0.375$.[65,66,91] Therefore, the bond length between the nearest neighboring atoms of nitrogen and III-nitrides in and off the c-axis can be defined by:[63]

$$d_{in} = u \cdot c$$

$$d_{off} = \sqrt{\frac{a^2}{3} + \left(\frac{1}{2} - u\right)^2 c^2}$$

Here the interatomic distance d_{in} is defined along the c-axis, while the distance d_{off} is defined diagonally with the base of the tetrahedron. Likewise, the angle α established between the atoms of the base and the principal axis, and the angle β defined between the atoms of the base, can be both expressed as functions of the lattice parameters by:[63]

$$\alpha = \frac{\pi}{2} + arccos\left\{\left[1 + 3\left[\left(\frac{c}{a}\left(\frac{1}{2} - u\right)\right)^2\right]\right]^{-\frac{1}{2}}\right\}$$

$$\beta = 2arcsin\left\{\left[\frac{4}{3} + 4\left(\frac{c}{a}\left(\frac{1}{2} - u\right)\right)^2\right]^{-\frac{1}{2}}\right\}$$

The electronegativity of atoms defines how the electron cloud is shifted in a chemical bonding, and this character is overall more intense from the bottom of a group to its top for most of the families in the periodic table, and less intense for families of lower groups.[92] Therefore, in the case of group-III nitrides, using the scale of electronegativity designed by the American chemist Linus Pauling in 1932, the atoms of nitrogen are more electronegative (3.04) than atoms of gallium (1.81), indium (1.78) and aluminum (1.61), for instance, leading to an electronic shift towards nitrogen.[92] Furthermore, Pauling evidenced that the higher the difference in electronegativity between the atoms, the stronger is the stablished bond between them. As the force constant of a vibrating molecule is intrinsically dependent on its bond strength, then the electronic distribution and the atomic spatial configuration strictly affects the modes of vibration in molecular systems represented by any crystallographic group. In order to condense all the symmetry information associated to a certain group, the German mathematician Ferdinand Georg Frobenius made use of principles of group theory applied in the mathematical domain of abstract algebra to develop the theory of irreducible representations.[59,60,73,80] In his theory, Frobenius defines the set of characters of a group as functions that summarize the most important information about symmetry operations applied to that group. This set of characters is condensed in the form of a character table, which facilitates the determination of symmetry properties, as well as the comparison between groups.[49,59,80] Character tables evidence how the action of operations of symmetry transform the irreducible representations of a group, which for convenience and standardization, are in general referenced using the Mulliken symbols for irreducible representations, created by the American chemist Robert Sanderson Mulliken in 1930.[80] Each irreducible representation is associated to one specific vibrational mode in crystals, and the total number of possible modes of vibration is dependent on the number of atoms that constitute the system's unit cell.[12] By using the valence shell electron pair repulsion theory, developed by the British chemist Ronald James Gillespie and the Australian chemist Ronald Sydney Nyholm in 1957, the arrangement of electronic pairs within the system of a wurtzite unit cell can be determined, as well the

tetrahedral shape of the structure.[93] In a three-dimensional Cartesian system of coordinates, a free molecule constituted by N atoms exhibits 3 degrees of translational freedom (along the directional unitary vectors $\hat{x}$, $\hat{y}$ and $\hat{z}$), 3 degrees of rotational freedom (around the axis of the unitary vectors $\hat{x}$, $\hat{y}$ and $\hat{z}$) and a total of $3N-6$ degrees of vibrational freedom.[94] For non-linear molecules there are five dimensions of irreducible representations: A (one-dimensional symmetric irreducible representation considering the principal rotation axis), B (one-dimensional antisymmetric irreducible representation considering the principal rotation axis), E (two-dimensional degenerate irreducible representation, named from the German word *entartet*, meaning "degenerate"), T (three-dimensional irreducible representation), G (four-dimensional irreducible representation) and H (five-dimensional irreducible representation).[80] There are different types of operations of symmetry: E (operation of identity, it corresponds to the operation of doing nothing to the molecule, or also to the rotation of 2π radians around any arbitrary axis), C_n (proper axis, it corresponds to a clockwise rotation of $2\pi/n$ radians around an axis, where n is an integer), C_n^k (proper axis, it corresponds to a clockwise rotation of $2k\pi/n$ radians around an axis, where both n and k are integers), σ (mirror reflection, it corresponds to a reflection in a mirror plane, from the German word *Spiegel*, meaning "mirror"), σ_v (mirror reflection, it corresponds to a vertical reflection), σ_h (mirror reflection, it corresponds to a horizontal reflection), σ_d (mirror reflection, it corresponds to a diagonal reflection), i (inversion center, it corresponds to the deflection between either x and $-x$, y and $-y$ or z and $-z$), and S_n^k (improper rotation, corresponds to a combined operation of a clockwise rotation of $2k\pi/n$ radians around an axis and a reflection in a plane which normal is parallel to the rotation axis).[59,80] As an example, the molecule of water belongs to the group C_{2v}, which displays four elements of symmetry: the identity E, the rotation C_2 of π radians around the z axis, the mirror reflection σ_{xz} in the vertical xz-plane and the mirror reflection σ_{yz} in the vertical yz-plane.[59,80] Character tables can be built by evaluating how the atomic disposition is transformed under operations of symmetry. In the case of water, by applying the operation of C_2 rotation around the z axis it would promote the atoms of hydrogen to trade positions while keeping the atom of oxygen at the same place. It represents an exact antisymmetric inversion of the molecule, which leads to a character identified as -1. The operation of identity E on the other hand results in the same atomic configuration as the original layout, therefore this operation represents a character $+1$ in the character table. Operations that displace the atomic bond to other positions are assigned as character 0, and degenerated elements are treated as

doubled characters.[59,80] Each irreducible representation can be described by basis functions, that represents the geometric transformation of a molecular system under the action of an operation of symmetry. [60,73,80] Wurtzite crystals, as members of the group C_{6v}, exhibit six relevant operations of symmetry: the identity E, the C_6 rotation of $2\pi/6$ radians around the z-axis, the C_3 rotation of $2\pi/3$ radians around the z-axis, the C_2 rotation of $2\pi/2$ radians around the z-axis, the σ_v vertical mirror reflection, and the σ_d diagonal mirror reflection.[56,59,60] Similarly, there are six irreducible representations associated to the group C_{6v}: two characterized by the one-dimensional symmetric element A, two characterized by the one-dimensional antisymmetric element B, and two characterized by the degenerate two-dimensional element E.[56] Figure 9 evidences each operation of symmetry for elements of the group C_{6v}.:[56,80]

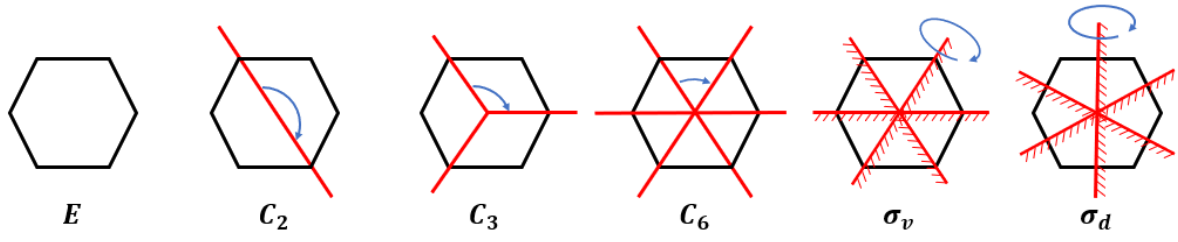

Figure 9 - Operations of symmetry for elements of group C_{6v}.

Additionally, Table 1 represents the character table for crystals that belong to the group C_{6v}, evidencing the quadratic basis functions of each irreducible representation:[95]

Table 1 - Character table for group C_{6v}

C_{6v}	E	$2C_6$	$2C_3$	C_2	$3\sigma_v$	$3\sigma_d$	*Quadratic basis functions*
A_1	1	1	1	1	1	1	$x^2 + y^2, z^2$
A_2	1	1	1	1	−1	−1	
B_1	1	−1	1	−1	−1	1	
B_2	1	−1	1	−1	1	−1	
E_1	2	−1	−1	2	0	0	(xz, yz)
E_2	2	1	−1	−2	0	0	$(x^2 - y^2, xy)$

Each irreducible representation is associated to one particular mode of molecular vibration.[60] When defined by linear basis functions (x, y, z), the irreducible representations are associated to changes in dipole moment during a molecular vibration.[56] Only representations described by quadratic basis functions $(x^2, y^2, z^2, xy, yz, xz)$ exhibit change in polarizability during atomic oscillations, therefore for crystals of group C_{6v} only the irreducible representations A_1, E_1 and E_2 are Raman active, once the variable polarizability is a primary selection rule to be qualified in order to an inelastic Raman scattering event to occur.[56] Additionally, due to the difference of mass between atoms of nitrogen and atoms of the group-III, high and low frequencies of vibration of the same mode can be coexistents in the system.[96] Furthermore, the relative orientation defined between the propagation vectors of incident and scattered light, as well as their modulated electric field, allows the favoritism for certain directions of oscillating atomic dipoles to be excited.[23,97] Figure 10 presents the four Raman active vibrational modes of atomic displacement that occur in group-III nitrides, according to each irreducible representation identified by A_1, E_1 and E_2:[23,26,28,98,99]

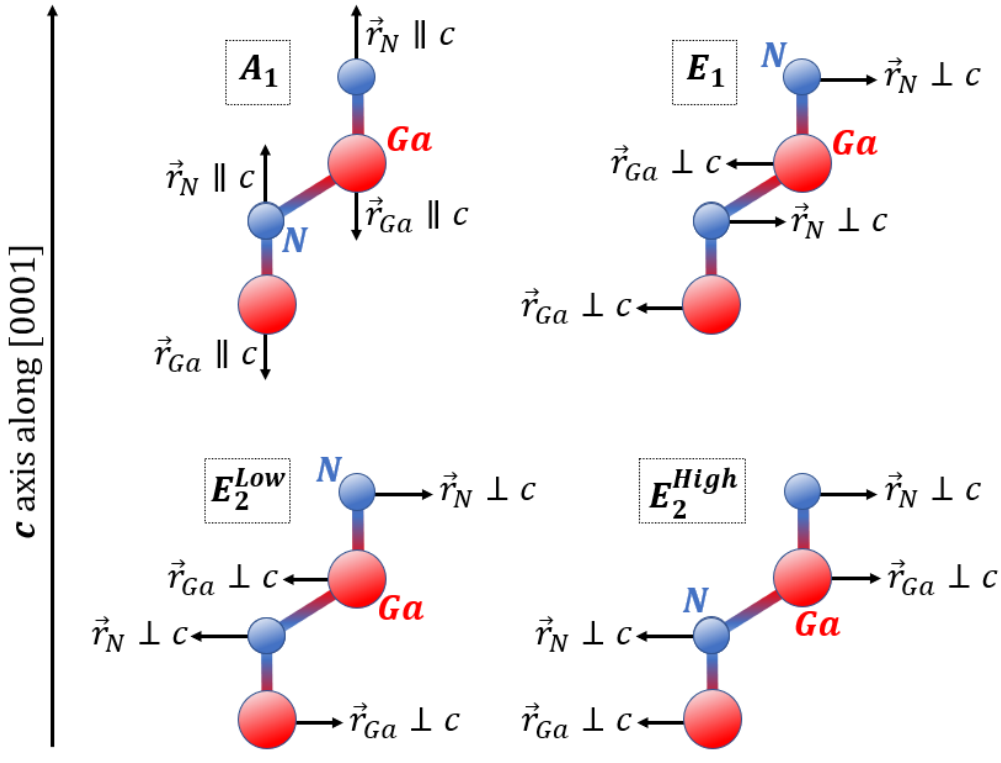

Figure 10 - Raman active vibrational modes of gallium nitride according to the irreducible representations A_1, E_1 and E_2. The atomic displacements $\vec{r}_{Ga}$ for gallium and $\vec{r}_N$ for nitrogen are referred as parallel $(\parallel)$ or perpendicular $(\perp)$ in comparison to the c-axis defined along the [0001] direction.

During events of Raman scattering, the change in the diatomic system's energy due to the interaction with the incident light leads to a modification in the molecular frequency of vibration.[13,20,99] This change in energy, and its correspondent change in the oscillatory frequency, can be evaluated by considering the incident light as a perturbation affecting the original atomic configuration. The magnitude of this effect depends on each irreducible representation associated to its specific type of molecular vibration, as well as features of the crystalline system.[100] In order to quantify this shift in energy, in 1950 the American physicists John Bardeen and William Shockley developed a method of approximation to investigate small shifts in energy due to deformation in the crystal lattice.[101] Their approach, known as linear deformation potential theory, assumes the existence of individual direction-dependent deformation potentials, which when convoluted and applied to each element of strain, are responsible for the overall evidenced shift in energy.[54,91,100–107] Using Cartesian coordinates, in a three-dimensional system the total perturbing potential can be defined by:

$$V = \sum V_{ij}\epsilon_{ij};\ i,j = x,y,z$$

Here each element V_{ij} of the deformation potential is applied to each component of strain ϵ_{ij}. In the absence of rotation, it is useful to use the commutative property of symmetry defined by $(i,j) = (j,i) = \{x,y,z\}$.[100,102] As a function of its elements, the total perturbation can then be expressed by:

$$V = V_{xx}\epsilon_{xx} + V_{xy}\epsilon_{xy} + V_{xz}\epsilon_{xz} + V_{yx}\epsilon_{yx} + V_{yy}\epsilon_{yy} + V_{yz}\epsilon_{yz} + V_{zx}\epsilon_{zx} + V_{zy}\epsilon_{zy} + V_{zz}\epsilon_{zz}$$

$$\therefore$$

$$V = V_{xx}\epsilon_{xx} + V_{yy}\epsilon_{yy} + V_{zz}\epsilon_{zz} + 2V_{xy}\epsilon_{xy} + 2V_{yz}\epsilon_{yz} + 2V_{zx}\epsilon_{zx}$$

The terms of the perturbing potential can be suitably rearranged in order to make explicit the basis functions for each Raman active irreducible representation, given by:[102,103]

$$f_{A_1}: \mathrm{x}^2 + \mathrm{y}^2,\ \mathrm{z}^2$$

$$f_{E_1}: \mathrm{xz}, \mathrm{yz}$$

$$f_{E_2}: \mathrm{x}^2 - \mathrm{y}^2,\ xy$$

Therefore, by only rearranging the terms, the total deformation potential can be expressed as:

$$V = \left\{\frac{1}{2}(V_{xx}+V_{yy})(\epsilon_{xx}+\epsilon_{yy}) + V_{zz}\epsilon_{zz}\right\}_{A_1} + \left\{2\left[(V_{yz}\epsilon_{yz}) + (-V_{zx})(-\epsilon_{zx})\right]\right\}_{E_1}$$
$$+ \left\{\frac{1}{2}\left[(V_{xx}-V_{yy})(\epsilon_{xx}-\epsilon_{yy}) + (-2V_{xy})(-2\epsilon_{xy})\right]\right\}_{E_2} = V_{A_1} + V_{E_1} + V_{E_2}$$

$$\therefore$$

$$V_{A_1} = \frac{1}{2}(V_{xx}+V_{yy})(\epsilon_{xx}+\epsilon_{yy}) + V_{zz}\epsilon_{zz}$$

$$V_{E_1} = 2\left[(V_{yz}\epsilon_{yz}) + (-V_{zx})(-\epsilon_{zx})\right]$$

$$V_{E_2} = \frac{1}{2}\left[(V_{xx}-V_{yy})(\epsilon_{xx}-\epsilon_{yy}) + (-2V_{xy})(-2\epsilon_{xy})\right]$$

In this relation, the quadratic dependence between coordinates is respected and each individual term of irreducible representation is represented by its appropriate function.[108] In group theory, among other properties the orthogonality theorem states that the sum of the product between two elements from matrices of different irreducible representations is equal to zero.[60,73] Therefore, the expected value of energy shift can be expressed by:

$$\langle i|V_j|k\rangle = \delta_{ij}\delta_{jk}{a_j}^f \quad \begin{cases} i,j,k = \{A_1, E_1, E_2\} \\ f = \{\mathrm{x}^2+\mathrm{y}^2,\ \mathrm{z}^2, \mathrm{xz}, \mathrm{yz}, \mathrm{x}^2-\mathrm{y}^2, xy\} \end{cases}$$

Here, δ_{ij} is Kronecker delta and ${a_j}^f$ is the expected value of the deformation potential for each term of basis function on each irreducible representation.[24] Consequently, the total change in energy ΔU_{A_1} for the Raman active non-degenerate irreducible representation A_1 is:[100]

$$\Delta U_{A_1} = \langle A_1|V_{A_1}|A_1\rangle = \left\langle A_1\middle|\frac{1}{2}(V_{xx}+V_{yy})(\epsilon_{xx}+\epsilon_{yy}) + V_{zz}\epsilon_{zz}\middle|A_1\right\rangle$$
$$= \frac{1}{2}\langle A_1|(V_{xx}+V_{yy})|A_1\rangle(\epsilon_{xx}+\epsilon_{yy}) + \langle A_1|V_{zz}|A_1\rangle\epsilon_{zz}$$

The degenerated representations E_1 and E_2 require the decomposition of each basis functions in order to make explicit the existence of degeneracy. For crystals of the group C_{6v}, the character of the identity operator is 2 for both E_1 and E_2 representations, as seen in the character table, which means that these representations are doubly degenerated.[102–105] Therefore, the total change in energy ΔU_{A_1}, ΔU_{E_1} and ΔU_{E_2} for the Raman active irreducible representations A_1, E_1 and E_2 is:

$$\Delta U_{A_1} = a_{A_1}(\epsilon_{xx}+\epsilon_{yy}) + b_{A_1}\epsilon_{zz}$$

$$\Delta U_{E_1} = a_{E_1}(\epsilon_{xx} + \epsilon_{yy}) + b_{E_1}\epsilon_{zz} \pm c_{E_1}\left[(\epsilon_{xx} - \epsilon_{yy})^2 + 4{\epsilon_{xy}}^2\right]^{1/2}$$

$$\Delta U_{E_2} = a_{E_2}(\epsilon_{xx} + \epsilon_{yy}) + b_{E_2}\epsilon_{zz} \pm c_{E_2}\left[(\epsilon_{xx} - \epsilon_{yy})^2 + 4{\epsilon_{xy}}^2\right]^{1/2}$$

These relations stablish the correspondence between the condition of strain the crystal is being submitted to, and the consequent variation in energy associated to the oscillatory system interacting with an incident radiation. When directly compared to energy shift, deformation potentials are measured in units of energy, however, due to its routinely application in Raman studies, the deformation potentials of materials can be often found in units of wavenumber.[102–105] The deformation potentials reign the directional dependency of energy shift, which can be therefore controlled by methods of polarization or, in particular for cases of epitaxial crystalline growth, by promoting a stress-free structural condition suitably aligned with a proper axis.[54,109,110] In this case, the mechanical stress along the growth direction vanishes due to the structure's freedom in expanding or contracting when adjusting itself during the planar settlement of each atomic layer, in response to the matching of bonds between substrate and the material being grown.[109] Then, in order to minimize the strain energy associated to the assembled configuration, only stresses defined along the basal plane will be evidenced.[111] As a consequence, using the simplified parameters in the representation of the components of strain for epitaxial growth of hexagonal crystals, the generalized Hooke's law leads to:[51,53,54,106,112]

$$\begin{bmatrix}\sigma_1\\ \sigma_2\\ \sigma_3\\ \sigma_4\\ \sigma_5\\ \sigma_6\end{bmatrix} = \begin{bmatrix} C_{11} & C_{12} & C_{13} & 0 & 0 & 0\\ C_{12} & C_{11} & C_{13} & 0 & 0 & 0\\ C_{13} & C_{13} & C_{33} & 0 & 0 & 0\\ 0 & 0 & 0 & C_{44} & 0 & 0\\ 0 & 0 & 0 & 0 & C_{44} & 0\\ 0 & 0 & 0 & 0 & 0 & \frac{C_{11}-C_{12}}{2}\end{bmatrix}\begin{bmatrix}e_1\\ e_2\\ e_3\\ e_4\\ e_5\\ e_6\end{bmatrix} = \begin{bmatrix} C_{11}e_1 + C_{12}e_2 + C_{13}e_3\\ C_{12}e_1 + C_{11}e_2 + C_{13}e_3\\ C_{13}e_1 + C_{13}e_2 + C_{33}e_3\\ C_{44}e_4\\ C_{44}e_5\\ \left(\frac{C_{11}-C_{12}}{2}\right)e_6\end{bmatrix} = \begin{bmatrix}\sigma_1\\ \sigma_2\\ 0\\ 0\\ 0\\ 0\end{bmatrix}$$

Here it is evidenced the absence of non-zero components of shear strain e_4, e_5 and e_6 in the system, as well as the consequent relation between the perpendicular components of normal strain:

$$C_{13}e_1 + C_{13}e_2 + C_{33}e_3 = 0$$

Considering also that the stress is two-dimensionally isotropic, the components σ_1 and σ_2 defined along the xy-plane must present the same magnitude, which leads to the identity:[46]

$$\sigma_1 = \sigma_2 \therefore C_{11}e_1 + C_{12}e_2 + C_{33}e_3 = C_{12}e_1 + C_{11}e_2 + C_{33}e_3 \therefore C_{11}e_1 + C_{12}e_2 = C_{12}e_1 + C_{11}e_2$$

The validity of this relation is only assured if the perpendicular components of normal strain in the basal plane e_1 and e_2 also have the same magnitude, which allows the relation obtained from the generalized Hooke's Law to be expressed in function of the bidimensional strain e_1, the perpendicular strain e_3 and the shear strains e_4, e_5 and e_6 as:

$$\begin{bmatrix} (C_{11} + C_{12})e_1 + C_{13}e_3 \\ 2C_{13}e_1 + C_{33}e_3 \\ e_4 \\ e_5 \\ e_6 \end{bmatrix} = \begin{bmatrix} \sigma_1 \\ 0 \\ 0 \\ 0 \\ 0 \end{bmatrix}$$

Therefore, the perpendicular strain can be defined as explicitly dependent on the biaxial strain by:[46,76,113]

$$e_3 = \frac{-2C_{13}}{C_{33}}e_1$$

This relation evidences the Poisson ratio of the system, given by $\nu = -\frac{e_3}{e_1} = \frac{2C_{13}}{C_{33}}$, where $e_1 \perp e_3$ according to each unitary vector, as being completely dependent on the elastic constants of the stiffness tensor for hexagonal crystals.[77] Additionally, this relation can also be obtained in the case of a bidimensional strain in the absence of shear components by expressing the strain energy as:[46]

$$U = \frac{1}{2}\Omega_0 \left[C_{11}{e_1}^2 + C_{11}{e_2}^2 + C_{33}{e_3}^2 + C_{44}{e_4}^2 + C_{44}{e_5}^2 + \frac{1}{2}(C_{11} - C_{12}){e_6}^2 + 2C_{12}e_1e_2 + 2C_{13}e_1e_3 + 2C_{13}e_2e_3 \right] \therefore U = \frac{1}{2}\Omega_0[2(C_{11} + C_{12}){e_1}^2 + 4C_{13}e_1e_3 + C_{33}{e_3}^2]$$

Taking into account that the strain energy does not varies along the z-axis due to the absence of non-zero values of axial stress σ_3, the variation of the total strain energy per unit cell in respect to the axial strain e_3 should be zero, therefore:[84,113,114]

$$\frac{d\,U/\Omega_0}{de_3} = \frac{d}{de_3}\left\{\frac{1}{2}\left[2(C_{11}+C_{12}){e_1}^2 + 4C_{13}e_1e_3 + C_{33}{e_3}^2\right]\right\} = 2C_{13}e_1 + C_{33}e_3 = 0$$

$$\therefore e_3 = \frac{-2C_{13}}{C_{33}}e_1$$

As seen in the generalized Hooke's law relation, the bidimensional stress σ_1 is defined by:

$$\sigma_1 = (C_{11}+C_{12})e_1 + C_{13}e_3$$

Therefore, the explicit perpendicular dependence of the bidimensional stress can be avoided by using the Poisson ratio:

$$\sigma_1 = (C_{11}+C_{12})e_1 + C_{13}e_3 = (C_{11}+C_{12})e_1 + C_{13}\left(\frac{-2C_{13}}{C_{33}}e_1\right),$$
$$\therefore \sigma_1 = \left(C_{11}+C_{12}-\frac{2C_{13}}{C_{33}}\right)e_1$$

By expressing the strain components e_1 and e_3 in their complete notation ϵ_{xx} and ϵ_{zz} respectively, the total change in energy ΔU_{A_1}, ΔU_{E_1} and ΔU_{E_2} due to the system's interaction with an incident light for each Raman active irreducible representations A_1, E_1 and E_2 can then be defined as:[13,54,91,102,103,115]

$$\Delta U_{A_1} = a_{A_1}\left(\epsilon_{xx}+\epsilon_{yy}\right) + b_{A_1}\epsilon_{zz} = 2a_{A_1}\epsilon_{xx} + b_{A_1}\epsilon_{zz}$$

$$\Delta U_{E_1} = a_{E_1}\left(\epsilon_{xx}+\epsilon_{yy}\right) + b_{E_1}\epsilon_{zz} \pm c_{E_1}\left[\left(\epsilon_{xx}-\epsilon_{yy}\right)^2 + 4{\epsilon_{xy}}^2\right]^{1/2} = 2a_{E_1}\epsilon_{xx} + b_{E_1}\epsilon_{zz}$$

$$\Delta U_{E_2} = a_{E_2}\left(\epsilon_{xx}+\epsilon_{yy}\right) + b_{E_2}\epsilon_{zz} \pm c_{E_2}\left[\left(\epsilon_{xx}-\epsilon_{yy}\right)^2 + 4{\epsilon_{xy}}^2\right]^{1/2} = 2a_{E_2}\epsilon_{xx} + b_{E_2}\epsilon_{zz}$$

The variation in the diatomic system's energy ΔU_i for each irreducible representation due to the interaction with the incident light represents a change Δf_i in the frequency of the radiation, which is related to the change in energy by $\Delta\nu_i = \frac{\Delta U_i}{h}$, where $h = 6.626\ x\ 10^{-34}\ m^2Kg/s$ is the Planck's constant.[46] When measured as wavenumbers in reciprocal centimeters by $\Delta\tilde{\nu}_i = \Delta\nu_i/c$, where $c = 299792458\ ms^{-1}$ is the speed of light, this quantity assumes the form of the usual Raman shift $\Delta\omega_i$ evidenced experimentally for each vibrational mode.

Therefore, the Raman shift evidenced for each irreducible representation of members of the group C_{6v} in the absence of both shear strain and epitaxial stress is:[91,102,103]

$$\Delta\omega_{A_1} = 2a_{A_1}\epsilon_{xx} + b_{A_1}\epsilon_{zz}$$

$$\Delta\omega_{E_1} = 2a_{E_1}\epsilon_{xx} + b_{E_1}\epsilon_{zz}$$

$$\Delta\omega_{E_2} = 2a_{E_2}\epsilon_{xx} + b_{E_2}\epsilon_{zz}$$

Here the deformation potentials have units of reciprocal centimeters, as suitable for measuring the Raman shifts. The Poisson ratio $\nu = -\frac{\epsilon_{zz}}{\epsilon_{xx}} = \frac{2C_{13}}{C_{33}}$ can be used to explicit the sole dependence of the bidimensional strain on the observed Raman shift for each irreducible representation:

$$\Delta\omega_{A_1} = 2a_{A_1}\epsilon_{xx} + b_{A_1}\epsilon_{zz} = 2a_{A_1}\epsilon_{xx} + b_{A_1}\left(\frac{-2C_{13}}{C_{33}}\right)\epsilon_{xx} = 2\left(a_{A_1} - \frac{b_{A_1}C_{13}}{C_{33}}\right)\epsilon_{xx}$$

$$\Delta\omega_{E_1} = 2a_{E_1}\epsilon_{xx} + b_{E_1}\epsilon_{zz} = 2a_{E_1}\epsilon_{xx} + b_{E_1}\left(\frac{-2C_{13}}{C_{33}}\right)\epsilon_{xx} = 2\left(a_{E_1} - \frac{b_{E_1}C_{13}}{C_{33}}\right)\epsilon_{xx}$$

$$\Delta\omega_{E_2} = 2a_{E_2}\epsilon_{xx} + b_{E_2}\epsilon_{zz} = 2a_{E_2}\epsilon_{xx} + b_{E_2}\left(\frac{-2C_{13}}{C_{33}}\right)\epsilon_{xx} = 2\left(a_{E_2} - \frac{b_{E_2}C_{13}}{C_{33}}\right)\epsilon_{xx}$$

Consequently, the Raman shift evidenced in materials characterized by the symmetry properties of the group C_{6v}, in the absence of shear strain and epitaxial stress, for each Raman active irreducible representation can be defined by:

$$\Delta\omega_i = 2\left(a_i - \frac{b_i C_{13}}{C_{33}}\right)\epsilon_{xx}, \qquad i = \{A_1, E_1, E_2\}$$

2.4 Raman active longitudinal and transverse optical modes of III-nitrides

When under the influence of an external electric field, an oscillating dipole constituted by two bonded atoms may undergo different vibrational effects depending on the mass and electronegativity of each atom, and consequently also on the type of bonding.[113,116–118] Atoms of the same type are bonded together by covalent interaction, stablishing a nonpolar bond which leads to a zero permanent molecular dipole moment.[13,35] For instance, this bond is responsible for the atomic cohesion in crystals of silicon and of germanium, in which each

atom is bonded to its equivalent, leading to a zero difference in electronegativity.[12] Ionic crystals on the other hand present a much stronger cohesion due to their difference in electronegativity between distinct atoms, such as the crystals of sodium chloride ($3.16 - 0.93 = 2.23$).[12] There are a few distinctive limits to define the character of a bond depending on the scale of electronegativity, and usually, the range between 0.0 and approximately 0.5 is defined as nonpolar covalent bonds, and over approximately 2.0 as ionic bonds. The wide middle range of net electronegativity observed between around 0.5 and 2.0 is dominated by polar covalent bonds. Examples of this class are the semiconductors aluminum nitride ($\chi_N - \chi_{Al} = 3.04 - 1.61 = 1.43$), gallium nitride ($\chi_N - \chi_{Ga} = 3.04 - 1.81 = 1.23$) and indium nitride ($\chi_N - \chi_{In} = 3.04 - 1.78 = 1.26$).[119] The atomic displacement during molecular oscillations in materials constituted by covalent polar bonds generates a macroscopic electric field due to the long scale charge centers vibration. This induced electric field affects the polar modes associated to oscillating dipoles formed by atoms of distinct electronegativity, which in the case of crystals from group C_{6v} are associated to the irreducible representations A_1 and E_1.[116] This phenomenon promotes the split of these modes in transverse and longitudinal components, abbreviated as TO and LO respectively.[116] The atomic oscillation during transverse modes is defined perpendicularly to the direction of propagation of the incident radiation. Therefore, an incident light coming along the z-axis has its modulated electric field oscillating parallel to the xy-plane, and if the c-axis of the hexagonal crystal is defined along the z-axis, then the bonds situated within the xy-plane will be transversally affected, originating the modes described by the irreducible representations $A_1(TO)$ and $E_1(TO)$.[80,116] On the other hand, the nonuniform distribution of charges along the material's c -axis leads to an induced electric field which affects the bonds defined perpendicularly to the xy-plane, originating the modes described by the irreducible representations $A_1(LO)$ and $E_1(LO)$.[59,116,120] In the lack of a perfect perpendicular or parallel alignment between the directional orientation defined by vectors of dipole moment and electric field, possible combinations of transversal and longitudinal modes may occur, leading to partial contributions to each mode in the oscillatory system. This phenomenon of transverse-longitudinal splitting is not evidenced in the nonpolar mode associated to the irreducible representation E_2, once this mode represents the vibration between two similar atoms.[105] In the case of group-III nitrides, the oscillation between two atoms of nitrogen is associated to the irreducible representation E_2 by the nonpolar mode E_2^{High}, while the oscillation between two atoms from the group-III is

associated to the irreducible representation E_2 by the nonpolar mode E_2^{Low}.[102,103,105] This distinction is due to the difference of mass in the systems defined by symmetric dipoles, once a lower atomic mass leads to a higher frequency of dipole oscillation.[26] Therefore, the frequency of E_2^{High} modes are higher than that exhibited by E_2^{Low} modes.[13,121] In 1941, while studying polar vibrations, the physicists R. H. Lyddane, R. G. Sachs and E. Teller evidenced the existence of a relation connecting the ratio between the transverse and longitudinal mode frequencies and the dielectric constant of the crystal. This expression, known as Lyddane-Sachs-Teller relation can be defined by:[116,120]

$$\left(\frac{\omega_{LO}}{\omega_{TO}}\right)^2 = \frac{\varepsilon_{st}}{\varepsilon_{\infty}}$$

Here, ω_{TO} and ω_{LO} represents the frequency evidenced in Raman of transverse and longitudinal modes respectively, and ε_{st} and ε_{∞} are the static and high frequency dielectric constant of the crystal.[122] Table 2 presents the observed frequencies of Raman active transverse and longitudinal modes existent in group-III nitrides:[63,76,86,123]

Table 2 - Raman active frequencies of aluminum nitride, gallium nitride and indium nitride for each mode represented by polar and nonpolar irreducible representations.

$\boldsymbol{\omega}$	$\boldsymbol{AlN}$[86]	$\boldsymbol{GaN}$ 76	$\boldsymbol{InN}$ 123
$\mathbf{E_2^{Low}}$	252	144	83
$\mathbf{A_1(TO)}$	614	532	443
$\mathbf{E_2^{High}}$	656.7	567.4	483
$\mathbf{E_1(TO)}$	667	561	467
$\mathbf{A_1(LO)}$	893	735	586
$\mathbf{E_1(LO)}$	916	743	595

2.4.1 Mode E_2^{High} as a mechanical sensor in III-nitrides

Due to its high intensity and exceptional sensitivity to local stress, the nonpolar mode E_2^{High} represents a powerful tool in the investigation of strain in wurtzite crystals.[26,113] In

group-III nitrides, the mode E_2^{High} has its origin associated to the vibration between atoms of nitrogen, which are lighter than atoms of aluminum, gallium and indium, and therefore have their oscillation more easily affected by the structural properties of the lattice environment.[65,76,91,123] On the other hand, the nonpolar mode E_2^{Low} represents the oscillation of couples of atoms of aluminum ($m_{Al} \cong 26.98\,u$), gallium ($m_{Ga} \cong 69.72\,u$) and indium ($m_{In} \cong 114.82\,u$), which are heavier than the atoms of nitrogen ($m_N \cong 14.01\,u$), and therefore less easily affected by mechanical features of the lattice.[65] In special, for wurtzite crystals in the absence of nonzero values of epitaxial stress σ_{zz}, the local bidimensional strain ϵ_{xx} can be directly obtained by evaluating the frequency of the mode E_2^{High}, which is defined by:

$$\Delta\omega_{E_2^{High}} = 2\left(a_{E_2^{High}} - \frac{b_{E_2^{High}} C_{13}}{C_{33}}\right)\epsilon_{xx}$$

Here, $a_{E_2^{High}}$ and $b_{E_2^{High}}$ are the deformation potentials for the nonpolar mode associated to the irreducible representation E_2, while C_{13} and C_{33} are the components of the stiffness tensor representing the relevant elastic constants.[51,72,76,113,123] Also, the shift $\Delta\omega_{E_2^{High}}$ is taken as the difference between the frequency of an unstrained material and the frequency evidenced by Raman.

2.4.2 Modes E_1 and A_1 as electric sensors in III-nitrides

Due to their polar character, the modes E_1 and A_1 of wurtzite crystals exhibit the ability of stablishing a coupled condition with lattice plasmons, which allows the investigation of electric features of crystals, such as its carrier concentration and carrier mobility.[124] For instance, in the case of gallium nitride, its carrier concentration has been shown to express a dependent behavior to its longitudinal modes for concentration values under $10^{19} cm^{-3}$, according to the relation:[124–126]

$$\mathrm{N} = N_0\left(\omega_{LO}^{coupled} - \omega_{LO}^{uncoupled}\right)^r$$

Here, N_0 and r are parameters associated to each polar mode characterized by its specific irreducible representation E_1 ($N_0 = 5.3x10^{16},\ r = 0.876$) and A_1 ($N_0 = 1.1x10^{17},\ r = 0.764$).[125,127] Additionally, the carrier concentration can also be obtained by evaluating the plasmon frequency by:[127–129]

$$\omega_p = \frac{1}{2\pi c}\left(\frac{Ne^2}{m^* m_e \varepsilon_\infty \varepsilon_0}\right)^{1/2}$$

In this relation, $c = 299792458\ ms^{-1}$ is the speed of light in vacuum, $e = 1.602x10^{-19}C$ is the elemental electronic charge, $m^* = 0.2m_0$ is the electronic effective mass in wurtzite gallium nitride, $m_e = 9.109x10^{-31}Kg$ is the electron rest mass, $\varepsilon_\infty = 5.35$ is the high frequency dielectric constant of wurtzite gallium nitride and $\varepsilon_0 = 8.85x10Fm^{-1}$ is the absolute dielectric permittivity in vacuum.[130] The carrier mobility has its consequent dependence to the plasmon damping constant γ given by:[125,130]

$$\mu = \frac{e}{m^* \gamma}$$

Here, the dependence between phonon and plasmon parameters is given by the dielectric constant as function of the frequency shift evidenced using Raman as:[125,131]

$$\varepsilon(\omega) = \varepsilon_\infty\left(1 + \frac{\omega_{LO}^2 - \omega_{TO}^2}{\omega_{TO}^2 - \omega^2 - i\omega\Gamma} - \frac{\omega_p^2}{\omega^2 - i\omega\gamma}\right)$$

The value associated to the phonon damping constant Γ and plasmon damping constant γ, as well as the plasmon frequency ω_p, are all obtained by a method known as line shape model, which is used to investigate the acquired Raman spectrum under the condition of resonance in a coupled system constituted by electronic charges and lattice phonons.[132] The Raman intensity is considered to be dependent on the imaginary part of the inverse of dielectric function of the media:[125]

$$I(\omega) = S \cdot A(\omega) \cdot \Im\left(\varepsilon^{-1}(\omega)\right)$$

Here, S is a proportionality factor and $A(\omega)$ is a function that depends on the phonon and plasmon parameters, as well as on the Faust-Henry coefficient C, which defines the changes on the material's electric susceptibility due to lattice displacements and the presence of electric field.[133] The line shape model has been used in the last decades mainly for materials constituted by gallium nitride[125] and indium nitride[124].

2.5 Raman spectroscopy and its advantages

Since its discovery, the Raman effect has been widely explored in a great variety of fields.[7,34,35] The first investigations were devoted to the investigation of the nature of the effect, as well as its possibilities and limitations.[35] As observed, the Raman effect can be evidenced in several materials, allowing the identification of compounds due to its characteristic vibrational signatures.[13–15,20,23] In addition, the structural features of materials, such as its mechanical characteristics and electrical response can also be examined by exploring the appropriate Raman modes. Experimentally, the Raman spectroscopy does not require sophisticated methods of sample preparation, once the sample can be analyzed even in situ, at room conditions of temperature and pressure. The exploratory interaction is also nondestructive and can also be made through enclosed containers in the case of sensitive samples. Despite its low intensity when compared to Rayleigh scattering, the Raman signal can be amplified by stablishing conditions of resonance.[15] Even small amounts of materials can be investigated by Raman, and additionally, by acquiring the signal at the microscale, the technique allows to perform the surface mapping of structures.[134] Polar and nonpolar molecules can be satisfactorily studied using the Raman technique, with a precision of energy shift due to molecular vibration in the order of decimals of millielectronvolt.[23] Along the decades, more and more companies have become interested in using the Raman effect in the characterization of materials, such as Horiba, Thermo Fisher Scientific and Renishaw, among many others. The relative simplicity of the technique is also a great advantage when employing the Raman effect in automated systems. For instance, equipped with an ultraviolet spectrometer, the Perseverance rover is making history in 2021 by collecting Raman data in the surface of the planet Mars.[135] The rover uses a system named SHERLOC (Scanning Habitable Environments with Raman & Luminescence for Organics and Chemicals), which is one of the seven scientific instruments sent aboard the Mars 2020 mission. SHERLOC is focused on the study of minerals, organic molecules and search for biosignatures, and using the Raman effect, it might be the first system ever to detect chemical traces of life on Mars.[135–137]

Chapter 3: GaN/AlN superlattices

This chapter presents a brief review about superlattices, focusing on the fabrication and characteristics of III-nitride nanostructures. Interesting properties of aluminum and gallium

nitrides are discussed and compared with other materials. The phenomenon of lattice coherence is then evaluated in the case of AlN/GaN superlattices, also considering mechanisms of stress relief in nanostructures.

3.1 Superlattices

The earliest structures remotely resemblant to modern superlattices have their origins in the attempt to understand the resulting effects of mixing solid materials, mostly according to its electrical properties. In 1919, while investigating the galvanic characteristics of mixed crystals and metallic alloys, the Russian chemist Gustav H. J. A. Tammann verified that a significant change in electric resistance was evidenced after submitting a multilayer material to a long period of annealing.[138] It was proposed that the high temperature would lead the disordered atoms to stablish an orderly distribution within the materials, which was verified by the German scientists C. H. Johansson and J. O. Linde in 1925 when analyzing the x-ray diffraction pattern of an alloyed system constituted by a mixture of gold and cooper.[139] In 1935, a theoretical approach based on the thermodynamics of superlattices was developed by the German physicist H. A. Bethe by considering the atomic arrangement as fundamentally dependent on the temperature.[140] In 1937, the British physicists E. A. Owen and I. G. Edmunds evaluated the temperature dependence of a gold-zinc alloy system, achieving success in discriminating the x-ray diffraction pattern lines due exclusively to the multilayer structure.[141] Owen and Edmunds observed that those lines which origin relied on the separated materials could be seen invariably in the mixed system, although the lines resulting from the multilayer were dependent on its characteristics, such as the number and length of periodical layers. It was proposed by the American physicist J. S. Koehler in 1970 that the epitaxial growth of alternating thin layers of two different crystals, with distinct elastic constants, would lead to a material which tensile and compressive features differ from those of its separate precursors.[142] This theoretical multilayer structure would require close values of basal lattice constants between layers in order to minimize interfacial strain due to structural mismatch at atomic scale, as well as similar parameters of thermal expansion when intending structural stability. Also, the chemical bonding between atoms of different crystals should be as approximately large as the bonding between atoms in each separated crystal. The width of the layers should be small enough to accommodate no more than one hundred atomic layers in order to reduce the eventual generation of crystallographic defects, such as edge and screw dislocations. Under

the assumption of these conditions a successful superlattice growth would presumably result in a multilayer material with a stable interatomic cohesion and increased mechanical hardness.[142]

The initial idea of using superlattices as semiconductor quantum devices has its origin in the works of the Japanese physicists Reona Esaki and Raphael Tsu.[143] In 1970, Esaki and Tsu proposed a model of a nanostructured material that theoretically would allow the investigation of quantum effects on a new physical scale. In their work, Esaki and Tsu considered a periodic variation of impurity density or alloy concentration along the epitaxial growth process, leading to a one-dimensional periodic nanostructure.[143] The epitaxial growth would allow to control both the period of the superlattice, defined as the thickness of the smallest portion of the structure to be repeated along the material; as well as the number of repetitive cycles, commonly named as amplitude. Quantum aspects, such as the resulting material's energy band structure considering the periodic potential faced by carriers, as well as their transport characteristics, would all be controllable considering their direct dependence to the structural features of the superlattice.[143] In the following decades, innumerable semiconductor devices were developed basing their functionality on the properties of superlattices, being destinated to fields such as light emitting diodes[144,145], thermoelectronics[146], sensors[147], and many others.

3.2 Fabrication of III-nitrides superlattices

The earliest achievements in synthesizing nitrides using elements of the Boron family of the periodic table (B, Al, Ga, In, Tl) in the form $M^{[iii]}N^{[V]}$ date from the first decades of the 19th century. Commonly, nitride compounds were produced as a consequent process of heating either the pure form or an oxide of a metal in the presence of either nitrogen flux, ammonia or cyanide, aiming to provide an environment rich in ionic nitrogen as well as to favor the chemical reactivity. In 1842, the British chemist William H. Balmain synthesized for the first time boron nitride in its isolated form by reacting molten boric acid with potassium cyanide.[148] In 1876, the Irish chemist John W. Mallet accidentally produced aluminum nitride by heating alumina and carbon under flow of nitrogen.[149] Both indium nitride and thallium nitride were synthesized in 1910 by the German chemists Fischer and Schröter using a reaction with nitrogen gas in a cathodic discharge and cooling the final product in a liquid mixture of argon and nitrogen.[150] Finally, in 1932 the American chemist Warren C. Johnson successfully

produced isolated gallium nitride employing metallic gallium on ammonia gas at high temperatures.[69]

The final product acquired in these initial achievements of producing group-III nitrides were limited to small amounts of impure powder, which instability frequently led to undesirable post-final products by indirect reactions. Since then, the last century has faced the development of sophisticated techniques of crystalline growth based on the controlled deposition of chemical agents under more suitable conditions of temperature and pressure.[84,114] Differently from the earliest processes of crystal growth based on rustic forms of chemical vapor deposition (CVD), which rely on the chemical reaction between precursors often guided by catalysts, the technique named molecular beam epitaxy (MBE) involves the physical process of thin-film deposition, with nanometric precision at atomic scale layer by layer.[114] This deposition is conducted at conditions of ultrahigh vacuum at high temperatures, in which beams of atoms or molecules reach the clean surface of a single-crystalline substrate allowing the epitaxial growth of a nanometric structure with a defined crystalline orientation. Variations of the MBE technique have been developed since the 80's, such as high frequency MBE ($RF-MBE$),[151,152] ammonia-MBE,[153–156] plasma assisted MBE ($PAMBE$)[128,153,157–160] among others, which differ commonly in respect with the type of source employed to build the nanometric material. In special for nitrides, precursor sources constituted by ammonia or nitrogen plasma have displayed successful results, paving the way for suitable conditions of group-III nitrides growth.[114] The epitaxial growth of the nanostructure can be facilitated by avoiding conditions of intense thermal and structural mismatch due to the different coefficients of thermal expansion characteristics of the substrate and the nanostructure, as well as their different interatomic distances at equilibrium.[114] To do so, in order to provide a starting atomic surface atop of the substrate acting as a chemically friendly structure to the incoming atoms, it is usual to grow an initial layer, known as buffer layer, right above the substrate serving as a receptive surface for the atomic deposition and its successful adhesion, as well as for absorbing any undesirable stress due to structural arrangement. In Figure 11 the unscaled diagram represents the usual structure of a superlattice constituted by alternating layers of group-III nitrides grown by MBE:

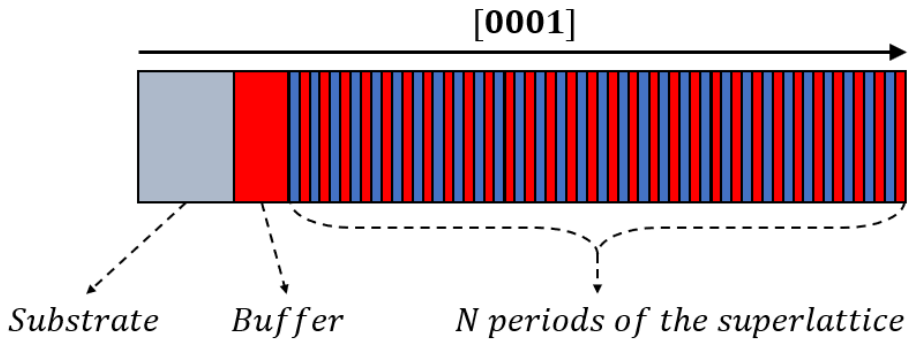

Figure 11 – Unscaled structure of a superlattice grown on top of a buffer layer over a substrate.

Besides the initial buffer layer, a final layer known as cap layer can also be grown on top of the superlattice as the last layer of the nanostructure, which has been shown to minimize surface current dissipation, as well as to reduce the propagation of dislocation defects promoted by residual strain release.[161] When selecting the substrate to be used for the growth of a superlattice, a wise decision must be based on fundamental aspects considering every step of the growth process, such as ensuring a structural affinity in the crystalline environment by reducing the interatomic distance discrepancy between substrate and nanostructure, commonly referred as lattice mismatch, in order to avoid a permanent condition of intense unintentional residual internal stress along the superlattice.[162] Also, it is advisable to use a substrate that allows thermal reliability at the nanostructure's growth temperature of synthesis. This can be done by evaluating the coefficients of thermal expansion of both substrate and the material to be grown, which must be close to each other. Electrical insulation must be also considered when aiming the production of nanostructured devices, which operation might be put in jeopardy during eventual electrical interactions with its surrounding environment. Additionally, the feasibility of a successful growth at nanoscale also depends on the logistics of synthesis, such as cost for production, availability of materials and overall complexity of the growth process.

In special, the research on semiconductor nitrides focused on gallium, aluminum and indium nitrides (GaN, AlN, InN) have attracted increased attention due to their remarkable functionality as sources of light emission, such as their tunable bandgap from visible to ultraviolet,[163] suitable operation in a wide range of temperatures,[164] high electron mobility,[165] and stable performance under high input power.[166] In particular, in the last few years AlN/GaN heterostructures have been widely employed in the industry of optoelectronic devices. Many investigations have been exploring the optical operation of these materials, such as in light

emitting diodes ($LEDs$) for the ultraviolet spectral range, currently covering the emission range in the UVA,[167] UVB,[168] UVC,[169] and most recently in the deep ultraviolet (DUV), reaching wavelength values as low as $219\ nm$[170] and $210\ nm$[171] These materials represent a much more sustainable and safer alternative to replace the environmentally harmful conventional mercury lamps.[163] The electroluminescent emission blueshift displayed by AlN/GaN superlattices has been reported to be highly dependent on the heterostructure thickness ratio and can be achieved by tunning the width of GaN along the nanostructure[172] Recent achievements using ternary structures, such as $GaN/AlGaN$ multi quantum wells, have been made in the field of quantum information by emitting uncontaminated ultraviolet single-photons at room temperature, exhibiting high purity with values of second-order correlation histogram as low as 0.02.[173] Also at room temperature, it has been reported fast switching speeds using AlN/GaN resonant tunneling diodes, whose heterostructures have been displaying a stable negative differential resistance behavior with peak-to-valley current ratios reaching values over 2.[174] The use of $InAlN/GaN$ and $AlGaN/GaN$-based ultrawide-bandgap high-electron-mobility transistors ($HEMTs$) have also been studied.[175] These materials have exhibited outstanding thermal stability with reliable operation and high electron density in the frequency range of $MHz - GHz$, as well as short detrapping time constants lower than $1\ ms$ and high electron mobility over $2000\ cm^2/Vs$, which are all suitable characteristics to be used in high-power switching applications.[61] The chemical engineering of $In_xGa_{1-x}N$ alloys have allowed the production of versatile light emitters which operation ranges from approximately $360\ nm$ until $2000\ nm$ by only modifying the relative concentration between indium and gallium in the nanostructure, such as devices constituted by an active layer of $In_{0.20}Ga_{0.80}N$ for blue light, $In_{0.43}Ga_{0.57}N$ for green light and $In_{0.70}Ga_{0.30}N$ for yellow light emission.[176,177] Polarization charges have been evidenced in the form of two-dimensional electron gas ($2DEG$) channels at III-nitride heterostructures interfaces.[178] These spontaneous and piezoelectric charges are introduced by the material's geometry and interlayer stress and are shown to be highly influential on the overall device performance. As a visualization of the broad luminescent emission of III-nitrides, Figure 12 presents the comparison between the lattice parameter and the bandgap of each wurtzite crystal, illustrating the coverage of the whole visible electromagnetic spectrum by also considering the ternary compounds $AlGaN$, $InGaN$ and $InAlN$.[114]

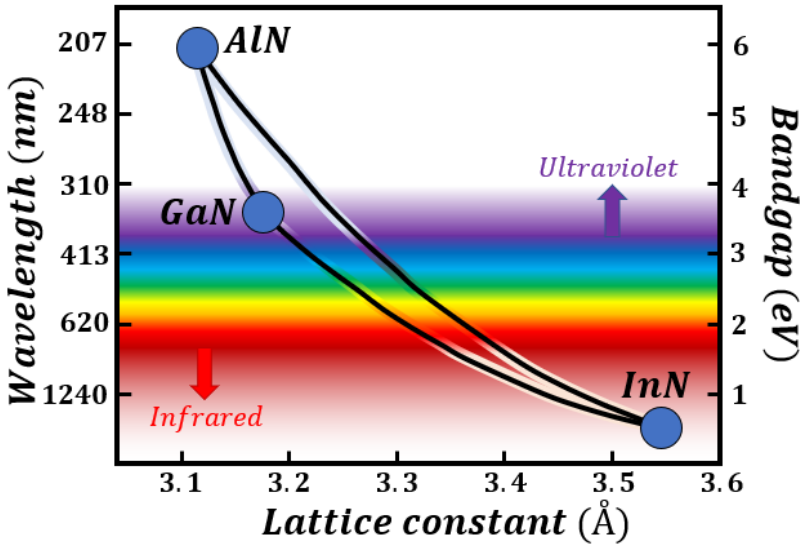

Figure 12 - Structural and optical properties of GaN, AlN, InN and their ternary compounds.

One of the main difficulties associated to the fabrication of operational III-nitride devices, besides the requirement of an inert ultrahigh vacuum environment and structural compatibility at nanoscale, is related to finding the suitable thermal conditions in order to effectively accomplish a well succeeded chemical reaction. The ultimate goal during the MBE growth of III-nitrides is to accomplish the formation reaction $M_{(g)} + N_{(g)} \xrightarrow{\Delta} MN_{(s)}$, where $M_{(g)}$ represents the group-III element and $N_{(g)}$ is nitrogen, both of them in the gas state, are reacting at a specific temperature to yield the III-nitride as final product $MN_{(s)}$ in the solid state.[179] This formation reaction exemplifies the general production of a III-nitride over the substrate, however additional and equally important intermediary steps must occur in order to make it possible to the crystalline growth to happen. For instance, in the production of gallium nitride using ammonia as source of nitrogen, the reduction of ammonia must occur, given by $NH_{3(g)} \rightarrow \alpha NH_{3(g)} + \beta N_{2(g)} + \gamma H_{2(g)}$, where the stoichiometric coefficient β measures the reaction efficiency in the formation of nitrogen gas $N_{2(g)}$, while hydrogen gas $H_{2(g)}$ is produced as a side product.[114] The crystalline growth rate is mostly determined by the temperature at the group-III element effusion cell, which in this case delivers the gaseous gallium to the reactive medium. By using c-plane sapphire as substrate, which interatomic distance between neighboring atoms in one of its families of planes of hexagonal symmetry equals to approximately 2.747 Å, a compressive strain due to a lattice mismatch of about 16 % will be felt in the gallium nitride layer, which basal lattice parameter in its hexagonal form equals to 3.189 Å.[114] The basal thermal expansion coefficients of c-plane sapphire (

$7.5x10^{-6}\,K^{-1}$) and gallium nitride ($5.6x10^{-6}\,K^{-1}$) exhibit small deviation at high temperatures, which decreases the lattice mismatch between substrate and nanostructure to about $15.9\ \%$.[114] The influence of this strained condition on the superlattice can be reduced by growing an initial buffer layer in order to absorb the effects of the residual stress and thermal expansion, which also guarantees a suitable reactive surface during the nanostructure synthesis.

Devices that are fabricated using the superlattice architecture have interesting properties arising from the superlattice structural periodicity. As an example, the alternating layers of gallium nitride and aluminum nitride in AlN/GaN superlattices define a periodic potential faced by carriers in the device, which electrical and optical properties are intrinsically dependent on the thickness of each distinct layer. When conditions of quantum confinement are met, such as the layers' thicknesses being at the same order as the material's Bohr radius, an intermittent disposition of wells and barriers are formed along the nanostructure. In particular, due to the large bandgap of aluminum nitride when compared to gallium nitride, the layers of AlN are faced as quantum barriers by carriers meanwhile the layers of GaN are faced as quantum wells. By modifying the conditions of synthesis, such as atomic composition and layer width, the energy levels of the quantum wells can be altered using methods of bandgap engineering.[180] Additionally, due to the lack of inversion symmetry along the c-axis of crystals from group C_{6v}, the uneven atomic disposition along the $[0001]$ direction leads to a natural state of polarity that also affects the superlattice's features.[57] In special, when compared to atoms of aluminum or gallium, the higher electronegativity displayed by nitrogen atoms tends to attract the electron cloud in its direction, creating a spontaneous separation between positive and negative charge centers along the superlattice. This property, known as spontaneous polarization P^{SP}, is intrinsically dependent on the material's polarity properties and it exists even in the absence of external events. Figure 13 illustrates the direction of spontaneous polarization in the case of wurtzite gallium nitride, by comparing a Ga-faced gallium nitride structure (spontaneous polarization antisymmetrically aligned with the $[0001]$ direction), and a N-faced gallium nitride structure (spontaneous polarization symmetrically aligned with the $[0001]$ direction).[181]

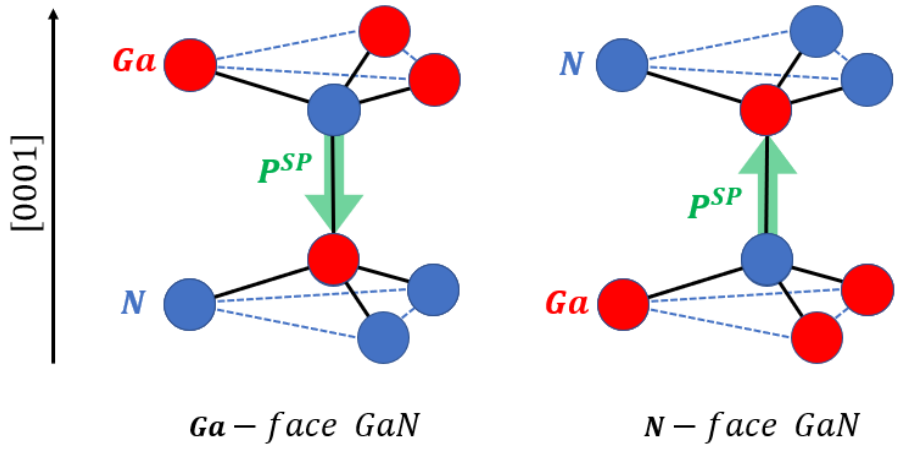

Figure 13 - Comparison between two polarities of gallium nitride: Ga-face GaN and N-face GaN.

In the presence of strain, an additional contribution to the polarization arises from the electric field generated by the displacement of charges from the equilibrium positions characteristic of their relaxed state. This mechanically activated polarization, known as piezoelectric polarization P^{PZ}, is dependent on the type and intensity of strain faced by the lattice environment. In the case of tensile strain ($\epsilon_i > 0$), which represents the situation when the atomic bonds are constantly being stretched, both spontaneous and piezoelectric polarizations are aligned parallelly along the same direction. On the other hand, in the case of compressive strain ($\epsilon_i < 0$) when the atomic bonds are being squeezed, both spontaneous and piezoelectric polarizations are aligned antiparallelly to each other. As a function of the stress, the piezoelectric polarization can be expressed in terms of piezoelectric moduli d_{il} by $P_i^{PZ} = \sum_k d_{ik}\,\sigma_k$, with $i,k = \{xx, yy, zz, yz, zx, xy\}$. Furthermore, by using the generalized Hooke's law between stress and strain, the dependence on strain can be made explicit by using the piezoelectric constants e_{ij}, which are obtained directly from the elastic constants of the stiffness tensor $\overleftrightarrow{C}$ for each material by $e_{ij} = \sum_k d_{ik} C_{kj}$. Overall, the total polarization that each layer of an AlN/GaN superlattice experiences is the sum between its spontaneous and piezoelectric components: $P_i^{Total} = P_i^{SP} + P_i^{PZ}$, with $i = \{AlN, GaN\}$. In heterostructures, the carriers may face an abrupt change in polarization at the interface between layers of distinct materials. This phenomenon generates a two-dimensional charge density of polarization at the superlattice's interfaces, which consequently is responsible for the promotion of local built-in electric field stablished alternately along the direction of epitaxial growth.[182] The magnitude

of the electric field experienced within each layer ($\vec{F}_{AlN}$ and $\vec{F}_{GaN}$) is dependent on the thickness of the layers (d_{AlN} and d_{GaN}) and on their total polarization ($\vec{P}_{AlN}^{Total}$ and $\vec{P}_{GaN}^{Total}$), and it can be expressed by:

$$\vec{F}_{GaN} = \frac{d_{AlN}\left(\vec{P}_{AlN}^{Total} - \vec{P}_{GaN}^{Total}\right)}{\varepsilon_0(\varepsilon_{AlN}d_{GaN} + \varepsilon_{GaN}d_{AlN})} = -\frac{\vec{F}_{AlN}d_{AlN}}{d_{GaN}}$$

In this relation, ε_{AlN} and ε_{GaN} represent the static dielectric constant for the wurtzite form of aluminum nitride and gallium nitride. Their values can be both obtained from the Lyddane-Sachs-Teller relation between dielectric constants and the frequency splitting of polar modes associated to the irreducible representations A_1 and E_1 of each material.[183,184]

3.3 Properties of aluminum nitride

One of the main difficulties faced during the development of electrical devices is associated with its ability in avoiding current leaks, especially when the system layout involves operations at high voltages.[185] Events of current leakage might compromise not only the entire electronic device, but it may also lead to aggravated occurrences of electrical fire affecting and corrupting the whole system. In order to prevent such unwanted incidents to occur, it is usual to employ materials that exhibit high electrical resistance and that therefore will act as an insulation shield during the device's normal operation. In special, aluminum nitride is a suitable material to be used in systems that require electrical insulation due its low electrical conductivity (in the order of $10^{-12}\Omega^{-1}cm^{-1}$). Additionally, the high thermal conductivity ($321\ W/mK$) of aluminum nitride makes it a wonderful choice to perform the heat exchange in thermal management systems, such as in the battery systems of electric and hybrid vehicles.[185] The extremely large bandgap of aluminum nitride ($E_{gap}^{AlN} \cong 6.0\ eV$) also allows its use in the production of light sources emitting in the deep ultraviolet spectral range. In particular, emissions in wavelengths as low as $210\ nm$ have been achieved by using aluminum nitride nanowires.[171]

3.4 Properties of gallium nitride

Since the technological revolution promoted by the creation of white LED (light emitting diode) in the last decades, thanks to the successful development of blue luminescent emission made possible by the enduring efforts of the Japanese physicists Isamu Akasaki, Hiroshi Amano and Shuji Nakamura using gallium nitride, this semiconductor has attracted an increasing amount of interest, by both academic and commercial fields.[186] In special, Akasaki, Amano and Nakamura were awarded with the Nobel Prize in Physics in 2014 for their work on blue light emitting diodes, which have been used worldwide as a more sustainable and energy-saving light source. Many companies, such as Anker, GaN Systems, NXP Semiconductors, Fujitsu, among others, have been exploring the remarkable benefits of gallium nitride. Besides its exceptional efficiency as light source, gallium nitride has been the active compound in a versatile field of devices, such as battery charges, radio frequency transmitters, power amplifiers for 5G networks and satellite communications and many others high switching frequency power electronics.[187,188] Gallium nitride has a breakdown field of $3.3\ MV/cm$, which means that this material is capable of supporting voltages of up to approximately ten times higher than the maximum value supported by silicon, which exhibits a breakdown field of about $0.3\ MV/cm$.[187] For silicon, any internal field over this threshold limit will promote the material's ionization and extraordinary increase in the flow of electric current, which may lead to the failing of operation of electronic devices. That is why gallium nitride presents superior performance than silicon in systems that require high voltages. Additionally, due to its high electron mobility ($\mu_{GaN} \cong 2000\ cm^2/Vs$), gallium nitride is more suitable to be used in devices designed for high frequency operations in radio frequency switchers than silicon, which electron mobility is inferior ($\mu_{Si} \cong 1500\ cm^2/Vs$), representing an electronic movement of about 25% slower in silicon than in gallium nitride. The large bandgap of gallium nitride ($E_{gap}^{GaN} \cong 3.4\ eV$) also allows its operation in a wider range of temperatures than silicon ($E_{gap}^{Si} \cong 1.1\ eV$) by reducing effects of thermal generation of carriers at high temperature, which is a feature to be considered when designing transistors in sustainable and energy-saving industries.[187]

3.5 Lattice coherence in *AlN/GaN* superlattices

In 1954, the Ukrainian physicist Serguei Mikhailovitch Rytov developed a theoretical method to study the propagation of electromagnetic waves in multilayered systems.[189] His theory, known as Dielectric Continuum Model (DCM), has been since then successfully applied in the investigation of electric and mechanical properties of heterostructures built in nanoscale, such as multiple quantum wells and superlattices.[183] The model considers the electrostatic media constituted by the multiple layers as a system of intermittently alternated dielectric permittivity constants. It evaluates the resulting modulation of the electric field assuming the validity of boundary conditions, such as the continuity of electric field between layers, as well as the electric displacement due to polarization at the interface. For crystals of the group C_{6v}, the irreducible representations A_1 and E_1 represent polar modes of dipole oscillation with defined directions of polarization.[80] A wurtzite crystal grown along the z-axis in the direction $[0001]$ has its vibrational modes $A_1(TO)$ and $A_1(LO)$ polarized along the z-axis, while its vibrational modes $E_1(TO)$ and $E_1(LO)$ are polarized within the xy-plane. Therefore, in a comparison to the Lyddane-Sachs-Teller relation between dielectric constants and the frequency splitting of polar modes, the components of the dielectric permittivity at each layer constituting the media can be defined by:[118,183]

$$\varepsilon_{xx}(\omega) = \varepsilon_{\infty} \frac{\omega^2_{E_1(LO)} - \omega^2}{\omega^2_{E_1(TO)} - \omega^2}$$

$$\varepsilon_{zz}(\omega) = \varepsilon_{\infty} \frac{\omega^2_{A_1(LO)} - \omega^2}{\omega^2_{A_1(TO)} - \omega^2}$$

Here, the high frequency dielectric permittivity ε_{∞} refers to the value of each material for the specific layer, as well as its longitudinal (LO) and transverse (TO) modes. Additionally, due to the chemical bonds being stablished between different atoms during the epitaxial growth at the interface between layers, there is an internal condition of residual strain which arises from the matching among distinct values of lattice parameters.[162] In order to guarantee the structural integrity of the nanostructure, each layer undergoes mechanical deformations of expansion and contraction aiming to stablish an approximate condition of homogeneity of interatomic distances along the superlattice while maintaining independent modes of vibration within each layer. This process, known as lattice coherence, defines the resulting lattice parameter of the

superlattice as dependent on the strain displayed by each material from different layers.[162] At equilibrium, the basal lattice parameter of an AlN/GaN superlattice can be then expressed by:

$$a_{SL} = a_0^{GaN}(\epsilon_{xx}^{GaN} + 1) = a_0^{AlN}(\epsilon_{xx}^{AlN} + 1)$$

Here, the assumed biaxial strain $\epsilon_{xx}^{i} = (a_{SL} - a_0^i)/a_0^i$, with $i = \{GaN, AlN\}$ is defined for each layer. In the absence of non-zero values of axial stress ($\sigma_{zz} = 0$), the axial lattice parameter c_0^i of each material is considered conserved and therefore a homogeneous axial lattice parameter c_{SL} for the superlattice is not stablished. In this nanostructure, the layers of gallium nitride $(a_0^{GaN} = 3.189\ \text{Å})$ are submitted to a compressive strain in order to match with the layers of aluminum nitride $(a_0^{AlN} = 3.113\ \text{Å})$, which feel a tensile strain.[190]

Figure 14 illustrates the phenomenon of lattice coherence in the vicinity of the interface between gallium nitride and aluminum nitride layers of an AlN/GaN superlattice. Each layer has its defined modes of transverse and longitudinal vibrations (ω_{TO}^i and ω_{LO}^i, with $i = \{GaN, AlN\}$), which frequency depends on the elastic properties of each individual material as well as on the level of strain that is felt in each layer.

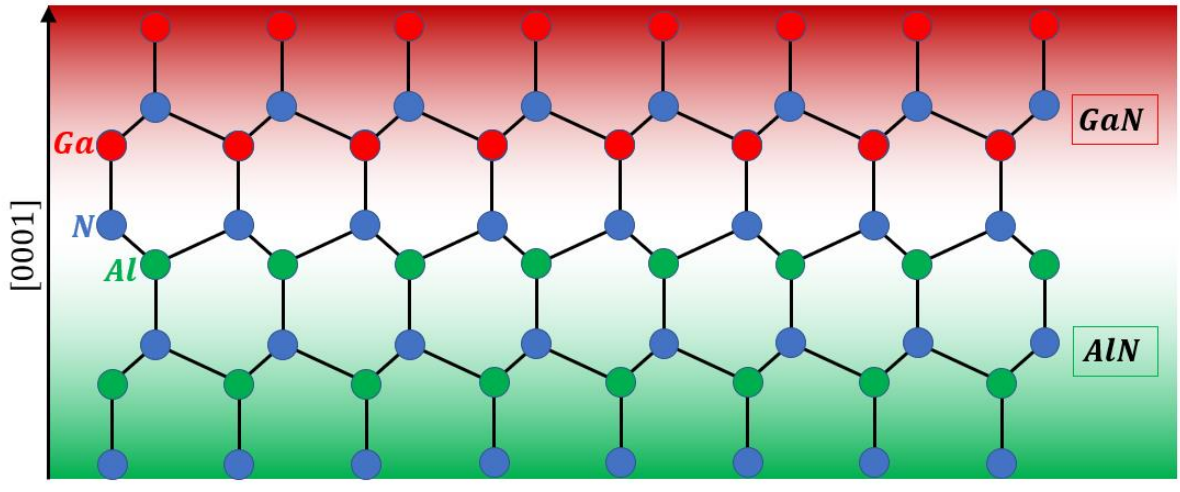

Figure 14 - Lattice coherence in AlN/GaN superlattice.

3.6 In-plane elastic energy minimization in *AlN/GaN* superlattices

The establishment of lattice coherence indicates a highly efficient crystalline growth, which is therefore dependent on the parameters used during the synthesis of the nanostructure, such as temperature, vacuum level, substrate affinity and flow of precursors from the effusion

cell.[46] In particular, the growth rate of a superlattice is affected by the amount of time the system is being exposed to the incoming precursors, which leads to either thicker or thinner individual layers. For a single period T of a AlN/GaN superlattice, constituted by the combination of one single layer of AlN and one single layer of GaN, with thicknesses given respectively by d_{AlN} and d_{GaN}, the average strain energy per period can be defined by:[46]

$$U_{SL} = \frac{1}{2}(d_{GaN}\sigma_{xx}^{GaN}\epsilon_{xx}^{GaN} + d_{AlN}\sigma_{xx}^{AlN}\epsilon_{xx}^{AlN})$$

In this relation, σ_{xx} and ϵ_{xx} are the biaxial stress and strain, respectively. The condition of minimum strain energy per period is met when the following relation is satisfied:[46]

$$\frac{d_{GaN}C_{GaN}\epsilon_{xx}^{GaN}}{d_{AlN}C_{AlN}\epsilon_{xx}^{AlN}} = -\frac{a_0^{GaN}}{a_0^{AlN}}$$

Here the constant $C_i = C_{11} + C_{12} - 2C_{13}^2/C_{33}$, with $i = \{GaN, AlN\}$ represents the basal Young's modulus $E = \sigma_{xx}/\epsilon_{xx}$ of each layer. The minimum value of strain in the layers is determined by the in-plane lattice parameter a_{SL} of the superlattice at equilibrium, which can be then expressed as dependent on the layers' thicknesses by the ratios:

$$a_{SL} = \frac{a_0^{AlN} + \frac{d_{GaN}a_0^{AlN\,2}C_{GaN}}{d_{AlN}a_0^{GaN}C_{AlN}}}{\frac{d_{GaN}a_0^{AlN\,2}C_{GaN}}{d_{AlN}a_0^{GaN\,2}C_{AlN}}} = \frac{a_0^{GaN} + \frac{d_{AlN}a_0^{GaN\,2}C_{AlN}}{d_{GaN}a_0^{AlN}C_{GaN}}}{\frac{d_{AlN}a_0^{GaN\,2}C_{AlN}}{d_{GaN}a_0^{AlN\,2}C_{GaN}}}$$

Therefore, the in-plane lattice parameter of a superlattice can be defined during its growth by choosing specific values of thicknesses for the layers of each material. This process is used in methods of strain engineering aiming to produce devices with a desirable value of strain, which for instance might bring benefits for the device's electronic and optical features, such as adjusting the conductivity and bandgap in piezoelectric nanostructures.[184]

3.7 Mechanisms of stress relief in *AlN/GaN* superlattices

The relation between the in-plane lattice parameter of the superlattice at equilibrium considers the ideal condition of growth in the absence of plastic deformations that might release the residual in-plane strain in the form of irreversible deformations or ruptures.[191] For a long time in the past during the development of techniques for efficient growths of III-

nitrides, structural defects were a considerable challenge to be overcame. The accumulated strain energy in the layers of a superlattice acts as an elastic potential energy which is readily available to be released in the form of structural defects. Morphological imperfections, such as threading dislocations may arise during crystalline growth producing the change in arrangement of atoms by promoting the glide or twisting motion of atomic layers. This process leads to structural misfits along the crystalline lattice, which may or not be propagated across layers of different materials. At a macroscale, it is possible to observe the phenomenon of cracking, often promoted by the relaxation process of releasing tensile strain.[192] As a result, the atomic layers situated close to the vicinity of cracks have their lattice parameters more relaxed to its non-stressed condition than atomic layers located far away from cracks, which are still severely submitted to the equilibrium value of in-plane strain.[192,193] The gradient of stress along cracked crystals can be evaluated by using the technique of Raman at the micrometric scale, known as micro-Raman, which uses a microscope to reach a spatial resolution in the order of one micrometer. In particular, the phenomenon of formation of nets of microcracks has been reported for AlN/GaN superlattices occurring along the hexagonal crystallographic directions $[2\bar{1}\bar{1}0]$, $[\bar{1}2\bar{1}0]$ and $[\bar{1}\bar{1}20]$ oriented $2\pi/3$ radians from each other, as shown in Figure 15.[192,193]

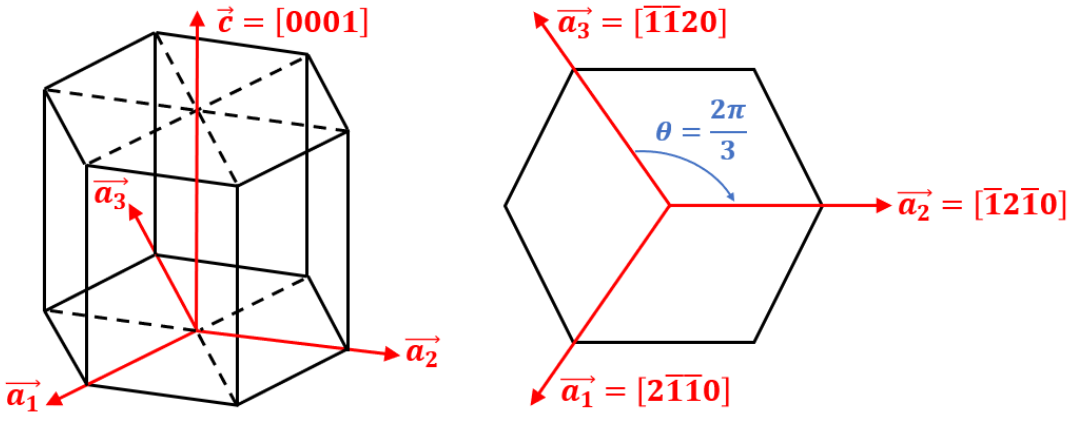

Figure 15 - Perspective and planar view of the rhombohedral system of axes, evidencing the unitary vectors $\overrightarrow{a_1}$, $\overrightarrow{a_2}$, $\overrightarrow{a_3}$ and $\vec{c}$ representing the relevant families of planes.

During the growth, structural dislocations may occur in the layers' interface due to the mechanical matching between interatomic distances of different materials. When cooling down after the synthesis, the crystal may suffer plastic relaxation by fracturing areas between cracks, which is more usual to occur in ultrathin layers of nanostructures.[191] The fracture propagation is most likely to occur along the direction that provides the maximum rate for releasing the

accumulated elastic energy. Considering the elastic anisotropy of wurtzite crystals and the stressed condition faced by the nanostructure layers perpendicularly to the direction of epitaxial growth, a hexagonal network of microcracks can be promoted throughout the superlattice.

Chapter 4: Research methodology

In this research, the technique of micro-Raman Spectroscopy was used to determine the local strain of a set of six 30-period AlN/GaN superlattices, differing among each other by the thickness of the layers constituted by gallium nitride. The superlattices were produced using the Molecular Beam Epitaxy (MBE) technique for nitrides, and were analyzed by X-Ray Diffraction in order to verify the average strain and layers' thicknesses of each sample. A correlation model between strain and Raman shift was developed and compared with empirical data. The morphology of the aluminum and gallium nitrides layers was studied using the Transmission Electron Microscopy technique, and the composition of each layer was analyzed using Energy-Dispersive X-Ray Spectroscopy. Complementary, the optical bandgap of each superlattice was studied using the luminescent emission acquired by the Photoluminescence technique. The following diagram in Figure 16 illustrates the techniques employed in this research.

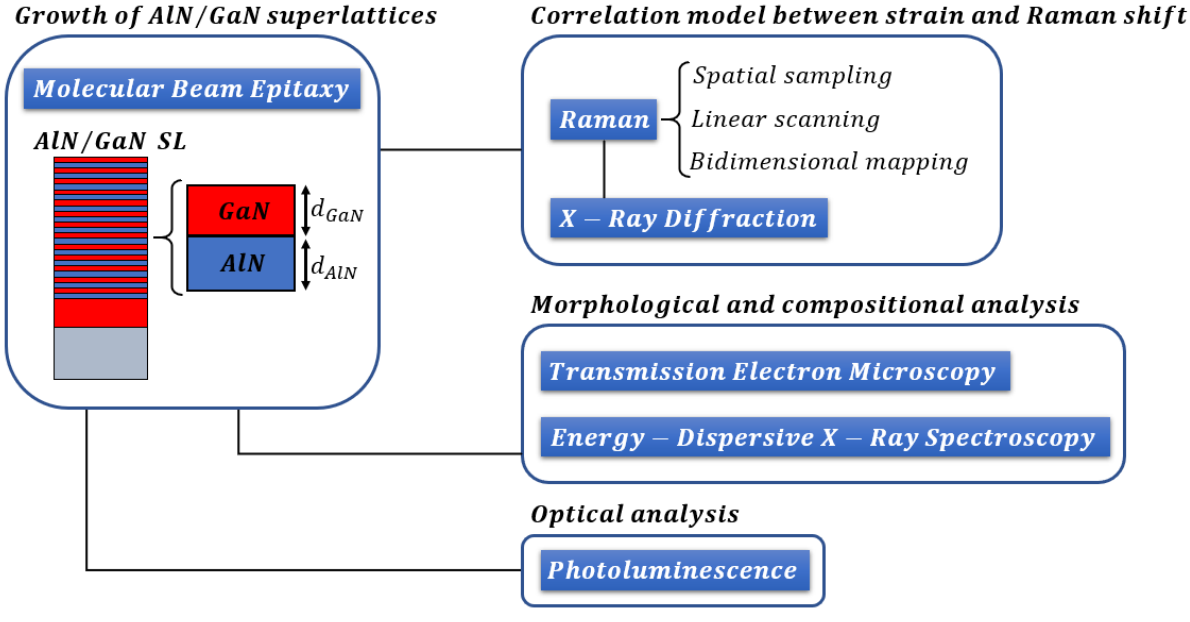

Figure 16 - Techniques used in this research.

4.1 Molecular beam epitaxy

For the last decades, molecular beam epitaxy (MBE) has been a remarkably useful technique in the successful production of nanostructured materials. It has been effectively employed in the fabrication of a large variety of compounds and structures, such as $GaAs$, $InAs$, $GeSn$, ZnS, and many others, including the III-nitrides AlN and GaN.[114] One of the main advantages of using the MBE technique, and its variations, is associated with its high efficiency in yielding accurate growth of homogeneous atomic planes at sub-monolayer scale, which is highly relevant when developing nanostructured devices which functionality is based on quantum scale effects. Additionally, the growth can be monitored in situ by using the Reflection High-Energy Electron Diffraction ($RHEED$) technique. One fundamental concept required in the MBE technique is to provide an ultrahigh vacuum environment for precursors to react only when reaching the substrate.[179] In special, the technique known as Plasma-Assisted Molecular Beam Epitaxy ($PAMBE$) has being successfully used in the synthesis of nitrides.[114] In this method of growth, the reactant nitrogen is activated from its molecular form before its interaction with the group-III element. It is made by using methods such as Radiofrequency (RF) and Electron Cyclotron Resonance (ECR). The sources of gallium and aluminum atoms are usually produced in thermal evaporators known as Knudsen effusion cells (K-cell), which reactant flux can be precisely controlled by the temperature at the K-cell's crucible. The reactants are directed towards the substrate, which can be rotated to incite homogeneous growth at a desired temperature. Figure 17 displays the fundamental components of a MBE system.[114]

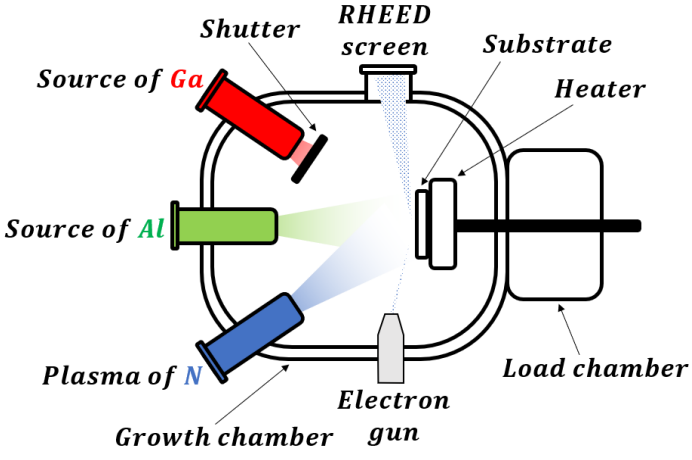

Figure 17 - Components of a MBE system.

In this research, six 30-period AlN/GaN superlattices were grown on GaN templates using the plasma assisted molecular beam epitaxy technique ($PAMBE$). Figure 18 presents photos of the MBE system ($Veeco$, model $Gen\ II$) located at the Institute for Nanoscience and Engineering of the University of Arkansas.

Figure 18 - Photos of the MBE system: growth chambers (left) and power controller (right).

Commercial GaN templates ($Kyma\ Technologies$) were used as substrates in the MBE growths in order to provide a lattice-friendly surface during the epitaxial synthesis. In Figure 19, the unscaled diagram illustrates the structure of the GaN templates, constituted by a $5\ \mu m$-thick $[0001]$-oriented and n-type unintentionally doped Ga-face GaN, grown by Hydride Vapor Phase Epitaxy ($HVPE$) on top of c-plane sapphire (Al_2O_3) substrate using an intermediate layer of approximately $25\ nm$-thick Al-face AlN deposited epitaxially by Plasma Vapor Deposition of Nanocolumns ($PVDNC$), which facilitates the high quality growth of GaN

.

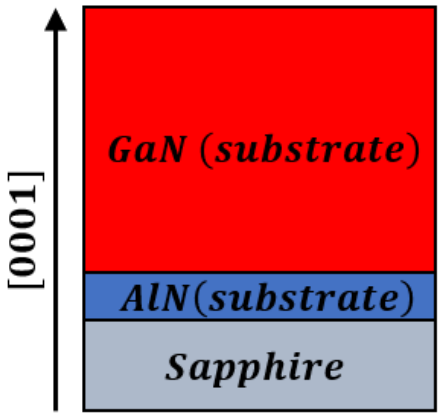

Figure 19 - Structure of the GaN template ($Kyma\ Technologies$) used as a substrate for the growth of the superlattices by MBE.

As required for the MBE growth, the $2\ inches$-wide wafers of GaN template were mechanically cut in quarters using a water guided dicing saw ($NanoFab$). The quarters were then cleaned in acetone (CH_3COCH_3) for $2\ min$ using an ultrasonic cleaning machine ($NanoFab$), followed by $2\ min$ in static solution of methanol (CH_3OH), $2\ min$ in static solution of isopropanol ($CH_3CHOHCH_3$) and then finally dried using a soft blow of nitrogen gas (N_2). In preparation for growth, each quarter was degassed in the initial-chamber of the MBE system at 200℃ at a pressure of approximately $10^{-8}\ Torr$ for $60\ min$. The quarter was then transferred to the middle-chamber at a pressure of approximately $10^{-10}\ Torr$ for $60\ min$ at 300℃. Finally, the quarter was transferred to the main-chamber at 830℃ at a base pressure of approximately $10^{-11}\ Torr$ for $60\ min$, followed by a constant flux of $0.5\ sccm$ of nitrogen plasma. The ultrahigh vacuum environment in the MBE system is used to remove any impurity or contaminant that might compromise the high quality of the epitaxial growth. Prior to the superlattice growth, an initial $180\ nm$-thick buffer layer of GaN was grown on top of each GaN template at a rate of approximately $3\ nm/min$ at a stable pressure of $10^{-6}\ Torr$. Afterwards, 30 periods of alternated AlN/GaN layers were epitaxially grown onto the buffer layer, maintaining the thickness of the AlN layers constant for all samples at approximately $3\ nm$, and modifying the thickness of the GaN layers from approximately under than $1\ nm$ up to over than $7\ nm$ for different samples. The software $MOLLY$ ($Veeco$, version 2000) was used to control the periodic growth. Table 3 summarizes the nominal values of the deposited thickness of AlN and GaN layers for each sample determined in situ using $RHEED$:

Table 3 - Nominal thicknesses of AlN and GaN for each sample.

Sample	***AlN* (*nm*)**	***GaN* (*nm*)**
S1	3.40	0.25
S2	3.35	1.35
S3	3.35	2.95
S4	3.40	4.50
S5	3.20	5.70
S6	3.30	7.30

All the six superlattices ($S1$, $S2$, $S3$, $S4$, $S5$ and $S6$) were grown under the same conditions of temperature ($T_{K-\text{cell}}^{AlN} \approx 1055°C$, $T_{K-\text{cell}}^{GaN} \approx 935°C$), pressure and flow of reactants, differing only in respect to the time of exposition to the gallium effusion K-cell ($t_{open}^{AlN} \approx 45\ s$, $t_{open}^{GaN} \approx 25\ s$ ($S1$) to $150\ s$ ($S6$)). Therefore, the sample $S1$, which remained less time exposed to the gallium source than sample $S2$, has a relatively thinner layer of GaN. Additionally, in order to facilitate the formation of a flat interfacial surface between layers of AlN and GaN and avoid the segregation of impingent Al and Ga atoms, a waiting period of $15\ s$ was respected before starting a new layer. The following unscaled diagram in Figure 20 illustrates the structure of the AlN/GaN superlattices, which can be applied for all the samples analyzed in this study:

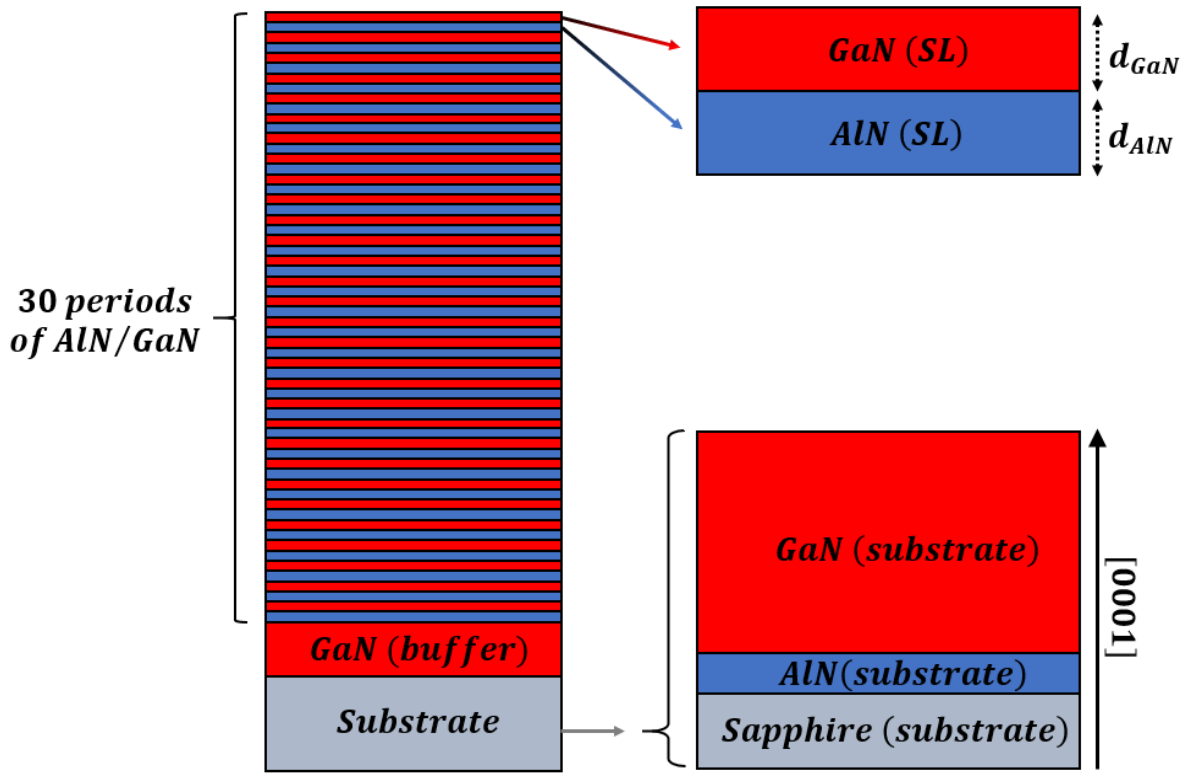

Figure 20 - Structure of the AlN/GaN superlattices grown in this study.

4.2 Micro-Raman spectroscopy

The technique of micro-Raman Spectroscopy allows the investigation of Raman active modes of materials within a spatial resolution in the order of one micrometer along the analyzed surface. It can be accomplished by using an appropriate microscope, which is conjugated with the spectroscopic system. This level of resolution is suitable for methods of spatial sampling, linear scanning and planar mapping of materials with interesting features evidenced in the micrometric scale.[192] During a basic micro-Raman experiment, the investigated material is illuminated by an incident light through a microscope using an appropriated set of lenses, mirrors and filters. The scattered light is collected by a spectrometer and compared to the original incident light information. The technique can be performed at room temperature and atmospheric pressure, and the quality of the studied material remains intact throughout the experiment. Different orientations of polarizations between incident and scattered light can be used in order to impose preference for specific vibrational modes while blinding the system from others.[23] In particular, the Porto notation $A(B,C)D$, developed by the Brazilian physicist Sergio Pereira da Silva Porto in 1966, is used to express the geometry used

in Raman experiments.[194] In this notation, A and D represent respectively the propagation direction of the incident and scattered light, while B and C represent their respective direction of polarization. Figure 21 presents the fundamental components of the experimental system of micro-Raman Spectroscopy using the backscattering geometry $Z(-,-)\bar{Z}$, in which the propagation of the incident and scattered light is antiparallel, and there is no imposed control of polarization.

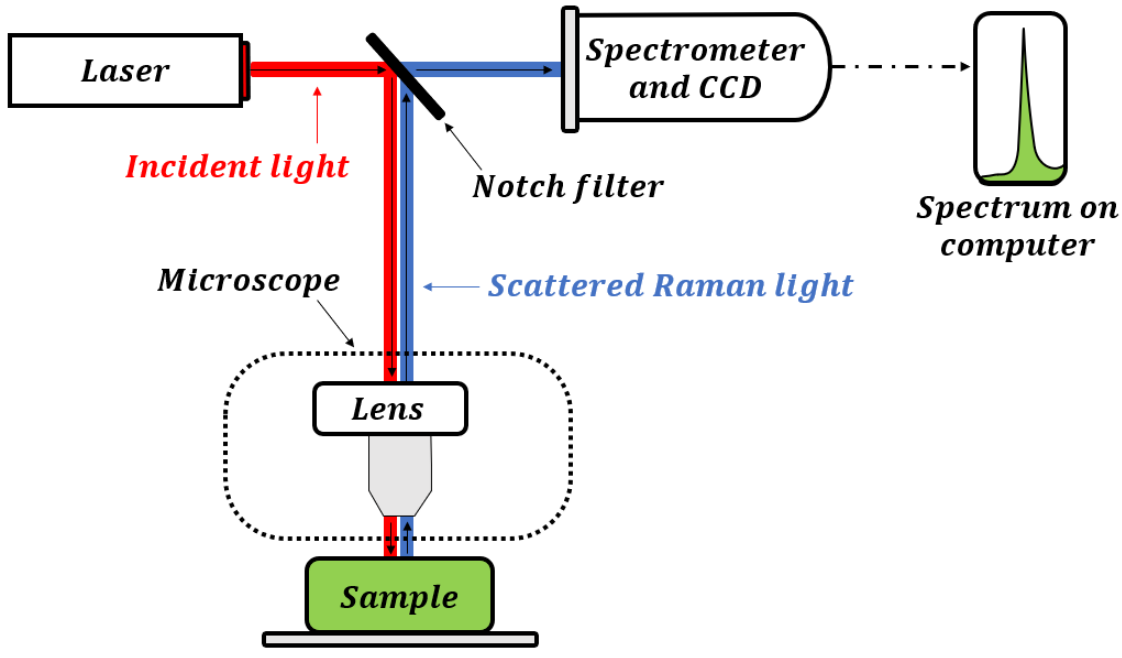

Figure 21 - Components of a micro-Raman system.

In the figure, the notch filter reflects the undesired light originated in the elastic Rayleigh scattering, allowing only the Raman light to reach the spectrometer, which using a charge coupled device (CCD) converts the luminous signal into storable data. The computer is used to plot the Raman spectrum evidencing the intensity associated to the investigated range of Raman shift.

In this research, the micro-Raman measurements were performed at the Raman Laboratory of the Optical Characterization Facility ($Nano/UARK$). The Raman data were acquired at room temperature using the backscattering configuration defined by the Porto notation $Z(-,-)\bar{Z}$, with both the incident and scattered light beams propagating along the z-direction, oriented parallel to the epitaxial growth axis $[0001]$ of the superlattice. A $632.8\ nm$ $He-Ne$ laser ($Melles\ Griot$, model $05-LPL-915070$) was employed operating with a resulting excitation power of $5\ mW$ on the surface of the sample. The spot of the incident laser

light was adjusted by the focus controllers of an optical microscope ($Olympus$, model $BX41$) using an $100x$ magnification objective lens ($Olympus$, model $MPLanN100x$) and a digital camera ($uEye$). The light of a high-power lamp ($Euromex$, model $EK - 1$) was employed for acquiring images of the surface of each sample. Figure 22 presents a picture of the excitation and detection stations of the micro-Raman system indicating the components of the experimental set up.

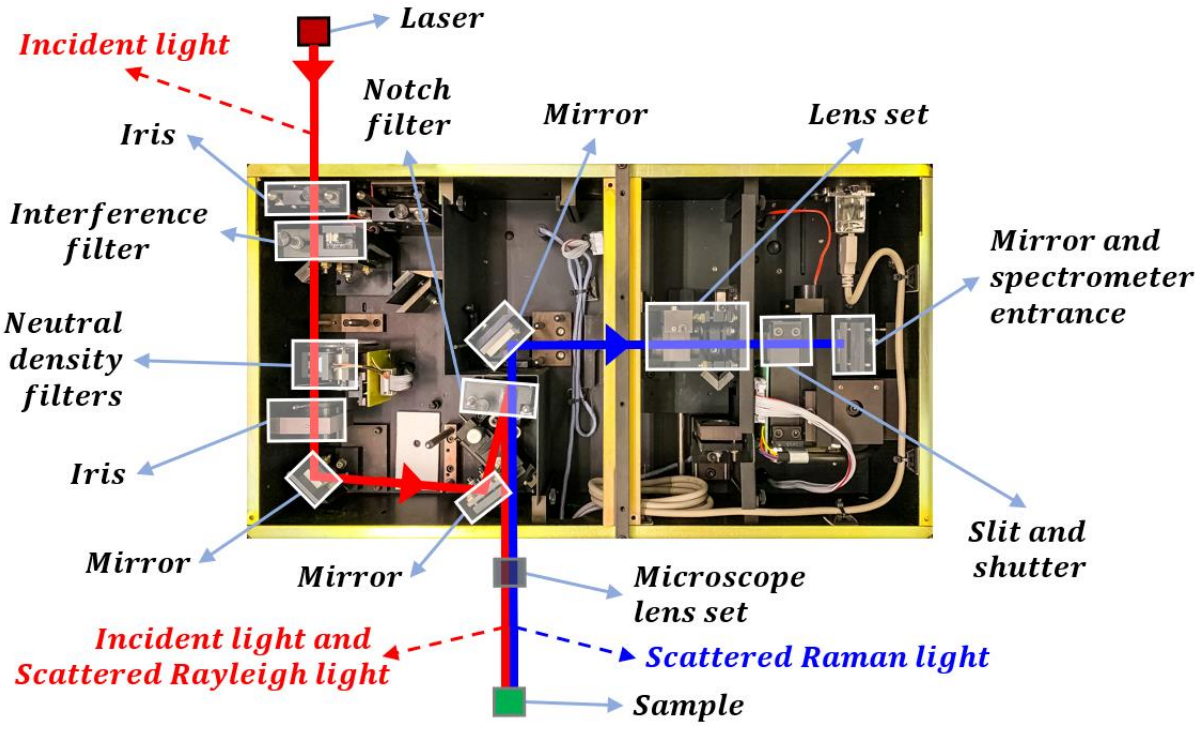

Figure 22 - Stations of sample excitation and signal collection used in the micro-Raman measurements.

The scattered Raman light was collected by a $0.75\ m$ long spectrometer ($Horiba\ Jobin - Yvon$, model $LabRam\ HR - 800$) equipped with a thermoelectrically cooled charge coupled device camera ($Andor$, model $DU420A - OE - 325$). The spectrometer system allows optical detection along the spectral range from $100\ cm^{-1}$ to $4000\ cm^{-1}$ with a spectral resolution of up to $1.5\ cm^{-1}$ and $1\ cm^{-1}$ of accuracy. A notch filter ($Horiba\ Jobin - Yvon$, $633\ nm$) was placed before the light collection in order to remove the undesirable elastically scattered laser light. The micro-Raman measurements were conducted using the software $LabSpec\ 5$ ($Horiba\ Jobin - Yvon$) operating under background correction, with the signal being acquired five times before averaged and stored. A time of exposition of $100\ s$ was employed in each cycle, with an aperture of $200\ \mu m$ at the

spectrometer entrance slit while using a $1800\ l/mm$ dispersion grating. The Raman data were mostly acquired in the spectral region between approximately $500\ cm^{-1}$ and $800\ cm^{-1}$, as suitable for the desirable range of analysis of gallium nitride and aluminum nitride, and additionally in the broader range between $100\ cm^{-1}$ and $2000\ cm^{-1}$ for further investigations. In addition to the basic components, the employed Raman system also has a set of mechanical irises used to verify beam alignment and collimation, an interference filter ($Horiba\ Jobin-Yvon$, $633\ nm$) to avoid incidence impurity, a set of neutral density filters ($Horiba\ Jobin-Yvon$) for excitation attenuation and the slit shutter used for background data acquisition. The same experimental configuration was employed for all the samples.

4.3 X-ray diffraction

Since the discovery of light diffraction, this phenomenon has allowed the development of several technologies currently used in scientific, medical and commercial fields. In particular, the technique of X-Ray Diffraction (XRD) has become universally employed as a reliable tool for structural analysis in atomic scale.[195] In an XRD experiment, the sample is illuminated with x-ray radiation, usually produced by a cathodic tube.[196] The incident x-ray light is diffracted by the atomic arrangement of the analyzed material once the radiation's wavelength is in the same order of spatial scale as the investigated material's interatomic distances. Figure 23 illustrates the main components of an XRD system, constituted by a source of x-ray radiation and a detector. During the experiment, the x-ray source and the detector are symmetrically rotated, and the intensities and distances associated to the interference pattern are recorded by the detector for the studied angular range.[196]

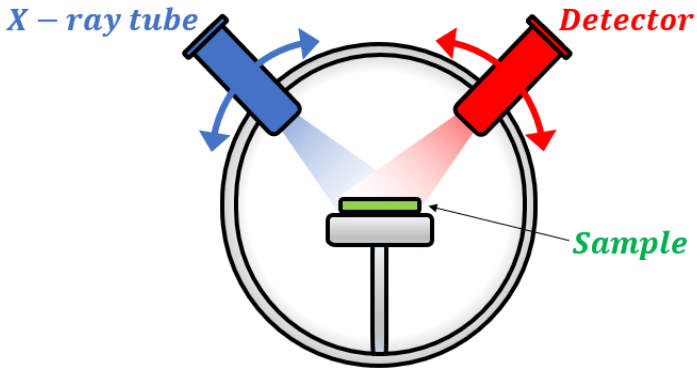

Figure 23 - Components of an XRD system.

In this research, the XRD analyses were performed at the XRD Laboratory of the Materials Characterization Facility ($NANO/UARK$) using a high resolution XRD diffractometer ($Malvern\ Pananalytical\ X'Pert\ Pro\ MRD$), which is equipped with a $1.6\ kW\ Cu\ K\alpha_1$ X-ray tube, a standard four-bounce $Ge(220)$ monochromator and a detector ($PIXcel$). The software $X'Pert$ ($Pananalytical\ X'Pert\ Data$) was used during the XRD analyses, investigating in the 2θ range between approximately 10 and $20\ degrees$, as suitable for composing the reciprocal space maps of each superlattice across the asymmetric $\bar{1}\bar{1}24$ and $\bar{1}015$ reflections.

4.4 Transmission electron microscopy

The visualization of small specimens such as viruses, DNA nucleotides, and atomic monolayers, requires extremely high levels of spatial resolution, usually in the order of million times of magnification.[196] Optical microscopes, which are suitable to observe objects using under a thousand times of amplification, are unable to resolve features that are smaller than the wavelength of visible light. This fact motivated the German physicist Ernst August Friedrich Ruska in 1933 to design a microscope based on beam of electrons, instead of photons, in order to achieve better imaging resolution with wavelengths a thousand times smaller due to the electronic wave-particle duality.[196] In a usual Transmission Electron Microscopy (TEM) system, an electronic beam produced by thermionic emission is accelerated through an electric potential and then focused using a set of electromagnetic lenses onto the analyzed material. The beam is transmitted throughout the material and then collected by a detector to produce the contrast image. The studied material must be micrometrically thin in order to enhance the imaging contrast, therefore it must be architected as a doubly polished ultrathin layer, which in the case of crystals is usually achieved by processes of mechanical polishing and ion-milling. The diagram shown in Figure 24 illustrates the main basic components of a TEM system.[196]

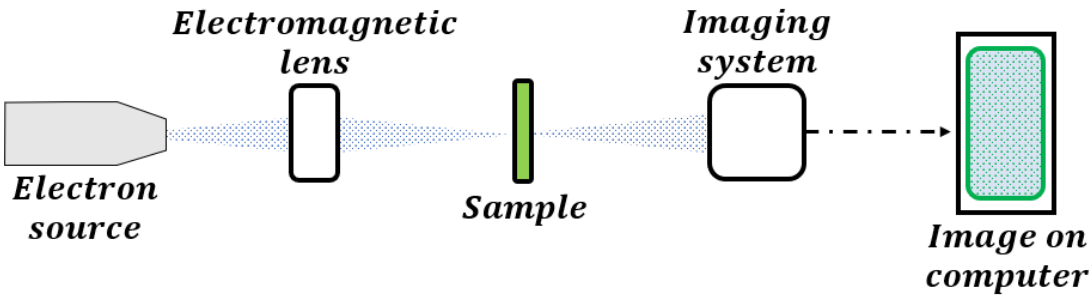

Figure 24 - Components of a TEM system.

In this research, the TEM analysis was performed at the TEM Laboratory of the Arkansas Nano-Bio Materials Characterization Facility ($Nano/UARK$). As required for TEM sample preparation, two rectangular slices of $2.50\ x\ 1.25\ mm$ were mechanically diced from the analyzed superlattice using a water guided dicing saw ($NanoFab$). The slices were cleaned in solution of acetone at $90℃$ for $10\ min$, and then dried using flow of nitrogen gas. An epoxy adhesive resin ($Epoxy\ Technology, Inc.$) was then prepared to be used as glue between the slices of the superlattices. For the preparation, a solution constituted by ten drops of bisphenol f (code $EPO - TEK\ 353ND\ Part\ A$) and one drop of imidazole (code $EPO - TEK\ 353ND\ Part\ B$) was heated at $180℃$ for $10\ min$. A microdroplet was collected from the resulting solution and deposited on top of one of the superlattice's slices, followed by its coverage by the other slice in a sandwich architecture. The double layer structure was pressed using a metallic clamp and heated at $180℃$ for $60\ min$, and then cooled down for $30\ min$. Figure 25 illustrates an unscaled diagram of the double layer structure connected by the epoxy adhesive resin:

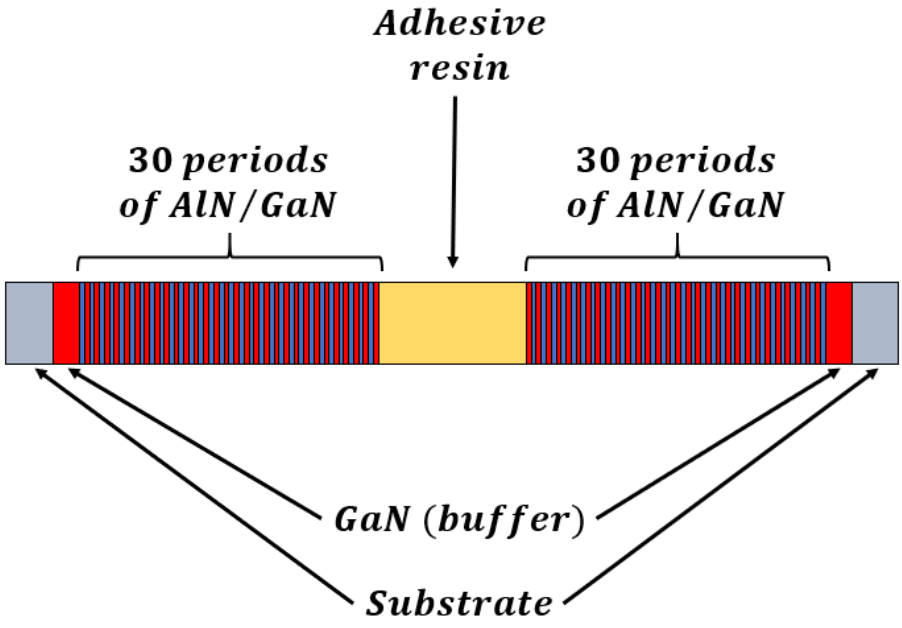

Figure 25 - Double layer structure used in the TEM analysis.

After the natural cooling process, the double layer structure was removed from the clamp and then attached to a metallic holder containing melted wax, which had been preheated at $220℃$ for $10\ min$. After $2\ min$ on heater at $220℃$, the holder containing the double layer was removed from the heated plate to cool down for $30\ min$. After the cooling process, the initial height ($\sim 1250\ \mu m$) of the double layer structure was verified using the micrometer of the polishing machine (*Allied High Tech Products, Inc.*). The holder was then attached to the polishing machine in order to reduce its height until approximately to $30\ \mu m$, which was made by mechanically polishing the double layer structure using its friction over a set of diamond lapping films (*Allied High Tech Products, Inc.*) in a steady rotation of $30\ rpm$. To avoid unintentional heating and rupture of the double layer structure, the polishing process was performed using a polishing lubricant (*Allied High Tech Products, Inc.*) for $10\ min$ employing a $6\ \mu m$-lapping film, followed by $10\ min$ using a $1\ \mu m$-lapping film and finally for $10\ min$ using a $0.5\ \mu m$-lapping film, always washing the holder containing the double layer structure in deionized water, drying it with nitrogen gas and replacing the lubricant between each change of film. The holder was then placed in a solution of acetone in order to degrade the solid wax and detach the double layer from the polishing holder. Once detached, the double layer was flipped and attached to the holder preheated at $220℃$ for $10\ min$ using melted wax, so that the polished side of the double layer was facing the wax. The holder was replaced at the polishing machine, and the double layer was polished for $10\ min$ using the

$6\ \mu m$-lapping film. After changing to the $1\ \mu m$-lapping film, the polishing process continued until the height of the double layer reached the value of approximately $30\ \mu m$, finally followed by $2\ min$ of polishing using the $0.5\ \mu m$-lapping film. The holder was then washed with deionized water and dried with nitrogen gas.

As the final step in the preparation for TEM analysis, a beryllium grid ($Spi\ Supplies$) was attached to the polished surface using two microdroplets of an strain gage adhesive ($Micro\ Measurements - Vishay\ Precision\ Group, Inc.$, model $M - bond - 610$), aiming to prepare the double layer for the process of ion milling. The holder containing the structure was then heated at $220℃$ for $140\ min$, and then cooled down for $30\ min$. Afterwards, the holder was placed in a solution of acetone to degrade the remaining solid wax. After detached from the holder, the beryllium grid containing the polished double layer was attached to the ion milling sample frame, and inserted in the ion milling chamber ($Fischione\ Instruments - Low\ Angle\ Ion\ Milling\ \&\ Polishing\ System$, model 1010). After reaching the pressure of $10^{-5}\ Torr$ inside the ion milling chamber, a $15°$-inclined argon ion beam was applied to the polished double layer for a period of $10\ min$. The double layer was then checked in optical microscope for the occurrence of a hole inside the region of the adhesive resin, repeating the process of ion milling in intervals of $10\ min$ until the formation of a well defined hole, which is an indicative that the polished double layer might be thin enough to be analyzed using the electronic microscope. The software $Ion\ Mill$ ($E.A.Fischione$, version $2.4.0$) was used to control the process of ion milling. After $4h$ of ion milling, a hole was evidenced in the adhesive resin, and the beryllium grid containing the polished double layer was inserted in the TEM chamber ($Field\ Electron\ and\ Ion\ Company$, model $Titan\ 80 - 3000$) at a pressure of approximately $10^{-7}\ Torr$. The software $TEM\ Imaging\ \&\ Analysis$ ($Field\ Electron\ and\ Ion\ Company$) was used to acquire the TEM images. The high resolution TEM system employed a field emission gun operating at $300\ kV$ allowing the acquisition of images by high-angle annular dark-field imaging ($HAADF$) with a spatial resolution of $0.1\ nm$, which is suitable for atomic scale investigations.

4.5 Energy-dispersive x-ray spectroscopy

During the process of sample imaging using electron microscopy, the atomic electrospheres of the analyzed material are bombarded with incident electrons, which are

highly energetic and capable of ejecting inner shell electrons from the material.[196] In these events, the ejected electrons leave behind a vacancy in their original energy level that is then occupied by another electron from a higher energy level by emitting a photon of x-ray radiation, which energy equals to the energetic difference between the consecutive atomic energy levels characteristic of the material.[190] By using an energy dispersive spectrometer, the emitted photons can be then analyzed and used as an atomic fingerprint, in a technique known as Energy-Dispersive X-Ray Spectroscopy (EDS).[196] This technique has been extensively employed to acquire quantitative elemental data of materials at atomic scale, representing a reliable tool for chemical characterization. Figure 26 illustrates a diagram of the main components of an EDS system.

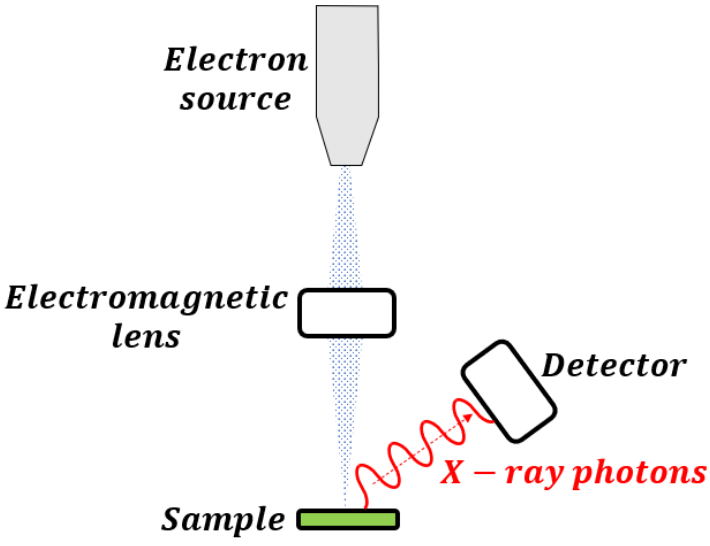

Figure 26 - Components of an EDS system.

The EDS system used in this research was part of the high resolution TEM system ($Field\ Electron\ and\ Ion\ Company$, model $Titan\ 80-3000$). This system contains a lithium-drifted silicon detector ($EDAX$, SDD) which allows measuring X-ray photons with a spectral resolution of approximately $0.136\ eV$. The software $TEM\ Imaging\ \&\ Analysis$ ($Field\ Electron\ and\ Ion\ Company$) was used to acquire the EDS elemental data.

4.6 Photoluminescence spectroscopy

The most remarkable feature of gallium nitride-based LED devices is associated to its blue light emission, which can be controlled using methods of bandgap engineering.[180] In

special, gallium nitride is a direct band gap semiconductor, which means that the least energetic electronic transition between valence and conduction bands does not require change in electronic momentum to be performed. It implies that differently than indirect band gap semiconductors, such as silicon for instance, gallium nitride systems can produce light more efficiently because the events of electronic excitation and deexcitation happen without additional lattice interactions, such as with phonons, which might affect and compromise the device's overall energy consumption.[180] In order to study the light emitted during events of electronic deexcitation, the technique of Photoluminescence Spectroscopy (PL) has been successfully employed in the analysis of a wide variety of materials. Figure 27 illustrates the diagram of the main components of a PL system.

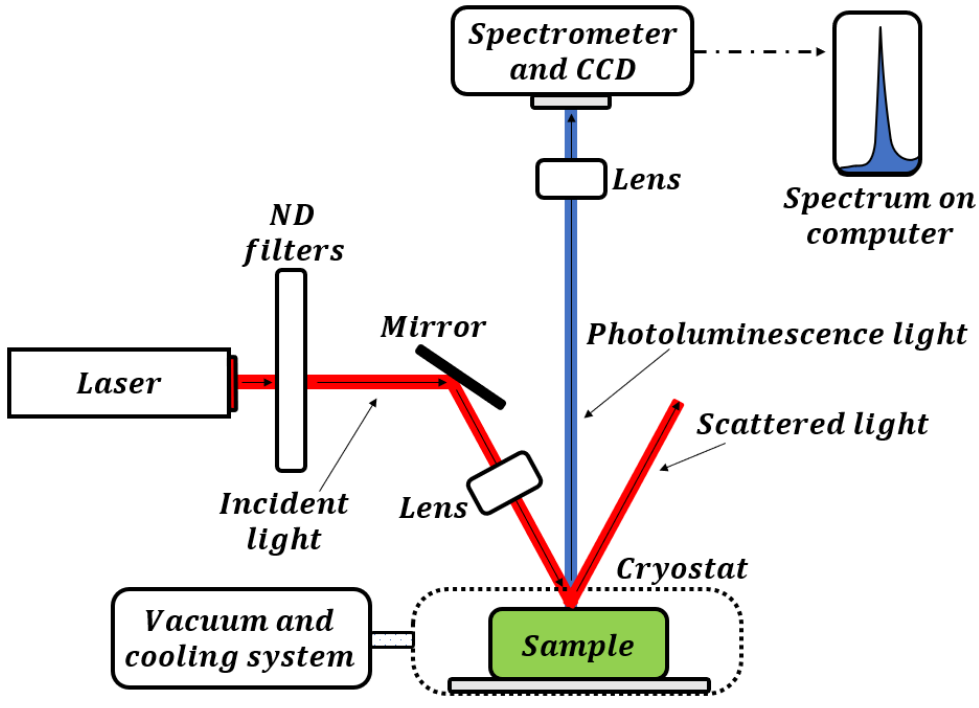

Figure 27 - Components of a PL system.

In the PL technique, photons that are more energetic than the material's band gap energy are absorbed by the material promoting the electronic transition of electrons from the semiconductor's valence band to its conduction band. This process leaves behind unoccupied states, known as holes, in the original electronic energy level in the valence band. When the electrons relax back from the conduction band to their original state in the valence band, the process of deexcitation emits photons which energy is equivalent to the material's band gap. In particular, investigations on the optical emissions of III-nitride superlattices have shown the existence of a dependence between features of the superlattice, such as the thickness of its

layers, and the resulting bandgap energy evidenced in the PL characterization. This dependence is substantially influenced by the quantum-confined Stark effect, which is associated to the internal electric field of each layer modifying the band energy diagram of the material. This effect, evidenced as a shift in PL emission, has been revealed to be highly dependent on the quantum well thickness of superlattices, as well as on the magnitude of its internal electrical field along the nanostructure.[184]

In this research, the PL measurements were performed at the Photoluminescence Laboratory of the Optical Characterization Facility ($Nano/UARK$). As a nondestructive method of analysis, the PL technique did not require any special sample preparation. The sample was loaded into a closed-cycle helium cryostat system and attached to the sample holder using an appropriate adhesive paste. The cryostat was sealed using two shields and a pressure of $10^{-5}\ Torr$ was maintained during the PL experiments using a vacuum pump ($Varian$, model $Turbo-V-70$). The PL data were acquired at $10\ K$ using an ultraviolet laser light of $266\ nm$ as luminous excitation, which is equivalent to an energy of approximately $4.7\ eV$. This excitation energy is suitable for GaN once its expected band gap for its bulk form is approximately $3.5\ eV$ at low temperatures, therefore this ultraviolet laser would be able to promote electronic transitions throughout the band gap. Additionally, it has been reported that nanostructured GaN displays a redshift towards lower energies, emitting in the near ultraviolet spectral range, which could be also evidenced in this PL setup. The $266\ nm$ laser light was produced by a $532\ nm$ laser ($Coherent$, model $Verdi\,V-10$) using a resonant frequency doubling unit ($Coherent$, model $MBD-266$). A $266\ nm$ line filter ($MKS\ Newport$, model $10LF10-266$) was placed in the path of the excitation light to reflect any undesirable residue of the $532\ nm$ light by displaying a transmission center at $\sim 266\ nm$, with a full width half maximum of $\sim 10\ nm$. A set of lenses ($MKS\ Newport$, model SPX) suitable for the ultraviolet range was used for focusing the light beam. Also, a set of ultraviolet-friendly neutral density filters ($ThorLabs$, model $NDUV$) was used for attenuating the excitation power intensity during power-dependent PL measurements. In the absence of neutral density filters, the resulting power intensity of the millimetric beam at the surface of the sample inside the cryostat presented a value of approximately $9.2\ mW$. The PL signal was collected by a spectrometer ($Acton\ Research\ Corporation$, model $300i$) connected to a charge coupled device (CCD, $Roper\ Scientific$, model $7346-0005$), which was maintained cooled down at -100°C during all the PL experiments. The sample was cooled down using a compressor (

$APD\ Cryogenics, Model\ HC-4$) and the temperature was verified using a temperature controller ($LakeShore, Model\ 330$). The software $WinSpec32$ ($Priceton\ Instruments$) was used to obtain and save the PL data, which were acquired in the ultraviolet and visible spectral range between approximately $280\ nm$ and $620\ nm$, energetically equivalent to the window from $4.4\ eV$ to $2.0\ eV$.

4.7 Research layout

The techniques and experimental methodologies described in this chapter were used to study the morphology (TEM), composition (EDS), structure (XRD), luminescence (PL) and strain condition ($micro\text{-}Raman$) of six 30-period AlN/GaN superlattices fabricated at nanoscale (MBE). In special, using the advantage of the microscale sampling resolution of the $micro\text{-}Raman$ technique, allied with the high crystallographic accuracy of the XRD results, a correlation model based on lattice coherence for superlattices was developed. It made possible the study of the gradient of strain along the AlN and GaN layers by tracking the vibrational modes of each nitride. These findings are described in the following chapter, in addition to the study of the luminescent emission of each superlattice as a dependence on the thickness of the GaN layers.

Chapter 5: Results and discussion

This chapter presents an alternative method for studying in-plane strain distribution in nanostructures at microscale. Firstly, the morphology of a 30-period AlN/GaN superlattice is investigated using electronic microscopy at atomic monolayer scale, and the concentration of aluminum and gallium is evaluated along layers. Then, the AlN and GaN layers' thicknesses and their respective in-plane lattice constant of a set of superlattices are determined using x-ray diffraction, and compared to values of strain calculated using the Raman shift of a nonpolar mode in the scope of the traditional linear formulation. A more precise method of strain analysis at microscale is then elaborated in the form of a nonlinear model between strain and Raman shift, being subsequently tested with results reported in the literature. The nonlinear method is then used to investigate the one- and two-dimensional distribution of strain along

each superlattice at the micrometric scale and compared to values reported using x-ray diffraction.

5.1 Morphological analysis

The technique of Transmission Electron Microscopy (TEM) was employed as described in $Chapter\ 4$ in order to verify the morphology of the AlN and GaN layers, as well as to investigate the interfacial surface between layers. The superlattice $S6$, which is the one that contains the thickest GaN layers among the samples, was chosen for electronic microscopy due to its largest separation between consecutive interfacial surfaces, which facilitates the study of any possible compositional gradient. The morphology of this representative superlattice is considered analogous to the remaining superlattices, differing among each other by the layers' thicknesses. Figure 28 presents the electronic microscopy of sample $S6$, evidencing the superlattice structure containing alternated layers of gallium nitride (brighter layers) and aluminum nitride (darker layers), as well as the buffer layer. The image represents a cross-sectional view of the superlattice along the crystalline plane $(1\bar{1}00)$, defined parallel to direction $[0001]$. The difference in contrast observed using electronic microscopy is dependent on the electronic density characteristic of the region of the material under analysis, and in particular for AlN/GaN superlattices, here layers containing aluminum atoms appear darker due to their lower effective atomic number ($Z_{AlN} = 13$) in comparison to the layers containing gallium atoms ($Z_{GaN} = 31$), which appear brighter. The electronic microscopy indicated homogeneity along layers of the superlattice, as well as a well defined interface between layers of different materials.

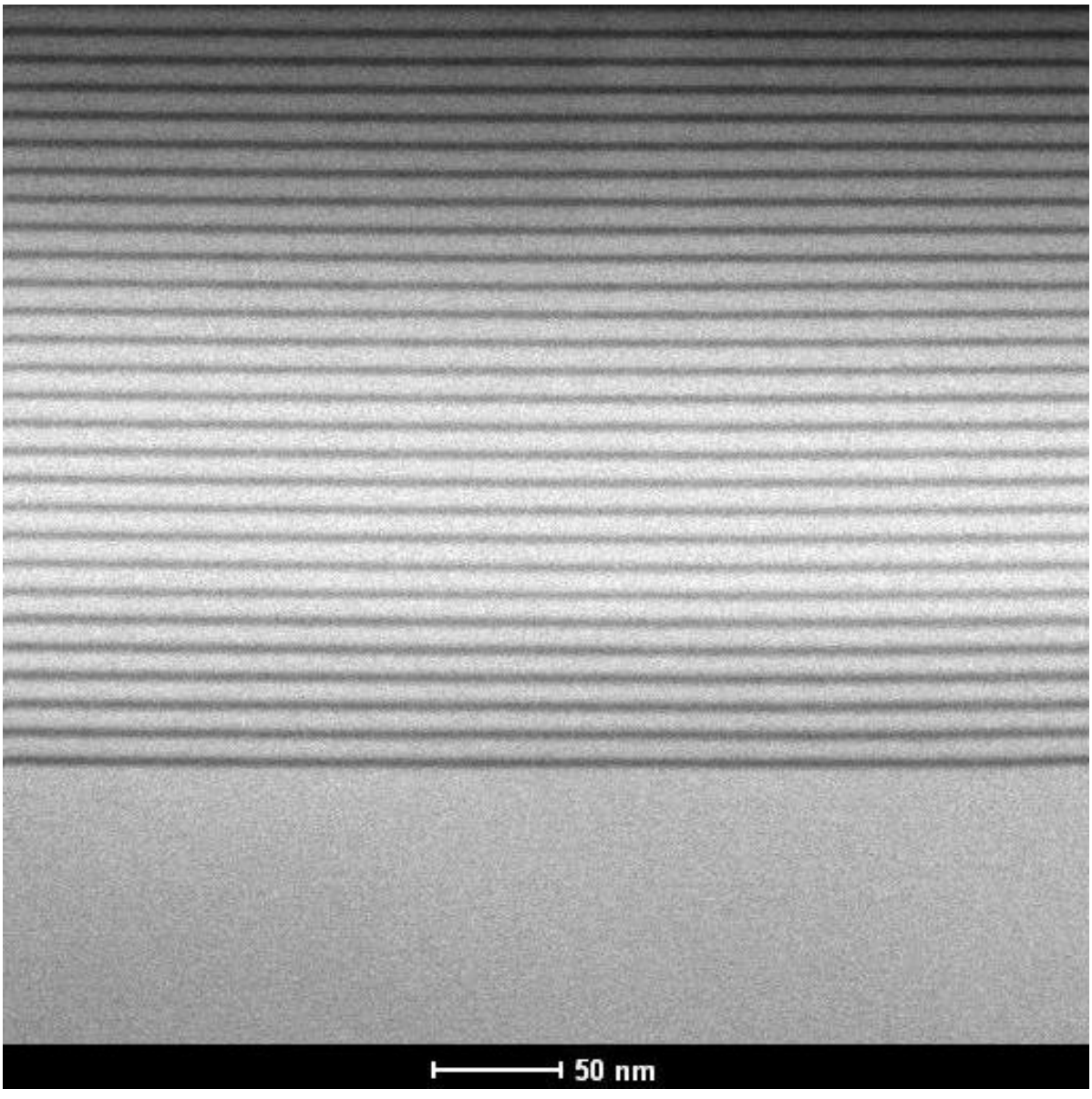

Figure 28 - Image obtained by TEM of sample $S6$ evidencing the superlattice layers of AlN (darker layers) and GaN (brighter layers), as well as the buffer layer of GaN.

The flat interfacial separation between layers of AlN and GaN can be better evidenced by increasing the magnification at a specific position of the superlattice structure, as can be seen in Figure 29 that contains a TEM image acquired using a higher spatial resolution.

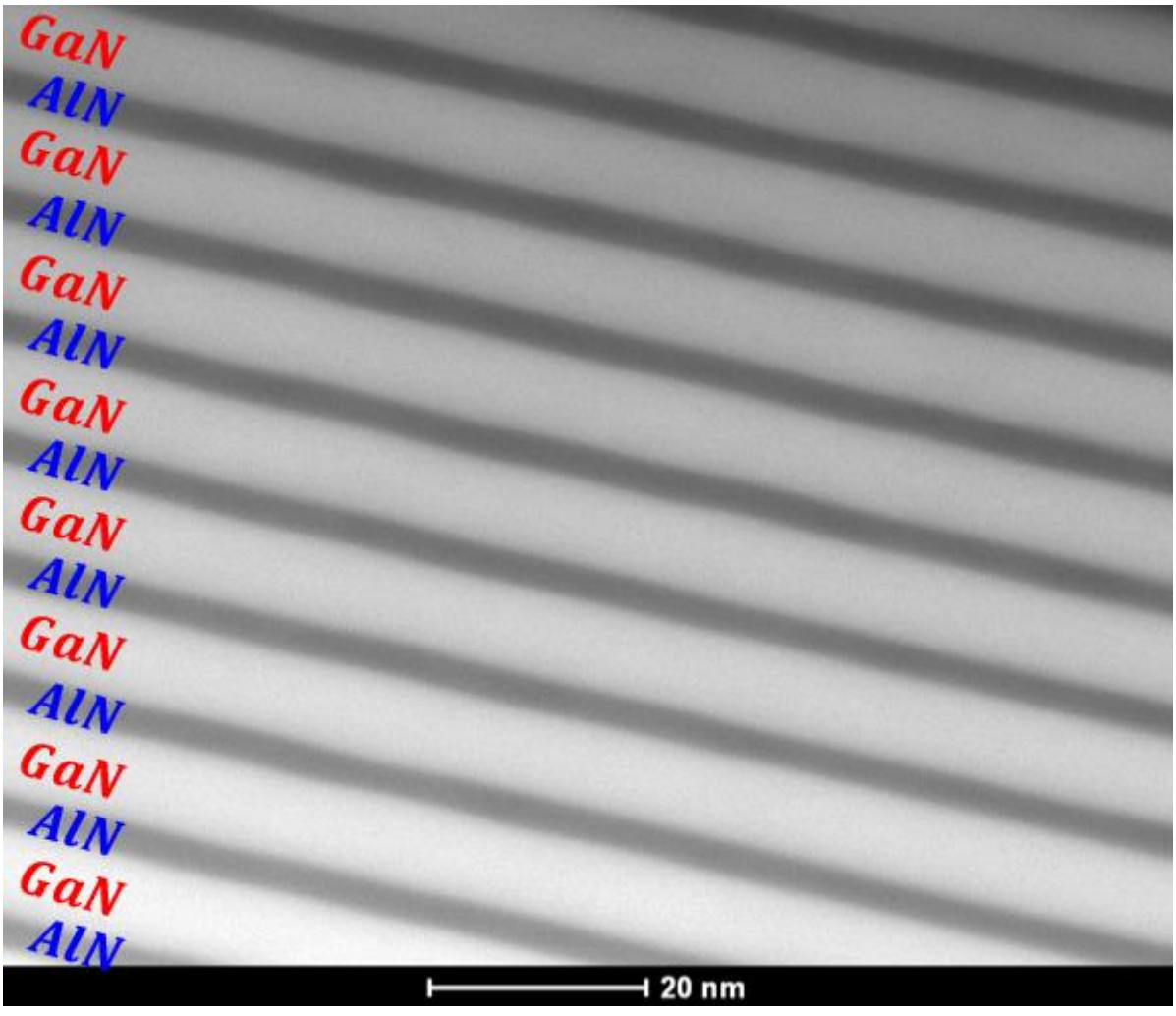

Figure 29 - Image obtained by TEM of sample $S6$ using a higher magnification, exhibiting the superlattice layers of AlN (darker layers) and GaN (brighter layers).

The monolayers that constitute each layer of AlN and GaN can be evidenced by using an even higher order of magnification in the electronic microscope. In Figure 30 it is possible to distinguish nitride monolayers containing atoms of gallium (brighter regions) and atoms of aluminum (darker regions). The internal gradient of contrast visualized within the limits of each layer is associated to the disposition of atoms of nitrogen and the group-three atoms in the tetrahedral configuration, as shown in $Chapter\ 2$.

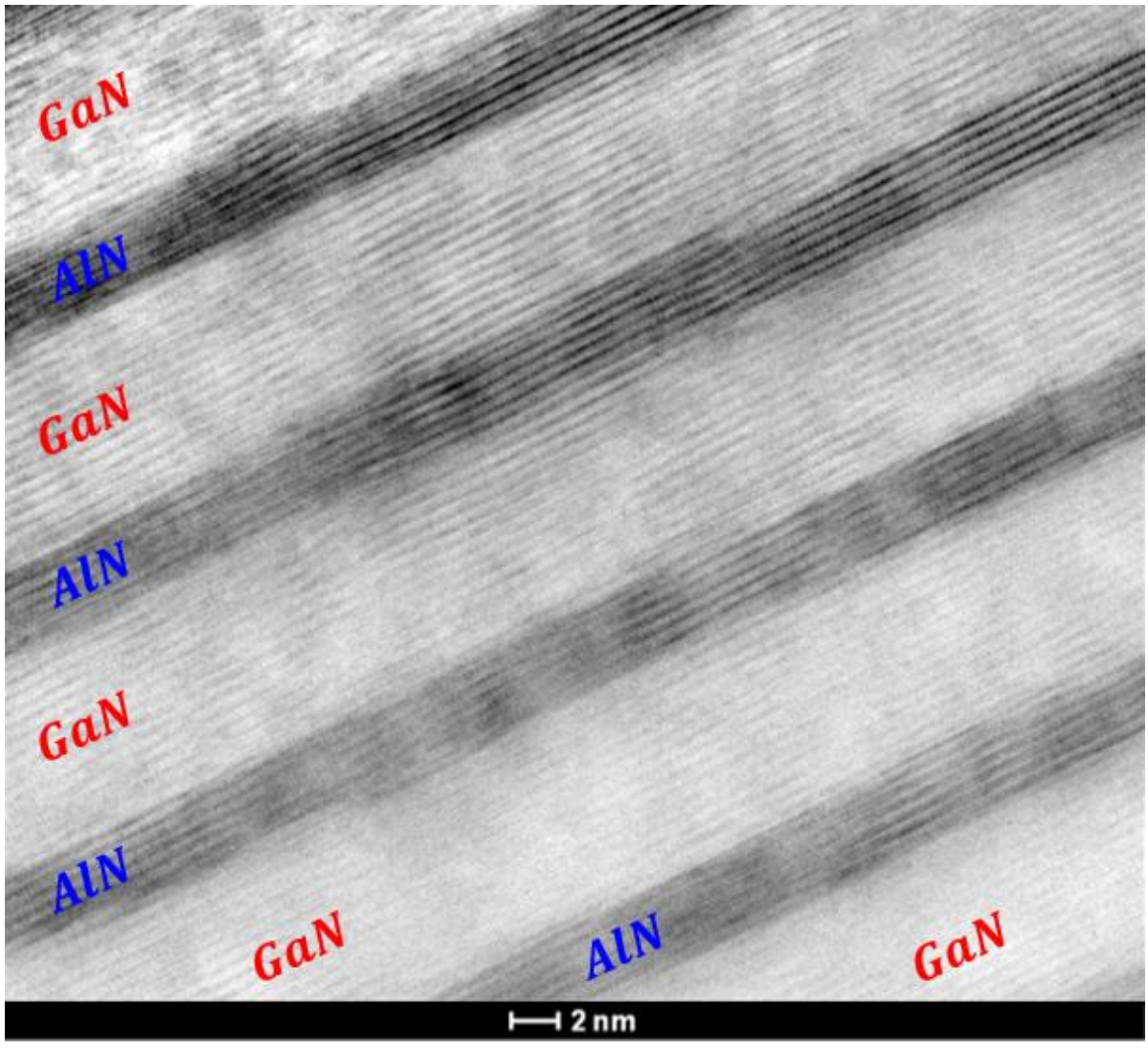

Figure 30 - Image obtained by TEM of sample $S6$ suing higher magnification evidencing the superlattice layers of AlN (darker layers) and GaN (brighter layers).

Overall, no considerable misfit dislocations were evidenced along the analyzed superlattice cross sectional area, and the presence of a gradient of contrast surrounding the interfacial separation between layers in some regions indicates a subtle presence of compositional boundary semilayers promoted by atomic impingement during the periodic epitaxial growth. Using the highest possible resolution in the order of 10^6 of magnification, the approximate value for the thicknesses of the monolayers of AlN and GaN of sample $S6$ along its epitaxial growth direction $[0001]$ were measured using an appropriate software ($Image\ J$, $National\ Institutes\ of\ Health$), as illustrated in Figure 31.

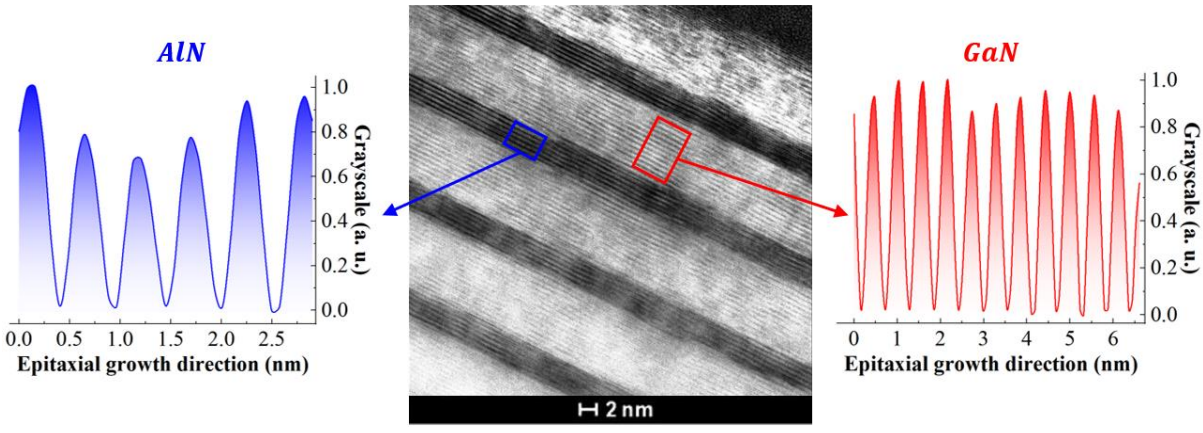

Figure 31 - Monolayers of AlN and GaN along the epitaxial growth direction $[0001]$.

In this figure, each maximum in grayscale represents the limits of each monolayer defined along the epitaxial growth direction $[0001]$. Considering the accuracy of the imaging analysis being determined by the TEM spatial resolution of $0.1\ nm$, the average thicknesses values obtained for the monolayers of AlN ($\sim 0.51\ nm$) and GaN ($\sim 0.56\ nm$) are comparably close to the axial lattice parameters c of the wurtzite crystals AlN ($0.4982\ nm$) and GaN ($0.5186\ nm$), which are usually more precisely determined by using the technique of X-ray diffraction at the sub-Angstrom metric scale.[76] Likewise, the approximate value for the period of the superlattice was determined by evaluating the gradient of contrast across multiple layers of AlN and GaN, as shown in the Figure 32.

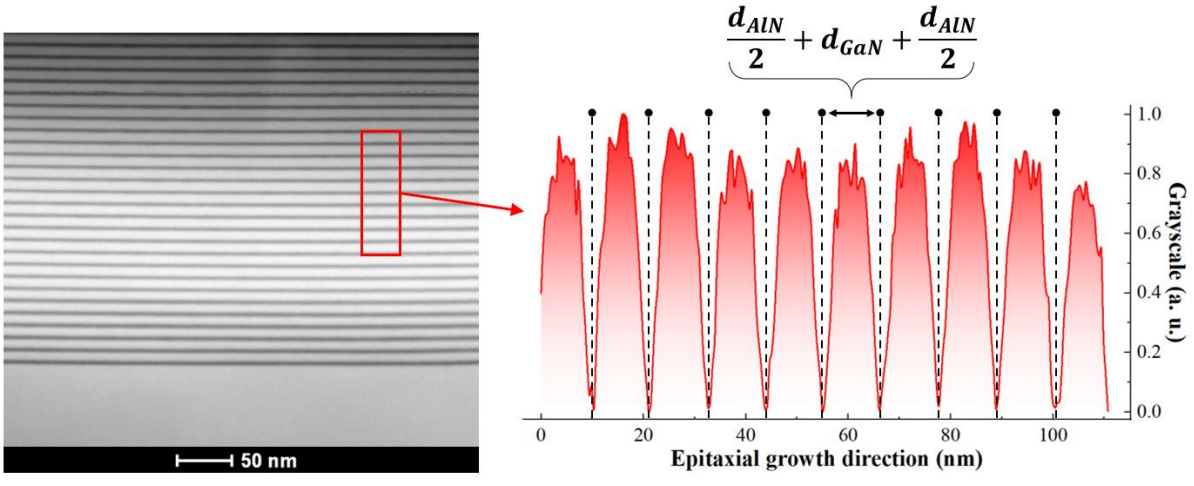

Figure 32 - Determining the period of the superlattice $S6$.

The average period length of $11.2 \pm 0.3\ nm$ was obtained considering the distance between consecutive valleys in the gradient of contrast observed along the epitaxial growth direction $[0001]$. In this figure, the distance between two successive minimums represents the space

comprehended by one full layer of GaN surrounded by half layers of AlN on either side. The imprecision of $\pm 0.3\ nm$ represents the standard deviation between eight consecutive periods. This period length is also comparably close to its nominal value of approximately $10.6\ nm$ determined in situ using $RHEED$ during the superlattice growth.

5.2 Compositional analysis

In order to verify the distribution of atomic content along the AlN and GaN layers observed by TEM, the technique of Energy-Dispersive X-Ray Spectroscopy (EDS) was employed. Figure 33 presents the analyzed region delimited by a linear scanning of approximately $17\ nm$ which crosses two complete layers of AlN and one full layer of GaN.

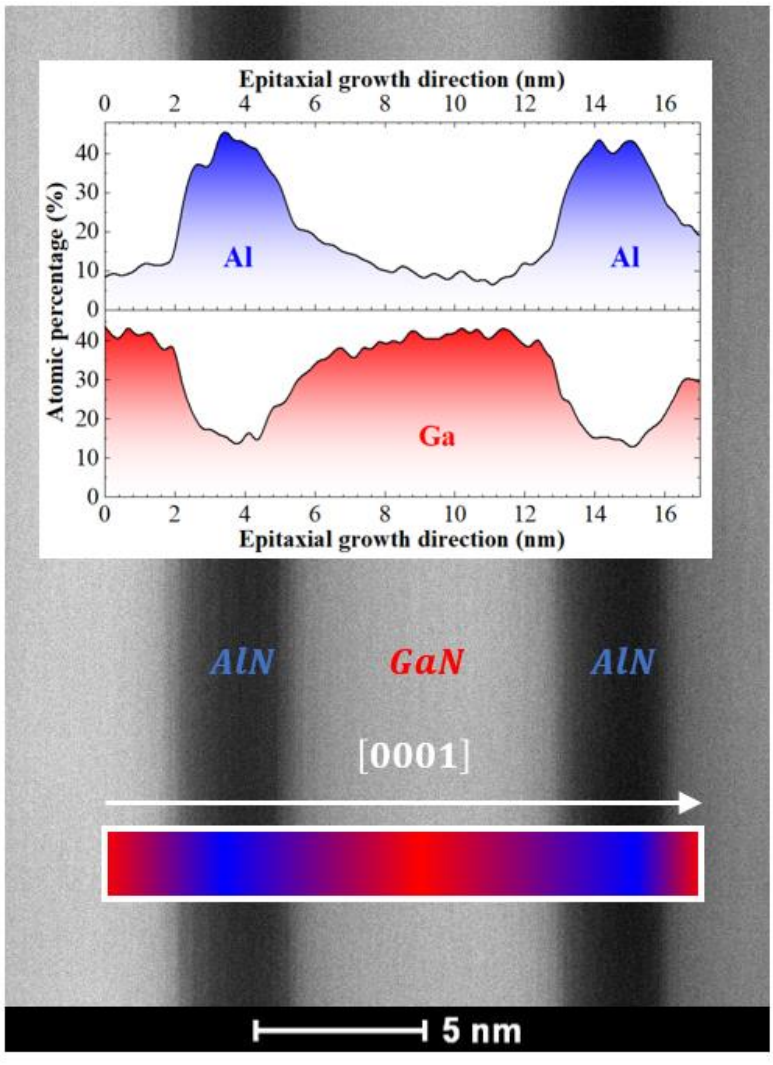

Figure 33 - Atomic percentages determined by EDS.

The average sum of the relative atomic concentration ($52 \pm 3\ \%$) between atoms of Al and Ga shows little deviation from the ideal value of 50%, as expected for a group-III nitride compound.[114] Evidently, the absence of abrupt changes in atomic percentage along the space comprehended by a single monolayer suggests the increment in stoichiometric homogeneity occurring in the direction defined outwards the interfacial surfaces. In comparison to the length of one complete period of the superlattice evidenced using the TEM technique ($\sim 11.2\ nm$), the value obtained by the EDS technique ($\sim 11.0\ nm$) is very close, which was calculated using the distribution of atomic percentage along the direction of epitaxial growth in the analyzed range of linear scanning. Additionally, a more subtle percentual increase in Al atomic bonding than in the case of Ga is also evidenced, which might be associated to the preferred nitrogen bounding in forming AlN due to its more similar atomic radii ($r_N = \sim 56\ pm$, $r_{Al} = \sim 118\ pm$, $r_{Ga} = \sim 136\ pm$) and more intense net electronegativity ($\chi_{AlN} = 1.43$, $\chi_{GaN} = 1.23$), besides MBE growth conditions, such as the time each effusion cell's shutter remains closed, as well as the temperature at the crucibles and at the substrate.[114]

5.3 Structural analysis

In order to determine more precisely the thicknesses of the AlN and GaN layers of all the six superlattices, as well as their lattice parameters and consequently its average strain, the technique of X-ray diffraction XRD was employed right after the growth of each nanostructure. The reciprocal space maps ($XRD - RMS$) of each superlattice were measured across the asymmetric $\bar{1}\bar{1}24$ and $\bar{1}015$ reflections.[190] These data sets were used to determine the values of the lattice parameters of the AlN and GaN layers, perceived by the XRD system as a distribution of values along each analyzed superlattice. Figure 34 presents the XRD data for all the superlattices, as well as the $\bar{1}\bar{1}24$ reciprocal space mapping of superlattice $S6$, which is the one that contains the thickest layers of GaN.

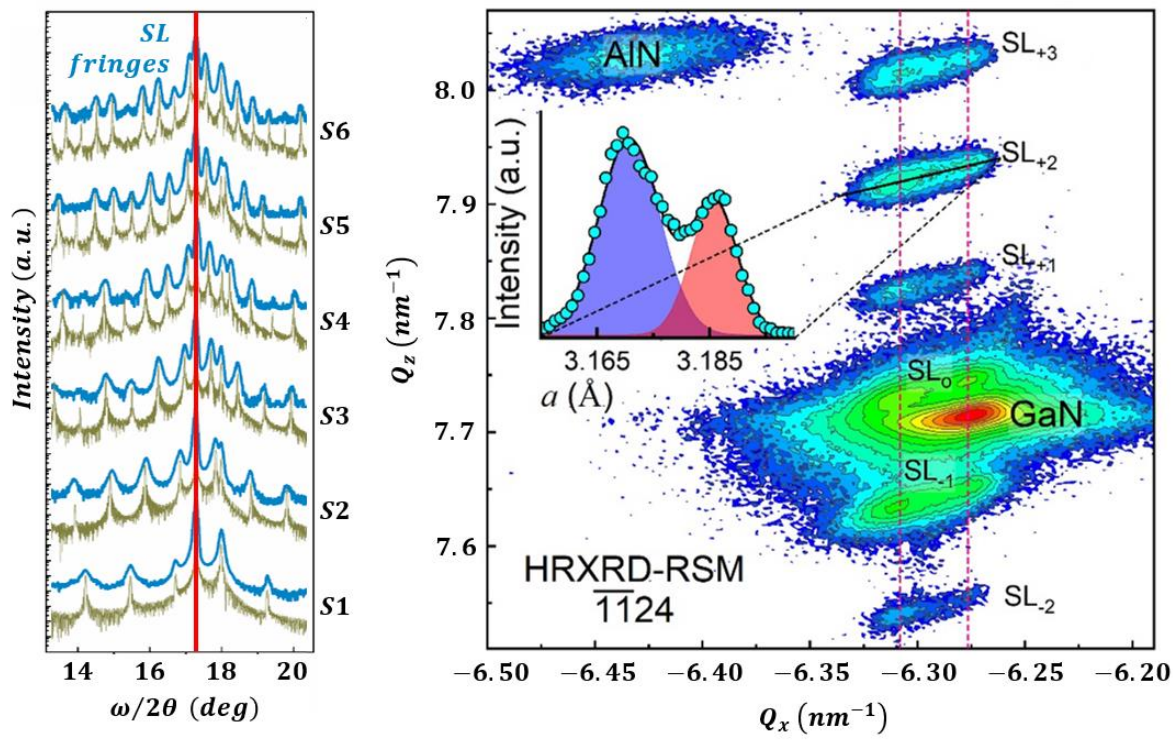

Figure 34 – On the left: Measured and simulated XRD scans for all the superlattices; on the right: RSM acquired using the asymmetric $\bar{1}\bar{1}24$ reflection for the sample $S6$.

In the figure, the GaN substrate is evidenced as the most intense peak, followed by another intense region representing the AlN substrate and finally a set of satellite peaks (SL_n) distributed along the Q_z axis, which are associated to the AlN and GaN layers of the superlattice. The presence of SL satellite peaks is an indicative of the existence of lattice coherence along the periods of the superlattice, which overcomes the natural lattice mismatch between AlN and GaN ($\sim 2.5\%$).[190] The evidence of lattice coherence confirms that the in-plane lattice parameter of the superlattice (a_{SL}) is conserved across layers of AlN and GaN ($a_{SL} = a_{SL}^{GaN} = a_{SL}^{AlN}$).[162] In the reciprocal space mapping, the distribution of each satellite peak along the Q_x axis demonstrates the varying character of the a_{SL} in the superlattice, which in this case is associated to the gradient of strain along the superlattice structure. In special, the vertical dashed lines in the figure define the two distribution centers of the satellite peaks, as shown in this figure's inset, which are attributed to the conditions of regions of the superlattice being fully strained, while others are partially relaxed. Therefore, the in-plane lattice parameter of the AlN and GaN layers (a_{SL}) is defined between the two extremes (a_{SL}^{min} and a_{SL}^{max}), also respecting the boundaries imposed by the bulk values of each unstrained material (a_{bulk}^{AlN} and a_{bulk}^{GaN}). For superlattice $S6$ the range is:

$$a_{bulk}^{AlN} = 3.113\ \text{Å} \leq a_{SL}^{min} = 3.171\ \text{Å} \leq \left(a_{SL}^{GaN}, a_{SL}^{AlN}\right) \leq a_{SL}^{max} = 3.186\ \text{Å} \leq a_{bulk}^{GaN} = 3.189\ \text{Å}$$

The most likely causes for the presence of a gradient of strain along the structure of the superlattice are associated to events of elastic potential energy being released during the growth of the nanostructure, as well as promoted by the cooling period after synthesis.[114,192] In particular, using optical microscopy ($Olympus$, model $BX41$) with a hundred times of magnification, a mosaic of cracks was evidenced in the surface of each superlattice, as can be seen in Figure 35 for superlattice $S6$.

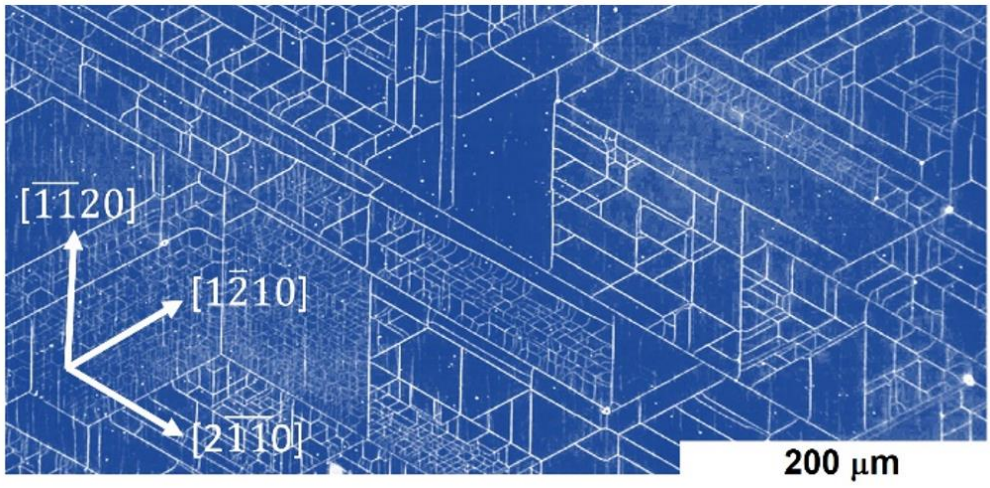

Figure 35 - Hexagonal network of cracks in superlattice $S6$ evidenced using optical microscopy.

As seen in the figure, the network of cracks propagates along the hexagonal directions $[\bar{1}120]$, $[1\bar{2}10]$ and $[2\bar{1}\bar{1}0]$, separated from each other by $\pi/3\ radians$. It is also possible to distinguish different types of cracks, in special: long and intense cracks that delimit areas in the order of hundreds of micrometers between cracking edges; and short and faint cracks, which are most likely originated after the creation of the long cracks and probably during the process of cooling down after synthesis, delimiting dense areas in the order of just a few micrometers. By creating cracks, the superlattice releases its elastic potential energy, which leads to a local condition of relief in strain along the structure of the superlattice.[192,193] At the regions situated far from any cracks, such as at the center of an area delimited by distant cracks, the atomic bonds are still submitted to the full residual in-plane strain, which magnitude is expected to gradually decrease in the vicinity of any crack.[193] Due to the spatial resolution of the XRD technique being limited to an average of the distribution of strain for the whole

structure, only the most intense limit was considered. Table 4 presents the $XRD - RSM$ results for each superlattice:

Table 4 - Values of period (T), layers' thicknesses (d), in-plane strain (ϵ_{xx}) and in-plane lattice constant (a_{SL}) of each superlattice using $XRD - RSM$.

Sample	$T\ (nm)$	d_{GaN}/d_{AlN} (nm)	$\epsilon_{xx}^{GaN_{SL}}$ (×10^{-2})	$\epsilon_{xx}^{AlN_{SL}}$ (×10^{-2})	a_{SL} (Å)
S1	3.65 ± 0.08	$0.26/3.48$	-1.927	0.513	3.128
S2	4.84 ± 0.08	$1.38/3.47$	-1.516	0.888	3.140
S3	6.35 ± 0.04	$2.83/3.52$	-1.241	1.170	3.149
S4	7.95 ± 0.08	$4.61/3.33$	-0.924	1.494	3.159
S5	8.92 ± 0.03	$5.51/3.41$	-0.821	1.601	3.163
S6	10.47 ± 0.6	$7.13/3.34$	-0.616	1.810	3.169

The XRD results evidenced the dependence of the thickness of GaN layers along the superlattice on the in-plane strain. In special, the compressive strain ($\epsilon_{GaN} < 0$) that is felt in the GaN layers and the tensile strain ($\epsilon_{AlN} > 0$) felt in the AlN layers balance each other by maintaining the lattice coherence of the nanostructure.[162] As an example, the thinnest superlattice $S1$ has the most intense tensile strain in the AlN layers ($\epsilon_{AlN} \approx 1.81 \times 10^{-2}$) and the least intense compressive strain in the GaN layers ($\epsilon_{GaN} \approx -0.62 \times 10^{-2}$) among all the superlattices. Likewise, the thickest superlattice $S6$ presents the opposite situation, displaying the least intense tensile strain in the AlN layers ($\epsilon_{AlN} \approx 0.51 \times 10^{-2}$) and the most intense compressive strain in the GaN layers ($\epsilon_{GaN} \approx -1.93 \times 10^{-2}$), among all the superlattices. Figure 36 presents the dependence between in-plane strain and the thickness of the GaN layers.

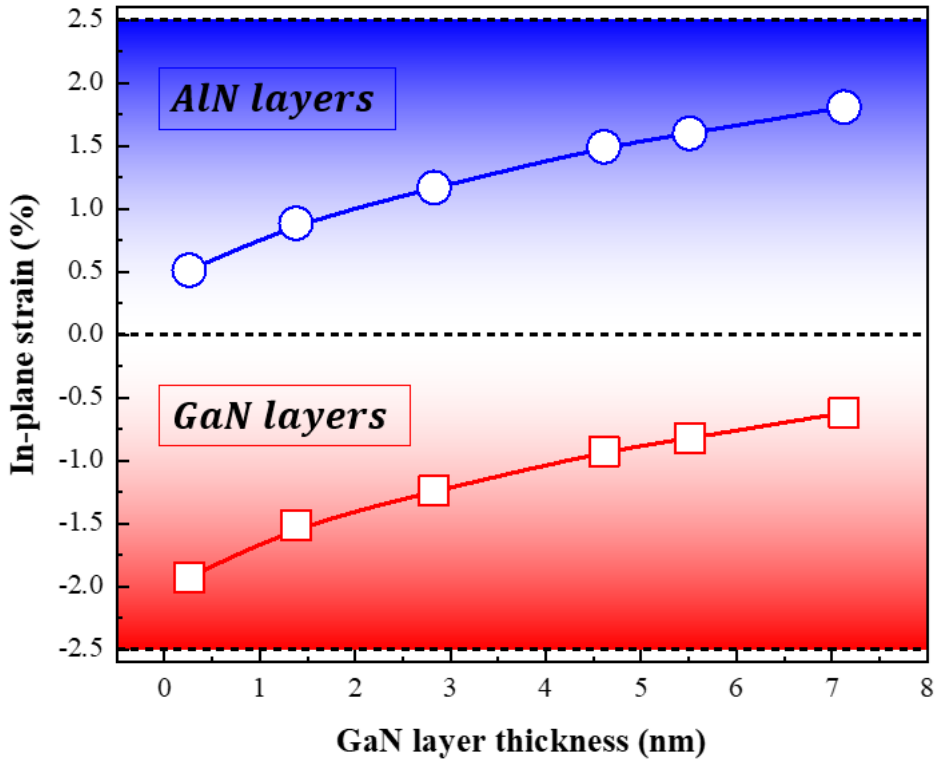

Figure 36 - Dependence between in-plane strain and thickness of the GaN layers of each superlattice.

In the figure, the strain limits ($\epsilon \approx \pm 2.5\% / \epsilon \approx 0\%$) are associated to the cases of fully strained/relaxed layers due to the natural lattice mismatching between AlN and GaN.[190]

5.4 Vibrational analysis

The XRD results showed that, as verified for all the superlattices, even by self-promoting structural defects along the nanostructure in the attempt to release the elastic potential energy stored during growth, none of the superlattices reach the status of being fully relaxed. In particular, the final residual in-plane strain felt after the propagation of cracks is defined not only by the presence of structural defects, but also by the conditions of synthesis, by demonstrating a steady trend with GaN thickness towards the limits of being fully strained/relaxed. Considering the elastic energy minimization in the absence of structural defects as defined in $Chapter\ 3$, an approximate value for the expected resulting in-plane lattice constant in the AlN and GaN layers can be expressed by $a_{SL} = a_0^{AlN,GaN}\left(1 + \epsilon_{xx}^{AlN,GaN}\right) = \frac{a_0^{AlN}\kappa_{AlN} + a_0^{GaN}\kappa_{GaN}}{\kappa_{AlN} + \kappa_{GaN}}$, where the parameter

$\kappa_{AlN,GaN} = d_{AlN,GaN}(C_{11} + C_{12} - 2C_{13}^2/C_{33})_{AlN,GaN}\left(a_0^{AlN,GaN}\right)^{-2}$ strongly depends on the elastic constants C_{ij} of the stiffness tensor of AlN and GaN.[197] This approximation does not take into account the substrate used for epitaxial growth, as well as the effects promoted by the presence of a buffer layer, once it considers only the alternated layers along the periods of the superlattice. In addition to the imprecision in the determination of elastic constants and the occurrence of structural defects, these facts might lead to a discrepancy between expected and measured values of in-plane lattice parameters, as can be seen in Figure 37, which presents a comparison between the actual values of strain obtained from the reciprocal space mapping using XRD and the expected dependence to layers' thicknesses in the absence of structural defects, represented between the extremes delimited by the unstrained values of lattice parameters of bulk AlN ($a_0^{AlN} = 3.113$ Å) and bulk GaN ($a_0^{GaN} = 3.189$ Å).[197]

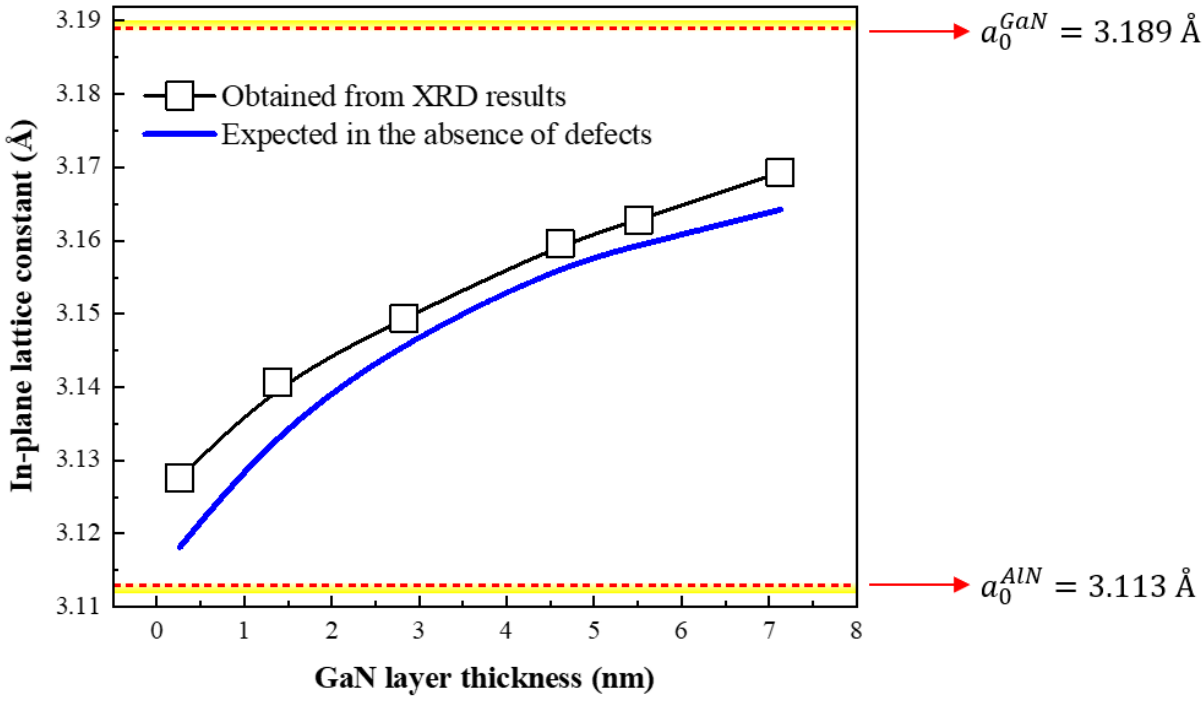

Figure 37 - Comparison between values of strain obtained from XRD and calculated in the absence of structural defects.

Despite displaying an average deviation in the order of ~0.01 Å while based only on the information about the layers' thicknesses, the determination of the in-plane lattice parameter must consider the effects promoted by distribution of defects along the layers of the superlattice. In this scenery, the technique of micro-Raman represents a useful and practical tool for quantifying local strain at the micrometric scale. To do so, initially the Raman modes of substrates of sapphire, AlN and GaN were analyzed in order to verify the contribution of

each component of the superlattices. It was expected that, just like in the XRD analysis, the layers of the GaN template and buffer also produced considerable intensities of Raman scattering when acquiring the data.

Figure 38 presents the Raman spectra of sapphire, AlN and GaN substrates, indicating the spectral position of each evidenced vibrational mode. All the Raman data were measured using the same conditions, as described in $Chapter$ 4.

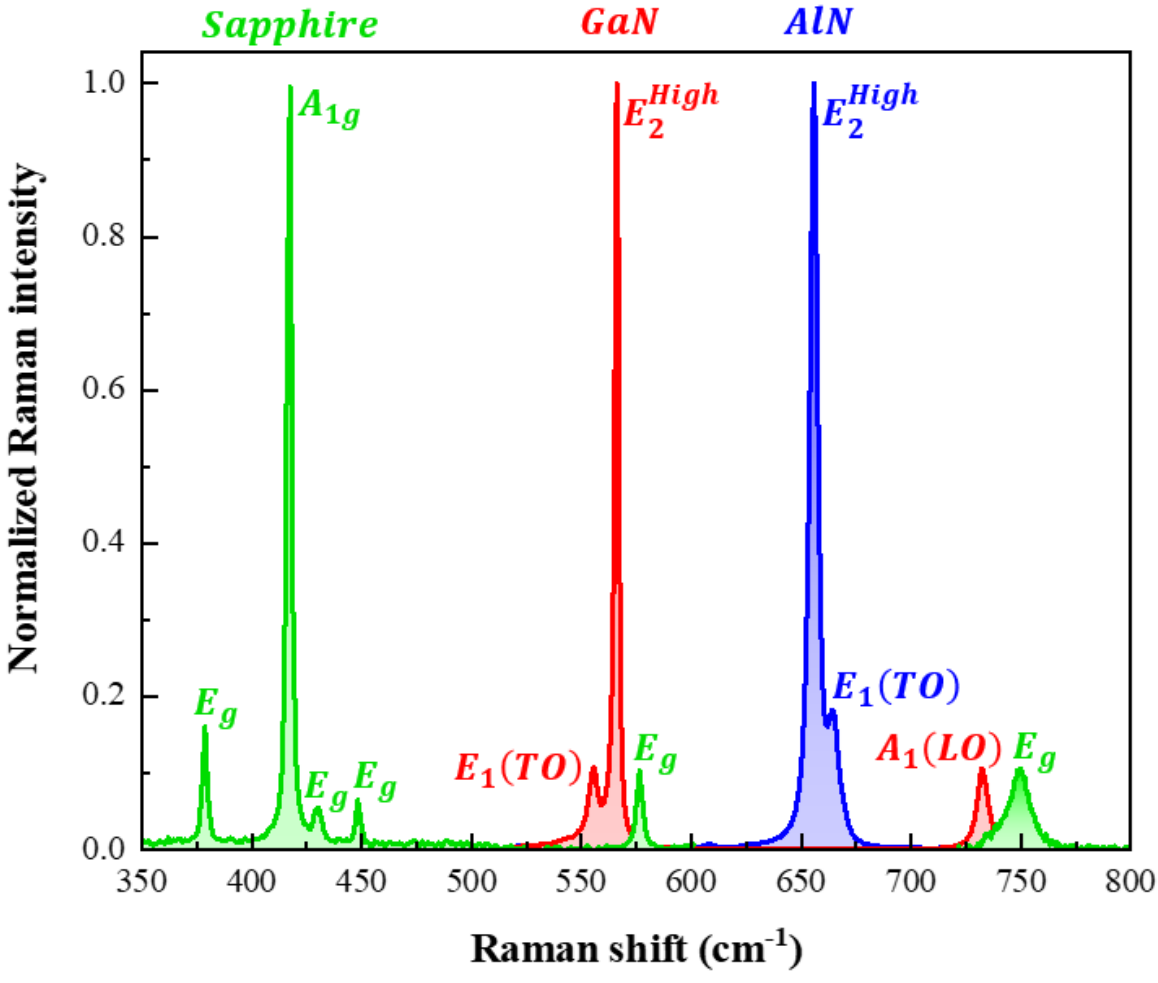

Figure 38 - Raman spectra of sapphire, AlN and GaN substrates in the investigated spectral range.

In this figure the intensity of each Raman spectrum was normalized between zero and one in order to present a comparable range of intensities between materials, once the actual sequence of unnormalized Raman intensities follows the hierarchy: $I_{GaN} > I_{AlN} \gg I_{Sapphire}$. Additionally, by using logarithmic scale it is possible to evidence the polar mode $A_1(TO)$ of AlN vibrationally located between the nonpolar modes E_2^{High} of AlN and GaN.[64] The modes

originated solely from the periods of the superlattices are expected to display a shift in wavenumbers according to the level of strain at which the specific material is being submitted to. Therefore, as discussed in $Chapter\ 3$, due to the lattice coherence the layers of GaN suffer a contraction, whilst consequently the layers of AlN are expanded, leading to opposite situations of compressive and tensile strain, respectively.[64] Also, due to the comparatively small amount of material along the periods of the superlattice, in relation to the template, the presence of shifted modes is likely to be noticed exhibiting weaker intensities than their corresponding layer of template. In the case of sapphire, which belongs to the space group D_{3d} , seven Raman active vibrational modes associated to the irreducible representations A_{1g} and E_g are expected in the spectral range between $300\ cm^{-1}$ and $800\ cm^{-1}$, they are: $380\ cm^{-1}\ (E_g)$, $418\ cm^{-1}\ (A_{1g})$, $431\ cm^{-1}\ (E_g)$, $450\ cm^{-1}\ (E_g)$, $577\ cm^{-1}\ (E_g)$, $645\ cm^{-1}\ (A_{1g})$ and $750\ cm^{-1}\ (E_g)$.[198] The subscript g comes from the German word *gerade*, meaning "even", and it is used in the Mulliken symbol to make explicit the existence of inversion symmetry.[80] In the case of AlN, as member of the group C_{6v} the six first-order Raman active modes in the range between $200\ cm^{-1}$ and $1000\ cm^{-1}$ are: $252\ cm^{-1}\ (E_2^{Low})$, $614\ cm^{-1}\ (A_1(TO))$, $657.7\ cm^{-1}\ (E_2^{High})$, $662\ cm^{-1}\ (E_1(TO))$, $893\ cm^{-1}\ (A_1(LO))$ and $916\ cm^{-1}\ (E_1(LO))$.[64] For GaN, as also member of the group C_{6v}, the six first-order Raman active modes in the range between $100\ cm^{-1}$ and $800\ cm^{-1}$ are: $144\ cm^{-1}\ (E_2^{Low})$, $532\ cm^{-1}\ (A_1(TO))$, $561\ cm^{-1}\ (E_1(TO))$, $567.4\ cm^{-1}\ (E_2^{High})$, $735\ cm^{-1}\ (A_1(LO))$ and $743\ cm^{-1}\ (E_1(LO))$.[64]

As a visualization of the Lyddane-Sachs-Teller relation described in $Chapter\ 2$ for the frequency splitting of polar modes associated to the irreducible representations A_1 and E_1 for AlN and GaN, Figure 39 illustrates the ratio between dielectric constants $\varepsilon_{GaN}/\varepsilon_{AlN}$ for each component defined in-plane ($\varepsilon_{xx}(\omega) = \varepsilon_\infty\left(\omega_{E_1(LO)}^2 - \omega^2\right)/\left(\omega_{E_1(TO)}^2 - \omega^2\right)$) and along the direction of epitaxial growth ($\varepsilon_{zz}(\omega) = \varepsilon_\infty\left(\omega_{A_1(LO)}^2 - \omega^2\right)/\left(\omega_{A_1(TO)}^2 - \omega^2\right)$).[116]

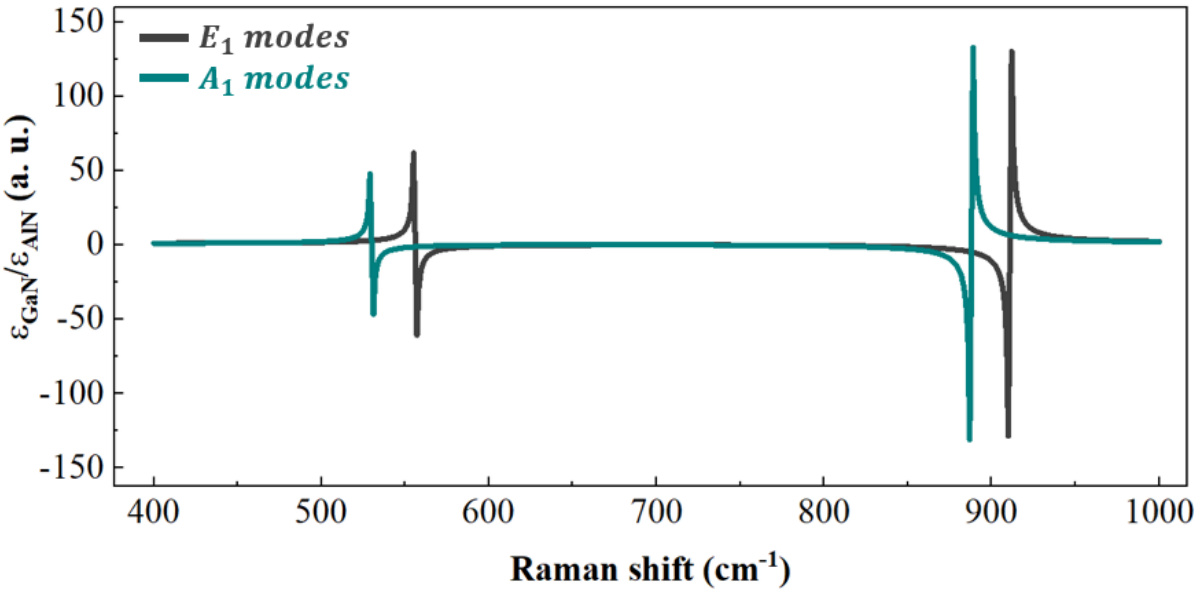

Figure 39 - Ratio between dielectric constants of AlN and GaN using the Lyddane-Sachs-Teller relation for the frequency splitting of modes A_1 and E_1.

In this figure the vertical asymptotes do not reach higher values tending to infinity due to the limit imposed by the finite step in frequency when acquiring the Raman data. According to the Dielectric Continuum Model (DCM) described in $Chapter\ 3$, and specially for materials that display piezoelectricity, the propagation of electromagnetic waves in multilayered systems is dependent on its electric and mechanical properties. For AlN and GaN, as members of the group C_{6v}, the irreducible representations A_1 and E_1 represent polar modes of dipole oscillation with defined directions of polarization. The frequency splitting of these modes in transverse (TO) and longitudinal (LO) optical phonons, as formulated by the Lyddane-Sachs-Teller relation, is associated to the dielectric constants of adjacent media according to the phonon frequency and relative alignment between orientation of polarization and direction of phonon propagation. In particular, the Lyddane-Sachs-Teller relation implies on specific limits for the components of the effective dielectric constant defined on their epitaxial ($\bar{\varepsilon}_{zz} = \varepsilon_{AlN}\varepsilon_{GaN}(d_{AlN} + d_{GaN})(d_{AlN}\varepsilon_{AlN} + d_{GaN}\varepsilon_{GaN})^{-1}$) and in-plane ($\bar{\varepsilon}_{xx} = (d_{AlN}\varepsilon_{AlN} + d_{GaN}\varepsilon_{GaN})(d_{AlN} + d_{GaN})^{-1}$) directions depending on which polar mode is being considered: $\bar{\varepsilon}_{zz} \to 0$ for $A_1(LO)$, $\bar{\varepsilon}_{zz} \to \infty$ for $A_1(TO)$, $\bar{\varepsilon}_{xx} \to 0$ for $E_1(LO)$ and $\bar{\varepsilon}_{xx} \to \infty$ for $E_1(TO)$.[183] Additionally, the sign inversion of the effective dielectric constant occurs at the specific frequencies associated to the polar modes of the materials. This change in sign can be evidenced by zeros and discontinuities of the ratio between dielectric constants $\varepsilon_{GaN}/\varepsilon_{AlN}$ for each irreducible representation.[183] In particular, Figure 40 evidences each Raman active polar

mode of AlN and GaN by tracking the value of the in-plane (ε_{xx}) and epitaxial (ε_{zz}) ratios $\varepsilon_{GaN}/\varepsilon_{AlN}$, associated to the irreducible representations E_1 and A_1, respectively. This figure is zoomed in the range around proximity to zero in order to highlight frequency position of each polar mode of AlN and GaN. The discontinuities promoted by limits that tend to infinity are seen as straight vertical lines for each mode and each material.

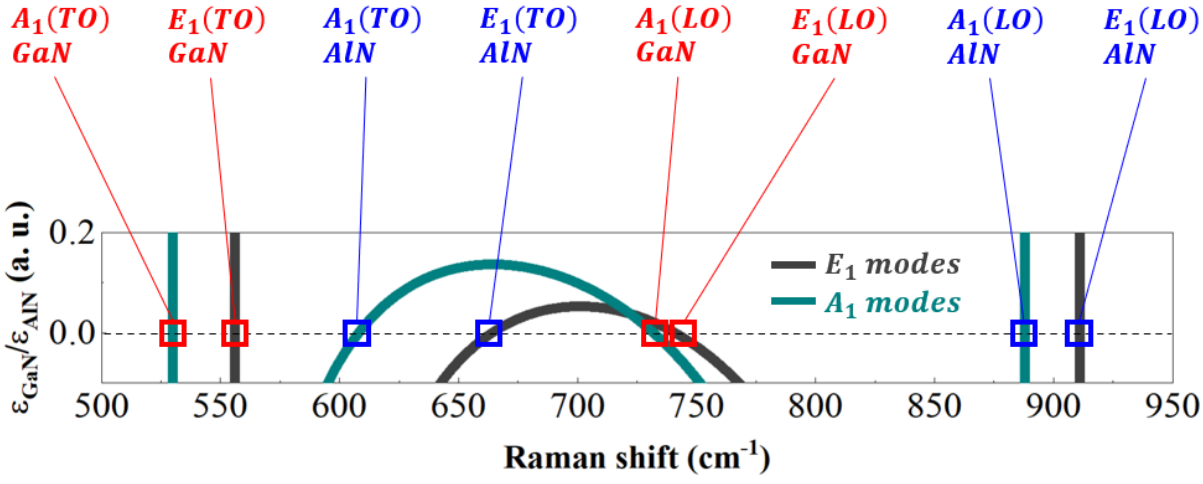

Figure 40 - Ratio between dielectric constants of AlN and GaN evidencing each polar mode.

Using the Lyddane-Sachs-Teller relation with $\varepsilon_{\infty}^{AlN} \approx 4.84$ and $\varepsilon_{\infty}^{GaN} \approx 5.35$, the dielectric constants calculated for AlN ($\varepsilon_{xx} = 9.1$ and $\varepsilon_{zz} = 10.3$) and GaN ($\varepsilon_{xx} = 9.6$ and $\varepsilon_{zz} = 10.2$) are very close to values reported for these wurtzite crystals.[183] Figure 41 presents the Raman spectra of AlN and GaN substrates in logarithmic scale to highlight low intensity modes, also illustrating their correlation to the ratio between frequency dependent dielectric constants of AlN and GaN.

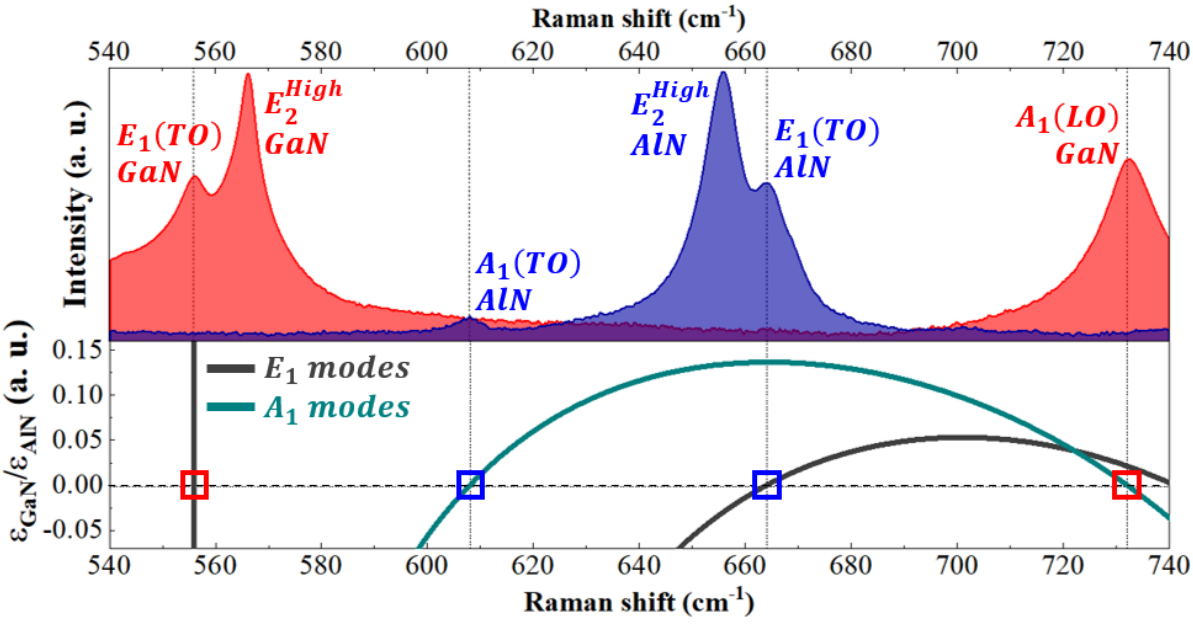

Figure 41 - Polar modes of AlN and GaN and the ratio between their frequency dependent dielectric constants.

The generalized Hooke's law, described in $Chapter\ 2$ and used for acquiring information on strain using Raman shift, is fundamentally dependent on the relevant components of the elastic constant defined by the stiffness and compliance tensors of a material. For AlN/GaN superlattices in the absence of epitaxial stress, the successful determination of precise values of in-plane strain is dependent on two relevant elastic constants (C_{13} and C_{33}) and two elements of deformation potential (a and b) according to the relation $\Delta\omega_{E_2^{High}} = R_{E_2^{High}}\epsilon_{xx}$, where $R_{E_2^{High}} = 2\left(a_{E_2^{High}} - \frac{b_{E_2^{High}}C_{13}}{C_{33}}\right)$ represents the elastic dependency on the variation of Raman shift ($\Delta\omega_{E_2^{High}} = \omega_{E_2^{High}}^{strained} - \omega_{E_2^{High}}^{bulk}$), in this case for the nonpolar mode E_2^{High}. Despite an expressive amount of theoretical and experimental investigations have been devoted in obtaining accurate values for these four quantities in the last decades, there is still a considerable deviation between reported values. As an example, Table 5 presents some of the bulk values of $a_{E_2^H}^{AlN,GaN}$, $b_{E_2^H}^{AlN,GaN}$, $C_{13}^{AlN,GaN}$ and $C_{33}^{AlN,GaN}$ that can be found in the literature for unstrained AlN and GaN, as well as the resulting average ratio $R_{E_2^{High}}$.

Table 5 - Bulk deformation potentials and elastic constants of AlN and GaN from references.

Material	***Constant***	***Value from reference***	***Average***	$R_{average}\ (cm^{-1})$
GaN	$a_{E_2^H}^{GaN}\ (\mathrm{cm}^{-1})$	-850,[26,102,199] -818,[64] -793,[64] -742,[112] -740[106]	-806 ± 49	-1232 ± 205
	$b_{E_2^H}^{GaN}\ (\mathrm{cm}^{-1})$	-821,[64] -797,[64] -727,[106] -715[112]	-765 ± 52	
	$C_{13}^{GaN}(GPa)$	-114,[50,200] -110,[57,201] -106,[26,51] -104,[112,202] -103,[52,57] -100,[53] -98,[203] -96,[76,204] -80.4,[204] -68,[57] -64[30,205]	-97 ± 17	
	$C_{33}^{GaN}(GPa)$	-414,[112] -405,[52,57] -398,[26,51] -392,[53] -390,[57,201] -389,[203] -387,[204] -381,[200] -376,[202] -354[57]	-391 ± 15	
AlN	$a_{E_2^H}^{AlN}\ (\mathrm{cm}^{-1})$	-1083,[105] -1048,[105] -1038,[105] -1008,[105] -877,[30]	-1011 ± 79	-1472 ± 253
	$b_{E_2^H}^{AlN}\ (\mathrm{cm}^{-1})$	-969,[206] -940,[110] -911[106]	-940 ± 29	
	$C_{13}^{AlN}(GPa)$	-140,[76] -127,[53,207] -120,[51,85,208] -116,[209] -113,[112] -112,[202] -108,[52,57] -100[57,201] -99,[86,210] -94[57]	-113 ± 13	
	$C_{33}^{AlN}(GPa)$	-409,[209] -395,[51,85,208] -392,[76] -390,[57,201] -389,[86,210] -383,[202] -382,[53,207] -377,[57] -373[52,57] -370[112]	-386 ± 10	

As seen in the table, the diverse spectrum of values reported for the constants leads to an average uncertainty of approximately $17\ \%$ in the determination of the vibrational/mechanical ratio $R_{E_2^{High}}$ for both AlN $(-1472 \pm 253\ cm^{-1})$ and GaN $(-1232 \pm 205\ cm^{-1})$. Consequently, it aggravates the imprecision of spectroscopically accessing information regarding mechanical features of these materials. Therefore, considering the high resolution at the microscale provided by the micro-Raman technique in acquiring vibrational data, an alternative method of strain analysis with a more precise formulation can be developed. In this research, the phenomenon of lattice coherence, described in $Chapter\ 3$ and confirmed by XRD results for all the AlN/GaN superlattices, was considered as starting point for a correlation model between the strained condition of a material and its evidenced Raman shift. From the definition of strain in the generalized Hooke's law, the in-plane lattice constant can be expressed as a function of the strained condition felt by the material as $a_{strained} = a_{unstrained}(1 + \epsilon_{xx})$. Whether or not structural defects are present, this expression is still held valid along all the superlattice once the balance between the strained/relaxed conditions at which the interfacing materials are being submitted to are regulated and maintained by the nanostructural coherency.[162] In terms of the observed Raman shift associated to the nonpolar mode E_2^{High}, the in-plane lattice constant a_{SL} of each superlattice can be then represented using the vibrational/mechanical ratio $R_{E_2^{High}}$ by:

$$a_{SL} = a^i_{unstrained}\left(1 + \frac{\Delta\omega^i_{E_2^{High}}}{R^i_{E_2^{High}}}\right), \qquad i = \{AlN, GaN\}$$

As shown in Figure 42, the inaccuracy when determining the in-plane lattice constant tends to increase in more intense conditions of strain, which are perceived in Raman scattering as large shifts parting from the unstrained vibrational mode. This imprecision is promoted by the uncertainty in the ratio $R_{E_2^{High}}$, which characterizes the standard linear method of interpretation of Raman scattering ($\omega_{strained} = \omega_0 + R\epsilon_{xx}$).

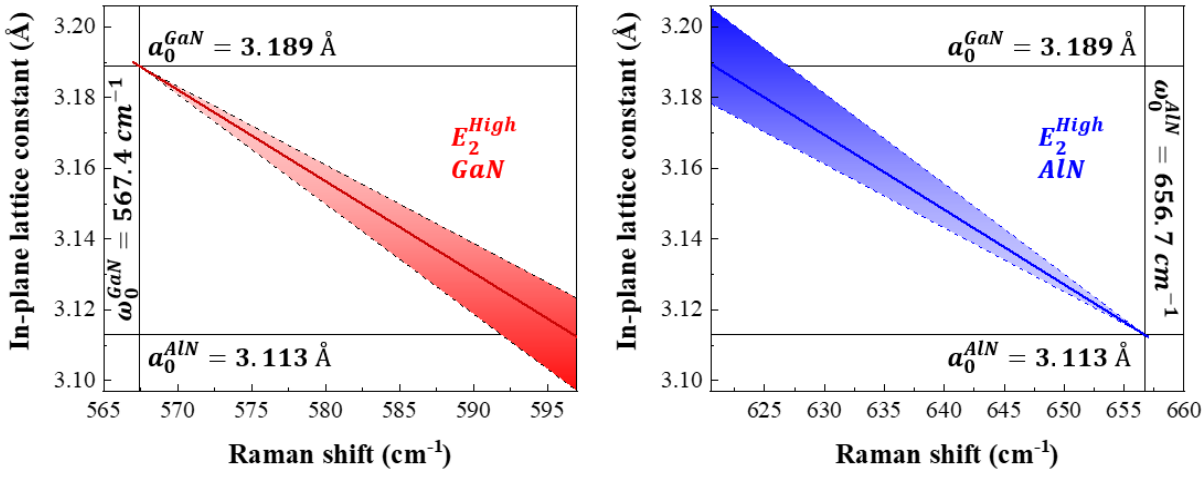

Figure 42 - Imprecision in determining the in-plane lattice constant of AlN/GaN superlattices using the standard linear method of interpretation of Raman scattering.

Contemplating the vibrating atomic system in the scope of harmonic oscillations, as discussed in $Chapter\ 2$, the resulting vibrational frequency ($\omega = \sqrt{k/m}$) has its explicit dependence on the atomic bond strength represented by the force constant k of the oscillating atomic configuration. For a system with constant mass, deviations in frequency can be assumed as controlled by modifications on the force constant, which is inversely proportional to the distance between charge centers ($k \propto 1/|\vec{x}| \therefore \Delta k/\Delta|\vec{x}| \propto -1/|\vec{x}|^2$).[26] At the interatomic distance scale, the changes on the force constant can be directly associated to the level of strain ($\epsilon \equiv \Delta a/a$) felt by the oscillating atomic system ($k \propto 1/a \therefore \Delta k/\Delta a \propto -1/a^2 \therefore \Delta k \propto -\Delta a/a^2 = -\epsilon/a$). As explicitly dependent on the in-plane strained condition, the force constant can then be defined by the sum between its unstrained value (k_0) and a deformation element ($\Delta k = -K\epsilon_{xx}k_0$, once $k_0 \propto 1/a_0$). The vibrational frequency ($\omega = \sqrt{k/m} = \sqrt{(k_0 + \Delta k)/m}$) can then be defined as dependent on strain by:

$$\omega = \sqrt{k/m} \propto \sqrt{\frac{1}{m}(k_0 - K\epsilon_{xx}k_0)} = \sqrt{\frac{k_0}{m}(1 - K\epsilon_{xx})} \therefore \omega = \omega_0\sqrt{(1 - K\epsilon_{xx})}$$

Here, alongside with the unstrained mode ω_0, the material-dependent proportionality constant K determines the effect of strain on the Raman shift ($\Delta\omega$), which can be expressed by:

$$\Delta\omega = \omega - \omega_0 = \omega_0\sqrt{(1 - K\epsilon_{xx})} - \omega_0 \therefore \Delta\omega = \omega_0\left(\sqrt{(1 - K\epsilon_{xx})} - 1\right)$$

Therefore, for AlN and GaN layers in AlN/GaN superlattices, the Raman shift of the nonpolar mode E_2^{High} can be defined by:

$$\Delta\omega^i = \omega_0^i \left(\sqrt{\left(1 - K_i \epsilon_{xx}^i\right)} - 1 \right), \qquad i = \{AlN, GaN\}$$

This nonlinear approximation represents an alternative tool to the standard linear method of description of Raman shift based on strain. In fact, by expanding this relation in binominal series ($(1+x)^n = \sum_{j=0}^{n} \binom{n}{j} x^j$) it is possible to correlate both linear and nonlinear approaches:[24]

$$\begin{aligned}
\Delta\omega^i &= \omega_0^i \left(\sqrt{\left(1 - K_i \epsilon_{xx}^i\right)} - 1 \right) \\
&= \omega_0^i \left(\left(1 + \frac{1}{2}\left(-K_i \epsilon_{xx}^i\right) - \frac{1}{8}\left(-K_i \epsilon_{xx}^i\right)^2 + \frac{1}{16}\left(-K_i \epsilon_{xx}^i\right)^3 + \cdots \right) - 1 \right) \\
&= \omega_0^i \left(1 - 1 - \frac{1}{2}\left(K_i \epsilon_{xx}^i\right) - \frac{1}{8}\left(K_i \epsilon_{xx}^i\right)^2 - \frac{1}{16}\left(K_i \epsilon_{xx}^i\right)^3 + \cdots \right) \\
&= \frac{1}{2}\omega_0^i K_i \epsilon_{xx}^i \left(-1 - \frac{1}{4}\left(K_i \epsilon_{xx}^i\right)^1 - \frac{1}{8}\left(K_i \epsilon_{xx}^i\right)^2 + \cdots \right)
\end{aligned}$$

Therefore, using the definition of Raman shift according to the standard linear method ($\Delta\omega^i = R_i \epsilon_{xx}^i$) and taking the binomial approximation only to the first order of strain (once $\epsilon_{xx}^i \gg \left(\epsilon_{xx}^i\right)^n \; \forall\, n \in \mathbb{N} \wedge n > 1$), the proportionality constant can be estimated by:

$$\Delta\omega^i = R_i \epsilon_{xx}^i = -\frac{1}{2}\omega_0^i K_i \epsilon_{xx}^i \left(1 + \frac{1}{4} K_i \epsilon_{xx}^i + \frac{1}{8}\left(K_i \epsilon_{xx}^i\right)^2 + \cdots \right) \approx -\frac{1}{2}\omega_0^i K_i \epsilon_{xx}^i \; \therefore \; K_i \approx -\frac{2R_i}{\omega_0^i}$$

This way, using the average quantities reported in literature, the correspondent values for the proportionality constant K of AlN and GaN in the harmonic approximation are:

$$K_{literature}^{AlN} \approx 4.5 \pm 0.8, \qquad K_{literature}^{GaN} \approx 4.3 \pm 0.7$$

In order to verify the validity of these values, the technique of micro-Raman was employed in the investigation of AlN and GaN Raman modes of each superlattice. To do so, the methodology of spatial sampling was used, by acquiring the Raman data in five different positions of each superlattice such that the distance between analyzed locations was maintained greater than fifty micrometers, using the optimal spatial resolution ($\sim 1\ \mu m$). The positions were randomly chosen along the superlattice by using an optical microscope ($Olympus$, model $MPLanN100x$) and a digital camera ($uEye$), with one hundred times of magnification. In

order to avoid effects of gradient of strain between cracks, all the positions were selected exactly on top of cracks so that the acquired Raman shift represented the strained condition after the maximum amount of elastic energy had been released by each superlattice.[46] All the Raman data were measured using the same conditions, as described in $Chapter\ 4$, prioritizing the visualization of the nonpolar mode E_2^{High}. Figure 43 presents an image of optical microscopy acquired in a determined position of superlattice $S6$, indicating one specific position of Raman analysis on top of a line of a structural crack. In the figure, the crack is visible as an approximately vertical black line at the middle of the image. The diagonal faint lines evidenced across the image are promoted by surface roughness, which did not influence the Raman results. Also, the representation of the spot of the laser was expanded for its better visualization, once its actual diameter is approximately $1\ \mu m$.

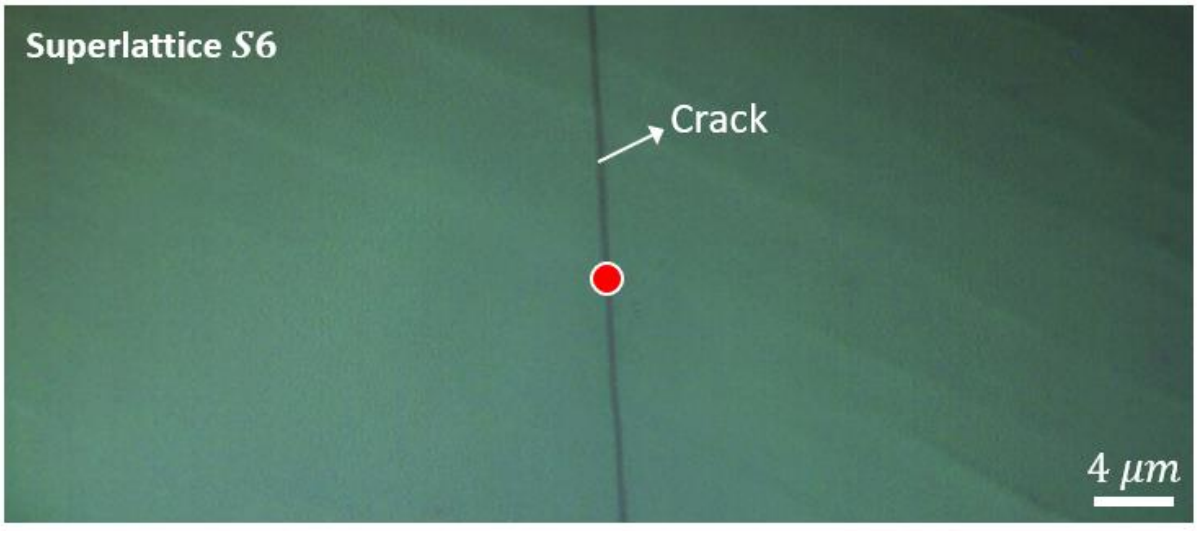

Figure 43 - Image of superlattice $S6$ acquired using optical microscopy indicating the position of Raman analysis on top of the line of a structural crack.

As a comparison between the superlattices, Figure 44 presents images acquired using optical microscopy ($Olympus$, model $MPLanN100x$) for all the superlattices. The apparent difference in color between the superlattices is mostly promoted by the autonomous adjust in contrast executed by the imaging tool of the software $LabSpec\ 5$ ($Horiba\ Jobin-Yvon$), using the light of a high-power lamp ($Euromex$, model $EK-1$) used to illuminate each superlattice during the image acquisition.

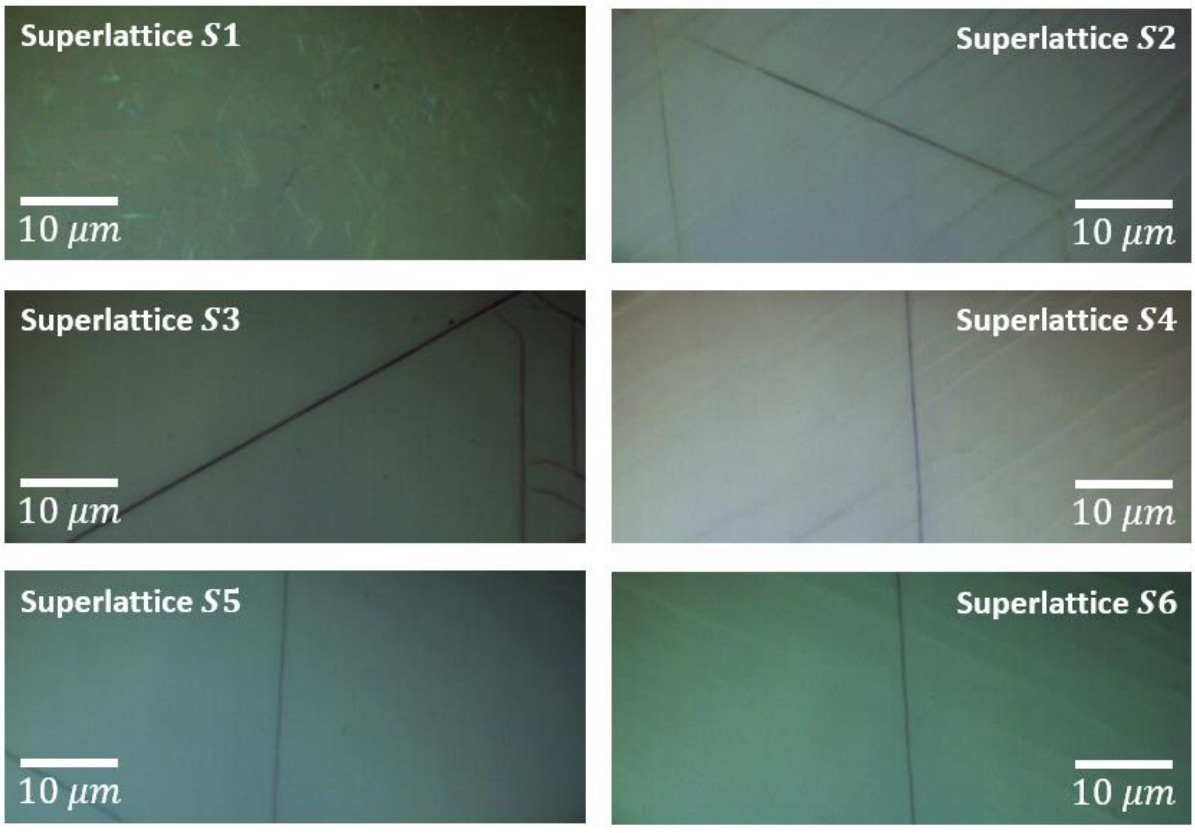

Figure 44 - Image acquired by optical microscopy for each superlattice suing $100x$ of magnification.

As seen in the figure, the cracks are mostly unperceivable in the superlattice with the thinnest layers of GaN. In fact, the presence of cracks in superlattices has been reported as originated in the attempt of releasing tensile strain stored during the epitaxial growth.[192] Therefore, in the case of AlN/GaN superlattices, it is expected that thicker layers GaN would generate more intense conditions of tensile strain along the AlN layers due to the lattice mismatching, which under certain conditions of synthesis would lead to the consequent formation of well defined cracks along the nanostructure. Figure 45 presents the Raman spectrum acquired at five positions of each superlattice.

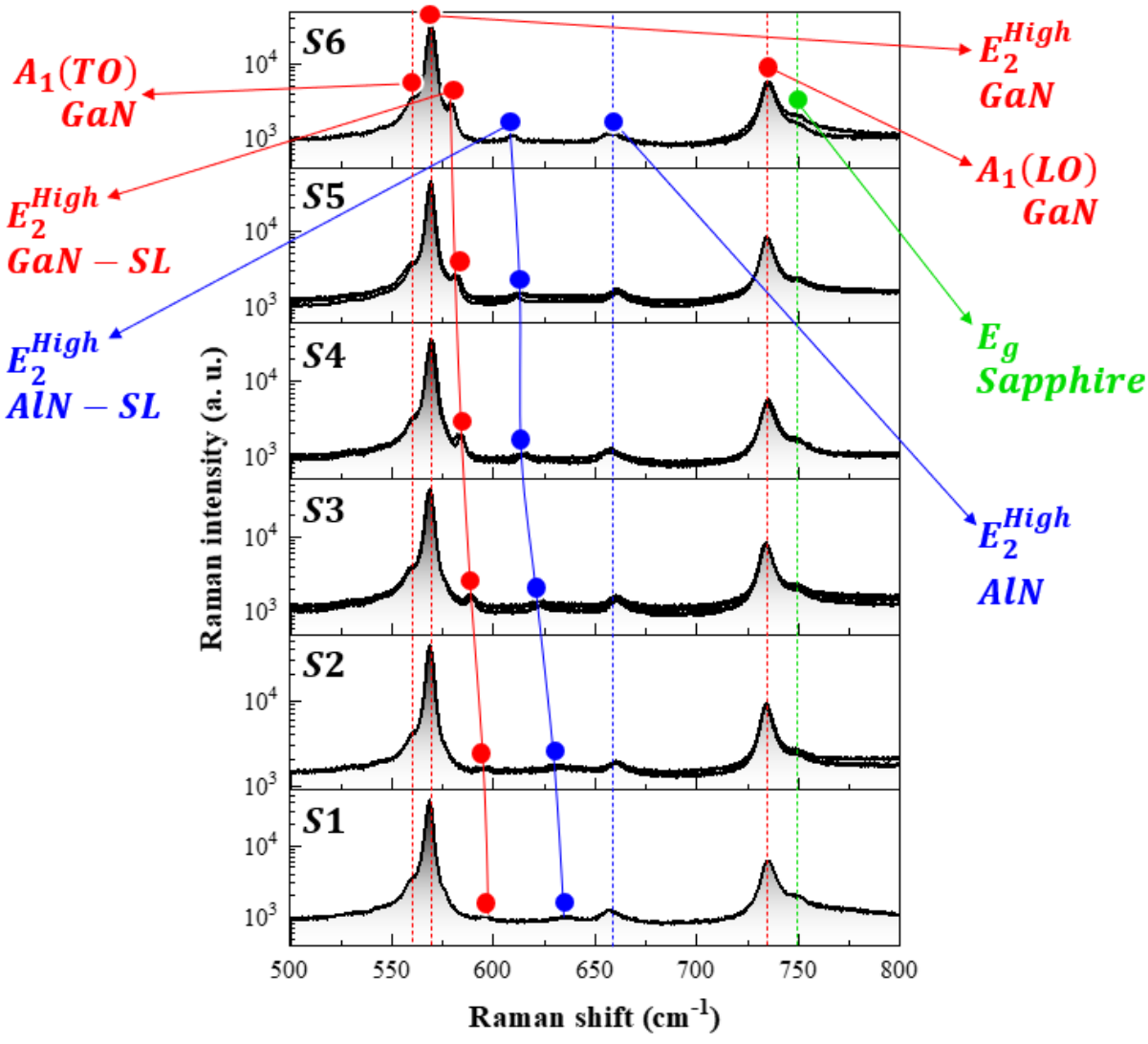

Figure 45 - Raman spectrum acquired at five positions of each superlattice, evidencing the modes from sapphire, AlN and GaN, from template and from periods of each superlattice (SL).

In the figure, it is evident that the only mode considerably dependent on the characteristics of each superlattice is the nonpolar mode $E_2^{High}(AlN - SL, GaN - SL)$ of each nitride, evidenced as a weak mode shifted from the E_2^{High} mode originated from the template. The modes $A_1(TO)$ and $A_1(LO)$ of GaN template, as well as the mode E_g from sapphire, do not vary among the different superlattices. In particular, Figure 46 presents a zoom around the E_2^{High} of each nitride of superlattice $S6$, according to the average of data acquired at five positions.

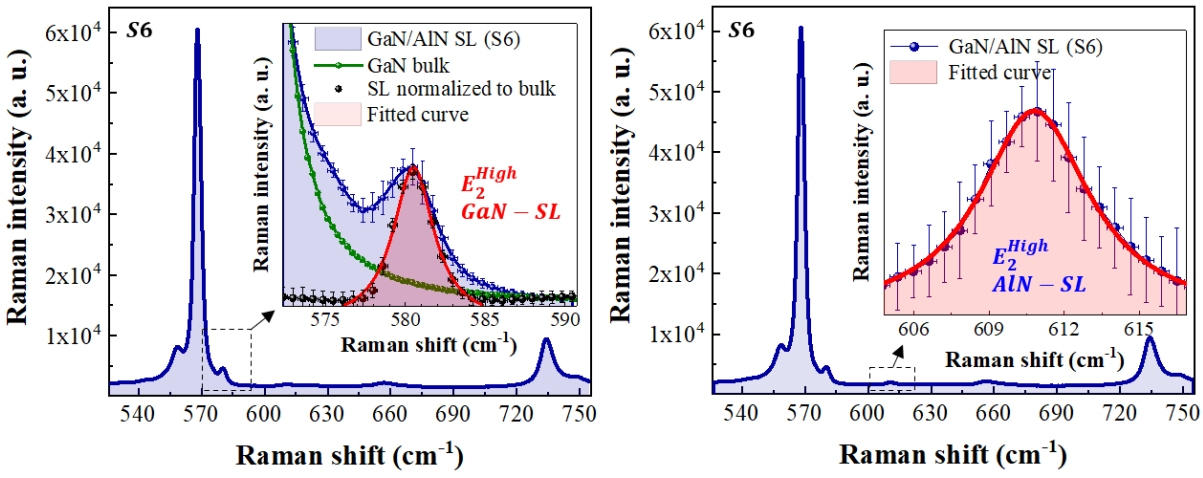

Figure 46 - E_2^{High} mode originated from AlN and GaN at the periods of the superlattice $S6$.

In the figure, the E_2^{High} mode of each nitride localized at the periods of superlattice $S6$ was fitted using a gaussian curve in order to determine the center of mode ($E_2^{High} \approx 579.66 \pm 0.04\, cm^{-1}$ for $GaN - SL$, and $E_2^{High} \approx 609.63 \pm 0.02\, cm^{-1}$ for $AlN - SL$). Additionally, in the case of GaN the E_2^{High} mode originated along the periods of the superlattices is almost hidden inside the E_2^{High} mode produced at the GaN buffer and template, therefore for better visualization the fitted curve represents a normalization between the Raman data from the superlattice and from the substrate. Table 6 presents the values of Raman shift associated to the mode E_2^{High} of each nitride for all the analyzed superlattices.

Table 6 - Raman shift associated to the E_2^{High} mode originated at the periods of each superlattice for AlN and GaN.

Sample	E_2^{High} (cm^{-1}) **GaN − SL**	E_2^{High} (cm^{-1}) **AlN − SL**
S1	608.87 ± 0.02	646.28 ± 0.01
S2	592.21 ± 0.01	632.72 ± 0.02
S3	589.59 ± 0.02	622.83 ± 0.02
S4	584.51 ± 0.04	616.35 ± 0.04
S5	581.86 ± 0.03	613.00 ± 0.03
S6	579.66 ± 0.04	609.63 ± 0.02

Using the measured Raman shift of the nonpolar mode E_2^{High} of each nitride and the strain obtained from XRD results for all the superlattices, the standard linear method correlating Raman shift and strain was tested. Figure 47 compares the acquired experimental data and the expected behavior using the linear method for each superlattice. As a comparison, the data is also fitted to the nonlinear relation obtained using the harmonic approximation defined by $\Delta\omega^i = \omega_0^i\left(\sqrt{\left(1 - K_i\epsilon_{xx}^i\right)} - 1\right)$ in terms of the proportionality constant K_i for AlN and GaN.

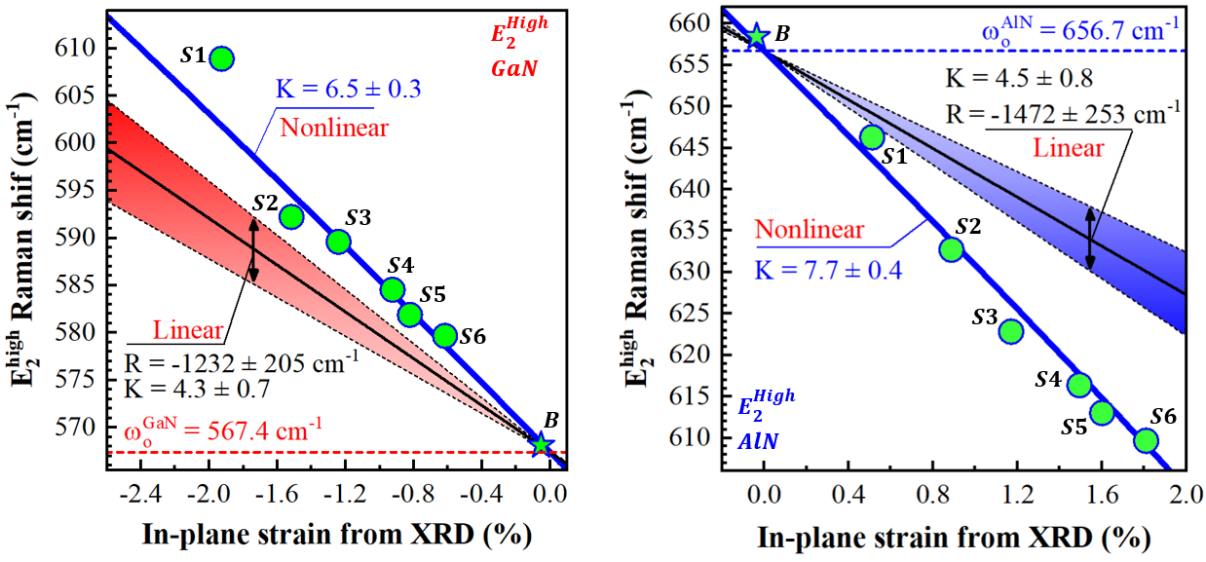

Figure 47 - Comparison between Raman shift and in-plane strain in the superlattices. The dots are experimental data from Raman and XRD, the blue curve traces the average and black curves limiting the colored regions represent the expected values using the linear model. The stars assigned as B are data from substrates of AlN and GaN.

As can be evidenced in the figure, the experimental data is not well represented by the standard linear method in the range of strain at which the layers of the superlattice were being submitted to. In addition, an actual trend can be observed between the E_2^{High} Raman shift and in-plane strain determined by an empirical average constant of proportionality given by:

$$K_{experiment}^{AlN} \approx 7.7 \pm 0.4, \qquad K_{experiment}^{GaN} \approx 6.5 \pm 0.3$$

As an explicit function of the measured Raman shift (ω_i), the in-plane lattice constant (a_{xx}) can be then expressed by:

$$a_{xx} = a_0^i\left[1 + \frac{1}{K_i}\left(1 - \left(\frac{\omega_i}{\omega_0^i}\right)^2\right)\right], \qquad i = \{AlN, GaN\}$$

As a test of effectiveness, the nonlinear model containing the empirical values of the proportionality constant ($K_{experiment}^{AlN,GaN}$) was examined using XRD and Raman results reported in the literature. Table 7 summarizes the tested data set, containing values of Raman shift (ω_{GaN}) associated to the E_2^{High} mode of GaN, and in-plane lattice constants (a_{xx}) obtained by XRD reported by references.

Table 7 - Values of Raman shift of E_2^{High} mode of GaN and in-plane lattice constants obtained from XRD reported in references from the literature.

Sample	E_2^{High} (cm^{-1}) **GaN − SL**	a_{SL} (Å)	***Material***	***Growth technique***
R1	610	3.11246	$AlN/GaN/AlN$ QW	$PAMBE$
R2	605	3.1198	$AlN/GaN/AlN$ QW	$PAMBE$
R3	595	3.13224	$AlN/GaN/AlN$ QW	$PAMBE$
R4	576.9	3.18068	Crack-free $[AlN/GaN]_{10}$ SL	$MOVPE$
R5	575.96	3.18772	Ge-doped $AlGaN$ films	$MOCVD$
R6	573.5	3.16604	Ge-doped $AlGaN$ films	$MOCVD$
R7	572	3.18926	GaN films	$MOCVD$
R8	569.6	3.1873	Cracked $[AlGaN/GaN]_5$ SL	$MOCVD$
R9	568.2	3.18804	$AlGaN$ and GaN	$MOCVD$
R10	565.6	3.1895	$AlGaN/GaN$ layers	$MOCVD$

The results assigned as $R1$, $R2$ and $R3$ were obtained by Qi et al.[26] and they are associated to $AlN/GaN/AlN$ single quantum wells (QW) grown by plasma assisted molecular beam epitaxy ($PAMBE$) varying the thickness of the GaN layer. The results represented by $R4$ were reported by Darakchieva et al.[211] and they are associated to crack-free 10-period AlN/GaN superlattices grown by metalorganic vapor phase epitaxy ($MOVPE$) varying the thickness of both AlN and GaN layers. The results assigned as $R5$ and $R6$ were obtained by Bansal et al.[212] and they are associated to Ge-doped $AlGaN$ films grown using metalorganic chemical vapor

deposition ($MOCVD$). The results displayed as $R7$ were reported by Davydov et al.[199] and represent GaN films grown by $MOCVD$. The results assigned as $R8$ were obtained by Lee et al.[165] and are associated to $AlGaN/GaN$ films also grown by $MOCVD$. The results represented by $R9$ were published by Tripathy et al.[192] and represent $AlGaN/GaN$ long-period superlattices fabricated using $MOCVD$. And finally, the results assigned as $R10$ were obtained by Christy et al.[213] and are associated to $AlGaN/GaN$ layers also grown by $MOCVD$. Figure 48 compares the data from references and the nonlinear model.

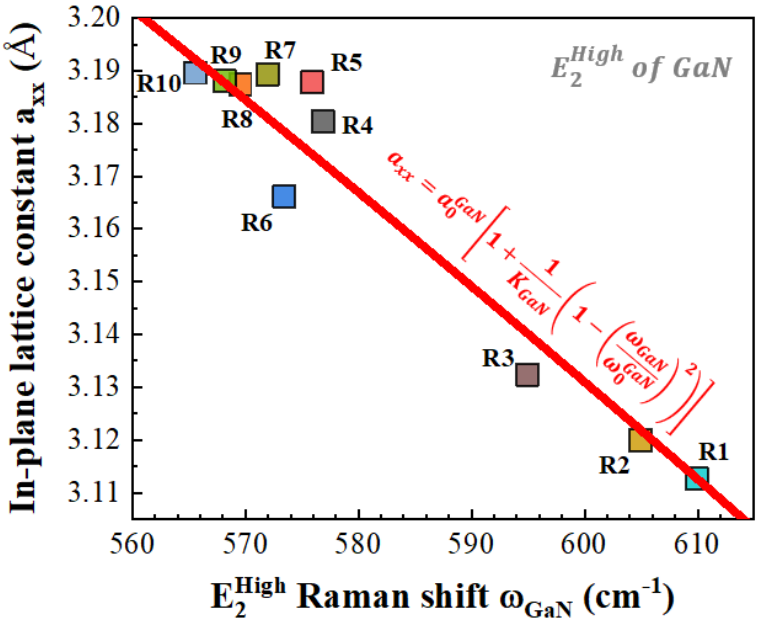

Figure 48 – Comparison between the nonlinear model and a tested data set, containing values of E_2^{High} Raman shift (ω_{GaN}) and XRD in-plane lattice constants (a_{xx}) reported by references.

As seen in the figure, the nonlinear model for GaN seems to be applicable for architectures other than superlattices, optimally describing AlN/GaN heterostructures fabricated by distinct methods of growth, only exhibiting a few considerable deviations in the case of the tested Ge-doped $AlGaN$ films. Likewise for the E_2^{High} mode of AlN, the Table 8 presents its respective values of Raman shift and in-plane lattice constant according to references.

Table 8 - Values of Raman shift of E_2^{High} mode of AlN and in-plane lattice constants obtained from XRD reported in references from the literature.

Sample	E_2^{High} (cm^{-1}) **AlN − SL**	a_{SL} (Å)	***Material***	***Growth technique***
R11	649.06	3.122	$AlN/AlGaN/GaN$	$Amonia - MBE$
R12	649.08	3.1249	$AlN/AlGaN/GaN$	$Amonia - MBE$
R13	648.63	3.1244	$AlN/AlGaN/GaN$	$Amonia - MBE$
R14	649.9	3.1266	$AlGaN/GaN$	$MOCVD$
R15	649.3	3.1279	$AlGaN/GaN$	$MOCVD$
R16	649.9	3.1283	$AlGaN/GaN$	$MOCVD$
R17	621.8	3.16343	$[AlN/GaN]_{5,10,20}$ SL	$PAMBE$
R18	624.8	3.15067	$[AlN/GaN]_{5,10,20}$ SL	$PAMBE$
R19	635.5	3.14382	$[AlN/GaN]_{5,10,20}$ SL	$PAMBE$

Here, the results assigned as $R11$, $R12$ and $R13$ were published by Agrawal et al.[156] and are associated to $AlN/AlGaN/GaN$ layers fabricated using ammonia molecular beam epitaxy ($Ammonia - MBE$) varying the thickness of AlN layers. The results represented by $R14$, $R15$ and $R16$ were reported by Lee et al.[165] and are associated to $AlGaN/GaN$ films grown by $MOCVD$. And finally, the results assigned as $R17$, $R18$ and $R19$ were obtained by Kolomys et al.[206] and represent AlN/GaN superlattices fabricated using $PAMBE$ varying the number of periods of each superlattice. Figure 49 compares the data from references and the nonlinear model.

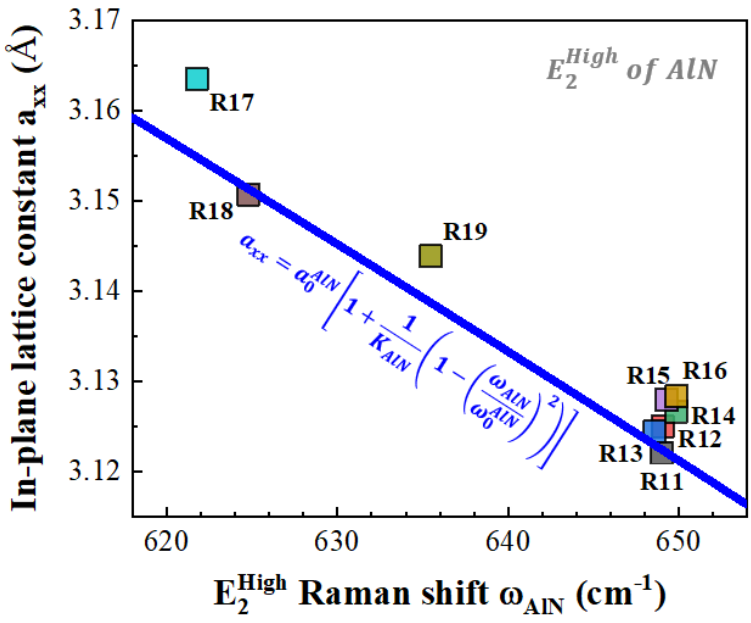

Figure 49 - Comparison between the nonlinear model and a tested data set, containing values of E_2^{High} Raman shift (ω_{AlN}) and XRD in-plane lattice constants (a_{xx}) reported by references.

In the case of AlN, the best correlation between reported results and the nonlinear model was evidenced for heterostructures fabricated using $Ammonia - MBE$, with a few considerable deviations among the remaining data set.

Once the reference testing displayed a reasonable coherence of model correlation, the nonlinear method was used to study the gradient of strain in the vicinity of cracks of each superlattice ($S1$, $S2$, $S3$, $S4$, $S5$ and $S6$). It was expected that the situation of maximum tensile strain would be verified approximately $10\ \mu m$ to $20\ \mu m$ away from the line of cracking, as previously reported in the case of AlN/GaN structures.[191] Keeping that in mind, a surface region of approximately $45\ \mu m$-wide of each superlattice was linearly scanned using micro-Raman, by acquiring the Raman data five times at the same position every $1\ \mu m$. The location of analysis for each superlattice prioritized selecting a long and defined crack and crossing it perpendicularly, trying to have at least $20\ \mu m$ of crack-free surface around the analyzed line of crack. In the case of superlattice $S1$, which contains the thinnest layers of GaN, once the lines of cracks are visually faint and not very well defined, a random position along the surface was chosen for the linear scan. The variation of the nonpolar E_2^{High} mode of each nitride was tracked along the linear scanning, and then used to determine the local value of compressive and tensile strain in the AlN and GaN layers of the periods of each superlattice displayed in Figure 50.

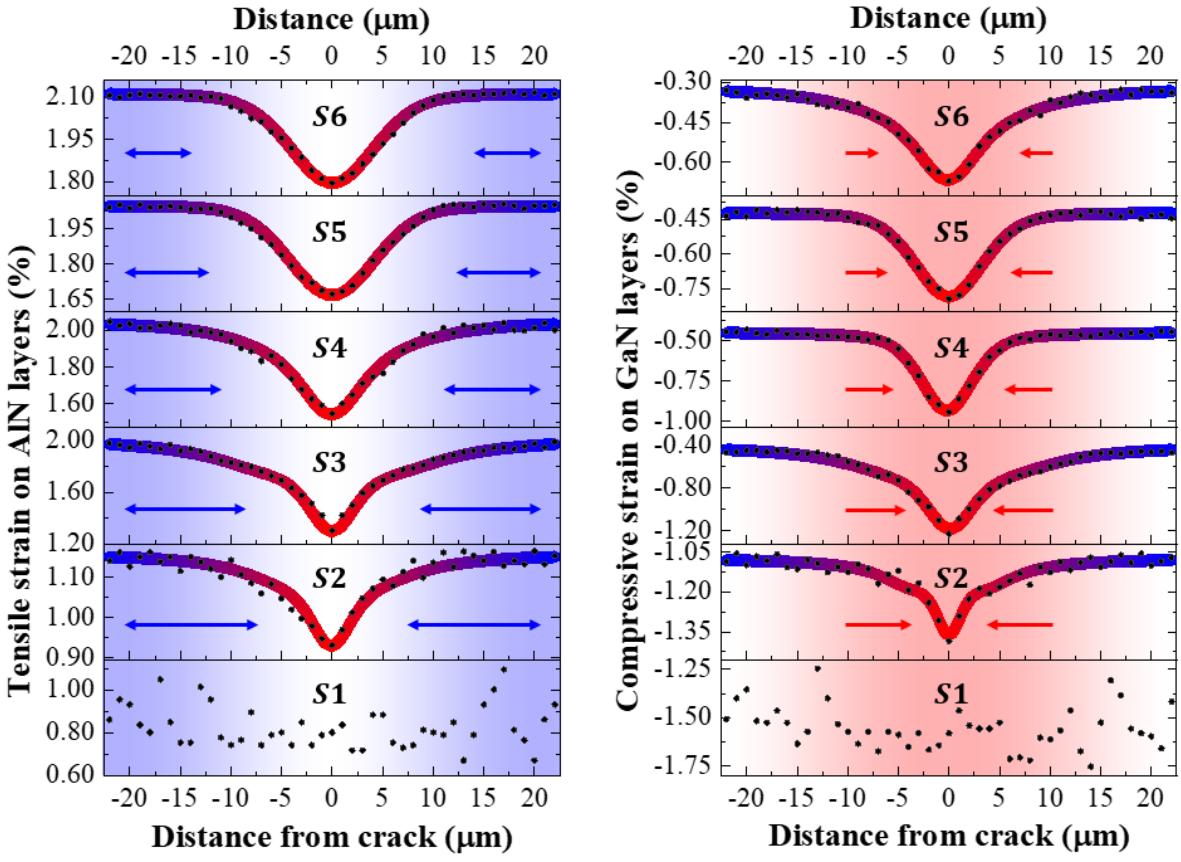

Figure 50 - Linear strain scanning across a crack of each superlattice.

As seen in the figure, the intensity of tensile strain increases along the direction outwards the line of crack, correspondent to the position zero in the scanning scale for the superlattices $S2$, $S3$, $S4$, $S5$ and $S6$. Additionally, the gradient of strain seems to become more abrupt around cracks in the superlattices with the thinnest layers of GaN, perceivable as a progressive increasing in the rate of strain variation around zero when decreasing the thickness of GaN layers. This figure also confirms that, for these AlN/GaN superlattices, the residual value of in-plane strain reaches a status of homogeneity at distances farther than approximately $15\ \mu m$ away from lines of cracks. Furthermore, it is possible to notice that the overall saturated level of residual tensile strain has both its maximum and minimum magnitudes less intense in the superlattices with the thinnest layers of GaN in the investigated spatial range of scanning. On the other hand, the maximum and minimum values of compressive strain are less intense in the superlattices with the thicker layers of GaN, which therefore counterbalances the local condition of tensile strain at each position of the superlattices. Figure 51 compares each linear scan with XRD results.

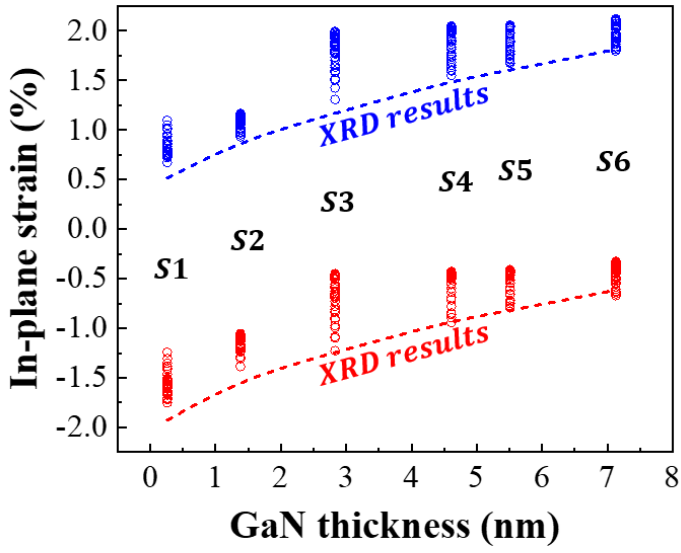

Figure 51 - Comparison between range of strain obtained in linear scanning and XRD results for each superlattice.

As seen in the figure, the XRD results for each superlattice represented a situation of extremum in the values of in-plane strain measured in each linear scanning, and more precisely, they correspond to the conditions of minimum tensile strain and maximum compressive strain. It means that the XRD data referred to the exact positions of lines of cracks, which exhibit similar values of low tensile and high compressive in-plane strain.

In order to study the contribution of multiple lines of cracks on the effective compressive and tensile local strain of AlN and GaN layers in the periods of the superlattices, a set of bidimensional Raman mappings were performed. Due to its better definition of lines of cracks, the superlattice $S6$ was chosen for this analysis. At first, a rectangular region of approximately $30\ \mu m\ x\ 40\ \mu m$ containing many lines of cracks was scanned, acquiring Raman data five times at each position every $1\ \mu m$. The variation of the nonpolar E_2^{High} mode of each nitride was tracked along the bidimensional mapping, and then used to determine the local value of compressive and tensile strain in the AlN and GaN layers of the periods of superlattice $S6$. Figure 52, acquired using optical microscopy, evidences the investigated area of superlattice $S6$.

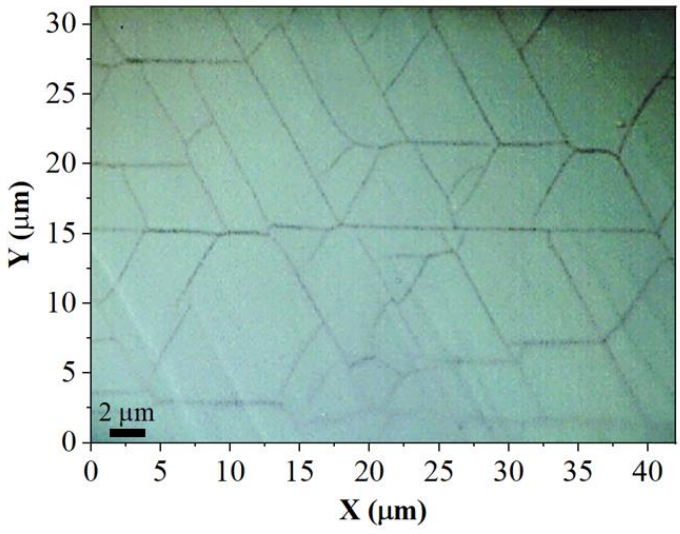

Figure 52 - Investigated area of superlattice S6.

Using the nonlinear model applied to every Raman spectrum acquired at each position along the analyzed area, the distributions of values of tensile and compressive strain in the layers of AlN and GaN were determined. In Figure 53 the compressive strain in the GaN layers is represented as a heat map across all the investigated area.

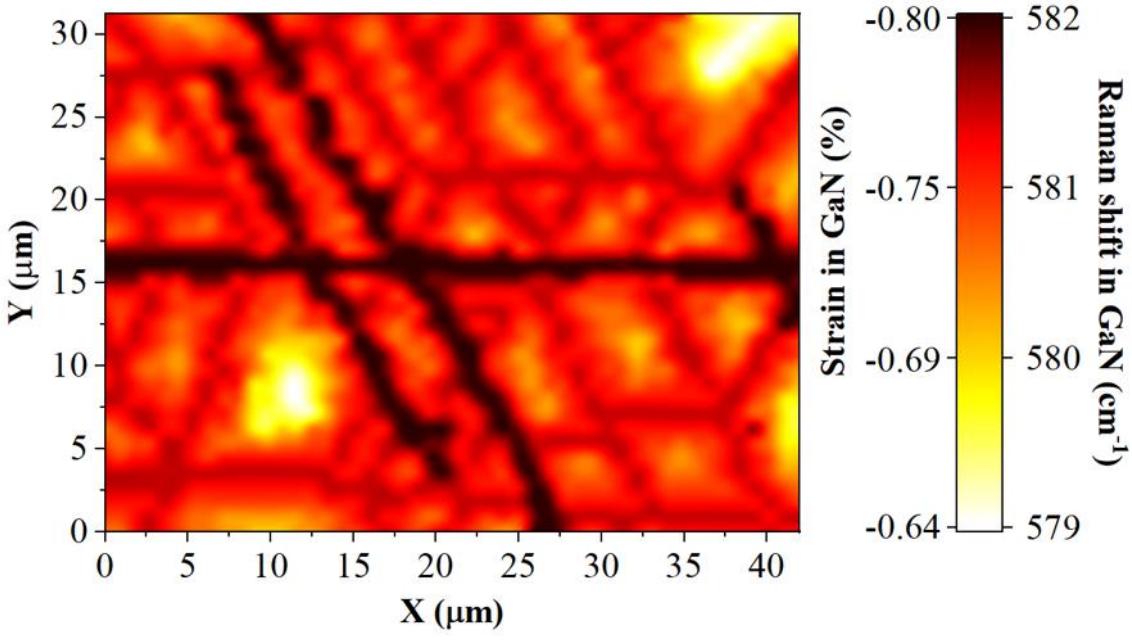

Figure 53 - Compressive strain in the GaN layers along a region of superlattice $S6$.

From the Raman mapping it was possible to distinguish the positions of each line of crack, as well as to evidence different types of crack: long, well defined cracks that are likely to be produced during the nanostructure growth; and short, faint cracks, which origin seems to be associated to the process of cooling down after the epitaxial growth.[191] It is noticeable that each

line of crack contributes directionally to the local strain, and only a few positions relatively distant from any crack presented low levels of compressive strain. Likewise, in Figure 54 the tensile strain in the AlN layers is represented as a heat map across all the investigated area.

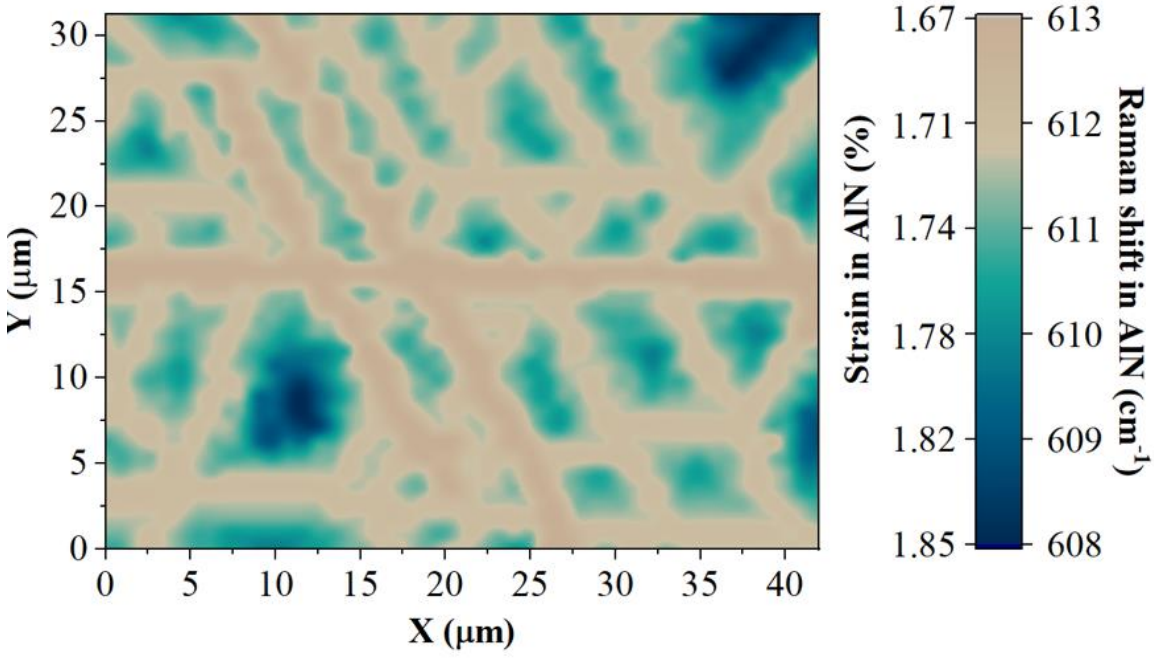

Figure 54 - Tensile strain in the AlN layers along a region of superlattice $S6$.

In the figure, it is very clear that the formation of cracks leads to the relaxation of tensile strain in the superlattice, and just like for GaN, there is also a distribution of tensile strain in the layers of AlN, increasing its magnitude along the direction outwards any line of crack. Additionally, due to the high density of cracks in the analyzed area very few positions presented reasonable low levels of tensile strain, once every position is surrounded by a considerably high number of cracks, that affect the effective condition of local strain. Therefore, in order to evidence saturation levels of compressive and tensile strain, an area along superlattice $S6$ containing the intersection of lines of cracks and also surrounded by an extended crack-free surface was selected and investigated using Raman mapping. Figure 55, acquired using optical microscopy, evidences the investigated area of superlattice $S6$.

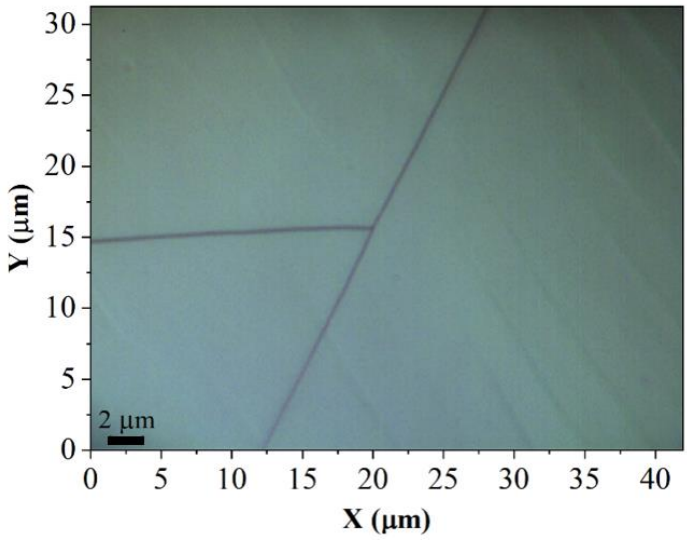

Figure 55 - Investigated area of superlattice $S6$.

Once again, using the nonlinear model applied to the Raman data obtained at each position along the analyzed area every $1\,\mu m$, the distributions of values of tensile and compressive strain in the layers of AlN and GaN were determined. Figure 56 presents the compressive strain in the GaN layers of superlattice $S6$ as a heat map across all the investigated area.

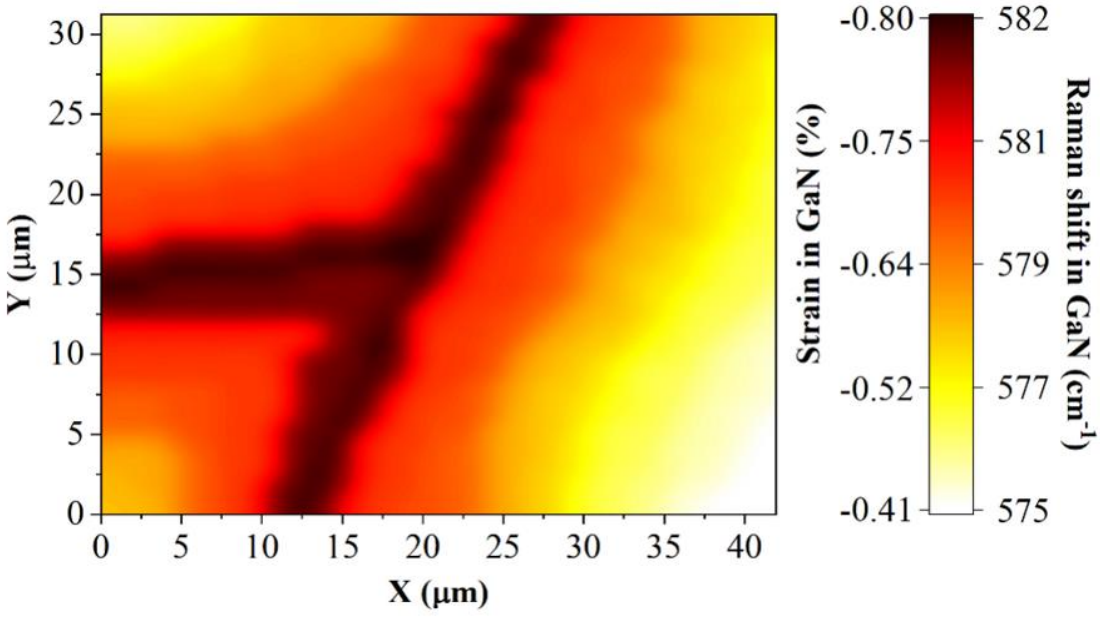

Figure 56 - Compressive strain in the GaN layers along a region of superlattice $S6$.

In the Raman mapping it is possible to evidence very clearly the distribution of strain along the analyzed area, reaching higher levels of compressive strain at the top of the lines of cracks and gradually becoming less intense in the directions oriented away from any crack. Similarly,

in Figure 57 the tensile strain in the AlN layers is represented as a heat map across all the investigated area.

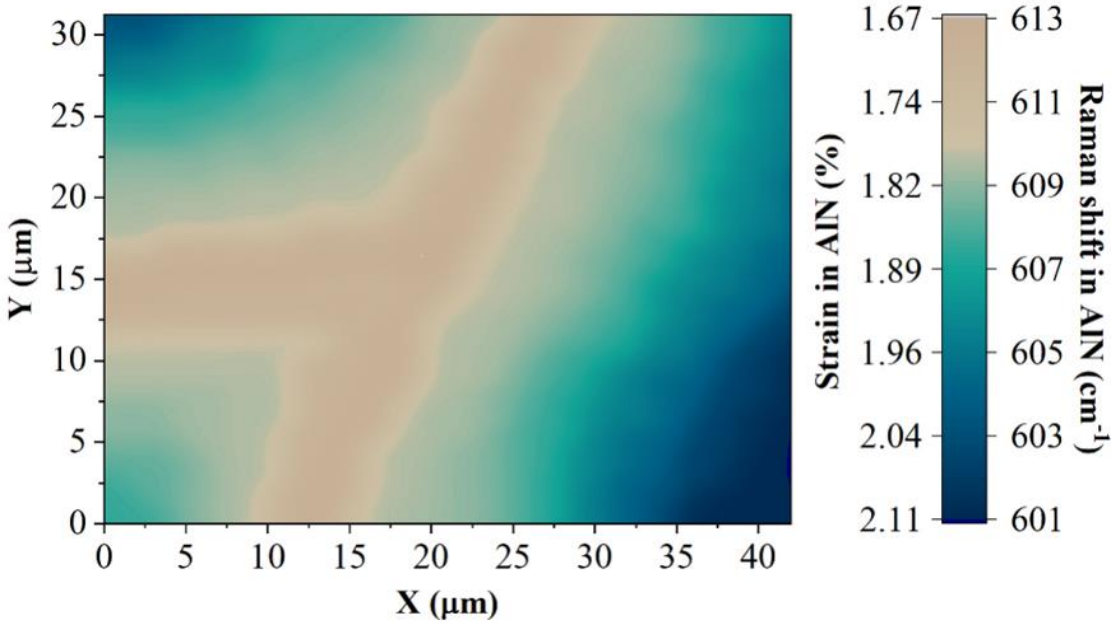

Figure 57 - Tensile strain in the AlN layers along a region of superlattice $S6$.

Therefore, it is evident that the technique of micro-Raman represents a suitable tool to study the distribution of in-plane strain in nanostructures. As verified previously using data from references, the nonlinear model based on a proportionality constant allows to summarize the material's elastic information in a single parameter ($K_{AlN,GaN}$), which was here obtained experimentally for AlN and GaN and used in multiple investigations.

5.5 Future perspectives

Despite its proved applicability at room temperature with consistent and reproductible results, the nonlinear model here presented does not contemplate the anharmonic effect of thermal dilation. Therefore, a further development of this research could be accomplished by acquiring Raman data at different temperatures, which could be used to elaborate a broader model for considering thermal dependence in strain analysis. Additionally, and endeavoring applications in the electronic and space industry, besides considerations concerning thermal conditions, the presence of magnetic fields could also be investigated.

As a step further towards application in the photonics industry, the six 30-period superlattices of this study were also evaluated according to their GaN luminescent emission. It was performed by acquiring luminescent data of each superlattice using the Photoluminescence (PL) technique as described in $Chapter\ 4$. Figure 58 presents the variation of the optical band gap of GaN layers using with multiple levels of excitation intensity for each superlattice.

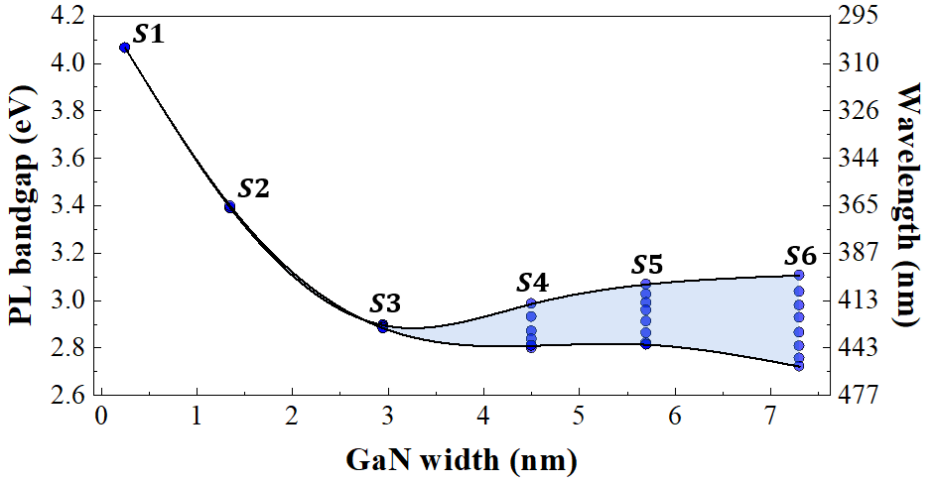

Figure 58 - Optical band gap of GaN layers measured using photoluminescence with multiple levels of excitation intensity for each superlattice.

It was expected that due to the internal electric field along the layers of AlN and GaN, which are perceived by carriers as quantum barriers and quantum wells respectively, the electronic deexcitation back from GaN's conduction band to its valence band would be modified, producing a shifted PL emission associated to the superlattice's effective optical band gap. The dependence between features of III-nitride superlattices, such as the thickness of its layers, and the resulting bandgap energy evidenced in the PL characterization, has been associated to the quantum-confined Stark effect, due to the internal electric field of each layer modifying the band energy diagram of the material, which allows the development of customizable light emitting devices by band gap engineering.[184]

Chapter 6: Conclusion

In this study, an alternative method for investigating strain in nanostructures at microscale was presented. By correlating x-ray diffraction and micro-Raman results using lattice coherence, a nonlinear correlation model between strain and Raman shift was formulated. In comparison with the traditional linear method of strain analysis using Raman shift, the nonlinear model allows the acquisition of more precise values of in-plane strain, mostly due to the imprecision in determining the multiple parameters of elastic constants and deformation potentials necessary for the linear method. On the other hand, by an empirical investigation, the nonlinear model depends on only one single parameter that summarizes the elastic information of the material. An association between the two methods was also presented for purposes of comparison. The nonlinear model was tested using data reported in references from the literature, and represented a good approximation of values of in-plane lattice constants for different categories of structures, also fabricated by distinct methods of growth. By using the micro-Raman technique, the model was employed in the analysis of strain mapping on a set of set six 30-period AlN/GaN superlattices. The distribution of values of strain measured using Raman indicated that the x-ray diffraction results were originated in specific areas of the superlattices, where the in-plane tensile strain was minimum and the compressive strain was maximum. By using optical microscopy, a mosaic of structural cracks was identified along the superlattices, which are responsible for minimizing the residual in-plane tensile strain in these nanostructures. And by using electronic microscopy the layers of AlN and GaN of multiple periods of a superlattice were observed, measured and analyzed using energy dispersive x-ray spectroscopy in order to evaluate the atomic distribution along the layers. Using high spatial resolution, the monolayers of each nitride were measured, allowing to obtain information about their axial lattice constant. Complementary, additions to the model were presented, in order to consider also effects of temperature and magnetic fields, as well as its application in band gap engineering.

References

1. Tyndall J. XXIII. On the absorption and radiation of heat by gases and vapours, and on the physical connexion of radiation, absorption, and conduction.—The bakerian lecture. The London, Edinburgh, and Dublin Philosophical Magazine and Journal of Science. 1861 Sep 1;22(146):169-94.
2. Twersky V. Rayleigh scattering. Applied Optics. 1964 Oct 1;3(10):1150-62.
3. Hertz H. Ueber einen Einfluss des ultravioletten Lichtes auf die electrische Entladung. Annalen der Physik. 1887;267(8):983-1000.
4. Stuewer RH. The Compton effect: transition to quantum mechanics. Annalen der Physik. 2000 Nov;9(11-12):975-89.
5. Thomson JJ. The structure of the atom. Academie Royale de Belgique; 1913.
6. Maxwell JC. VIII. A dynamical theory of the electromagnetic field. Philosophical transactions of the Royal Society of London. 1865 Dec 31(155):459-512.
7. Raman CV, Krishnan KS. A new type of secondary radiation. Nature. 1928 Mar;121(3048):501-2.
8. Kohlrausch K. W. F. Der Smekal-Raman Effekt, Springer, Berlin, 1931.
9. Placzek G.: The Rayleigh and Raman scattering, edited by: Marx E., Leipzig, Germany: Akademische Verlagsgesellschaft, 1934.
10. Stokes GG. XXX. On the change of refrangibility of light. Philosophical transactions of the Royal Society of London. 1852 Dec 31(142):463-562.
11. Jabloński A. General theory of pressure broadening of spectral lines. Physical Review. 1945 Aug 1;68(3-4):78.
12. Ashcroft NW and Mermin ND. Solid State Physics (Holt-Saunders, Philadelphia, 1976).
13. Loudon R. The Raman effect in crystals. Advances in Physics. 1964 Oct 1;13(52):423-82.
14. Cantarero A. Raman scattering applied to materials science. Procedia Materials Science. 2015 Jan 1;9:113-22.
15. Johnson BB, Peticolas WL. The resonant Raman effect. Annual Review of Physical Chemistry. 1976 Oct;27(1):465-521.
16. Debye P. Zur theorie der spezifischen wärmen. Annalen der Physik. 1912;344(14):789-839.
17. Martin JK. Einstein, Specific Heai and the Early Quantum Theo. 1965, 148 (3667): 173-180.
18. Einstein A. Concerning an heuristic point of view toward the emission and transformation of light. American Journal of Physics. 1965 May;33(5):367.
19. Walker CT, Slack GA. Who Named the-ON's?. American journal of physics. 1970 Dec;38(12):1380-9.
20. Keresztury, G. Raman Spectroscopy; Theory, in Handbook of Vibrational Spectroscopy; Chalmers, J. M.; Griffiths, P. R., Eds.; Wiley & Sons: Chichester, 2002; Vol. 1, p 71.

21. Albrecht AC. On the theory of Raman intensities. The Journal of chemical physics. 1961 May;34(5):1476-84.

22. Bernardini F, Fiorentini V, Vanderbilt D. Offsets and polarization at strained AlN/GaN polar interfaces. MRS Online Proceedings Library (OPL). 1996;449.

23. Wieboldt D, Heintz , Wall M. Fundamentals of Raman Polarization Microscopy. Thermo Fisher Scientific, 2016.

24. Abramowitz M, Stegun IA, editors. Handbook of mathematical functions with formulas, graphs, and mathematical tables. US Government printing office; 1964.

25. Marghitu D, Raju PK, Mazilu D. 6 Theory of Vibration. Mechanical Engineer's Handbook. 2001 Jan 1:339.

26. Qi M, Li G, Protasenko V, Zhao P, Verma J, Song B, Ganguly S, Zhu M, Hu Z, Yan X, Mintairov A. Dual optical marker Raman characterization of strained GaN-channels on AlN using AlN/GaN/AlN quantum wells and 15N isotopes. Applied Physics Letters. 2015 Jan 26;106(4):041906.

27. Rychlewski J. On Hooke's law. Journal of Applied Mathematics and Mechanics. 1984 Jan 1;48(3):303-14.

28. Shabana AA. Theory of vibration. New York: Springer-Verlag; 1991 Jan.

29. Yonenaga I, Motoki K. Yield strength and dislocation mobility in plastically deformed bulk single-crystal GaN. Journal of Applied Physics. 2001 Dec 15;90(12):6539-41.

30. Nowak R, Pessa M, Suganuma M, Leszczynski M, Grzegory I, Porowski S, Yoshida F. Elastic and plastic properties of GaN determined by nano-indentation of bulk crystal. Applied Physics Letters. 1999 Oct 4;75(14):2070-2.

31. Klein MV, Ganguly BN, Colwell PJ. Theoretical and experimental study of Raman scattering from coupled LO-phonon-plasmon modes in silicon carbide. Physical Review B. 1972 Sep 15;6(6):2380.

32. Fujioka Y. Influence of temperature on Raman lines. Nature. 1929 Jul;124(3114):11.

33. Strommen DP, Nakamoto K. Resonance raman spectroscopy. Journal of Chemical Education. 1977 Aug;54(8):474.

34. Bohning JJ, Misra TN, Choudhury M. The Raman effect. An International Historic Chemical Landmark. American Chemical Society and Indian Association for the Cultivation of Science. Calcutta, 1998.

35. Brand JC. The discovery of the Raman effect. Notes and Records of the Royal Society of London. 1989 Jan 31;43(1):1-23.

36. Mair SL, Barnea Z. Anharmonic thermal vibrations in wurtzite structures. Acta Crystallographica Section A: Crystal Physics, Diffraction, Theoretical and General Crystallography. 1975 Mar 1;31(2):201-7.

37. Bhagavantam S. Effect of pressure on Raman spectra. Nature. 1931 Aug;128(3222):188.

38. Faugeras C, Kossacki P, Basko DM, Amado M, Sprinkle M, Berger C, De Heer WA, Potemski M. Effect of a magnetic field on the two-phonon Raman scattering in graphene. Physical Review B. 2010 Apr 19;81(15):155436.

39. Hotokka M. Calculation of vibrational frequencies by molecular mechanics. Handbook of Vibrational Spectroscopy. 2006 Jun 15.

40. Slavič J, Boltezar M, Mrsnik M, Cesnik M, Javh J. Vibration Fatigue by Spectral Methods: From Structural Dynamics to Fatigue Damage–Theory and Experiments. Elsevier; 2020 Aug 20.

41. Young T. A course of lectures on natural philosophy and the mechanical arts. Taylor and Walton; 1845.

42. Euler L, Burckard EL. Dissertatio physica de sono. Thurnisii; 1727.

43. Cheng RT, Ling CH, Gartner JW, Wang PF. Estimates of bottom roughness length and bottom shear stress in South San Francisco Bay, California. Journal of Geophysical Research: Oceans. 1999 Apr 15;104(C4):7715-28.

44. Zhang PZ, Wen XZ, Shen ZK, Chen JH. Oblique, high-angle, listric-reverse faulting and associated development of strain: The Wenchuan earthquake of May 12, 2008, Sichuan, China. Annual Review of Earth and Planetary Sciences. 2010 May 30;38:353-82.

45. Komarova MA, Gorodtsov VA, Lisovenko DS. Variability of Young's modulus and Poisson's ratio of hexagonal crystals. InIOP Conference Series: Materials Science and Engineering 2018 Apr 1 (Vol. 347, No. 1, p. 012019). IOP Publishing.

46. Levy M, Bass H, Stern R. Modern acoustical techniques for the measurement of mechanical properties. Elsevier; 2001 Oct 16.

47. Ganesan S, Maradudin AA, Oitmaa J. A lattice theory of morphic effects in crystals of the diamond structure. Annals of Physics. 1970 Feb 1;56(2):556-94.

48. Fast L, Wills JM, Johansson B, Eriksson O. Elastic constants of hexagonal transition metals: Theory. Physical Review B. 1995 Jun 15;51(24):17431.

49. Walpole LJ. Fourth-rank tensors of the thirty-two crystal classes: multiplication tables. Proceedings of the Royal Society of London. A. Mathematical and Physical Sciences. 1984 Jan 9;391(1800):149-79.

50. Schwarz RB, Khachaturyan K, Weber ER. Elastic moduli of gallium nitride. Applied Physics Letters. 1997 Mar 3;70(9):1122-4.

51. Polian A, Grimsditch M, Grzegory I. Elastic constants of gallium nitride. Journal of Applied Physics. 1996 Mar 15;79(6):3343-4.

52. Wright AF. Elastic properties of zinc-blende and wurtzite AlN, GaN, and InN. Journal of Applied physics. 1997 Sep 15;82(6):2833-9.

53. Kim K, Lambrecht WR, Segall B. Elastic constants and related properties of tetrahedrally bonded BN, AlN, GaN, and InN. Physical Review B. 1996 Jun 15;53(24):16310.

54. Lu JY, Deng DM, Wang Y, Chen KJ, Lau KM, Zhang TY. Phonon deformation potentials of hexagonal GaN studied by biaxial stress modulation. AIP Advances. 2011 Sep 8;1(3):032132.

55. Kholkin AL, Pertsev NA, Goltsev AV. Piezoelectricity and crystal symmetry. InPiezoelectric and Acoustic Materials for Transducer Applications 2008 (pp. 17-38). Springer, Boston, MA.

56. Glasser ML. Symmetry properties of the wurtzite structure. Journal of Physics and Chemistry of Solids. 1959 Jul 1;10(2-3):229-41.

57. Ambacher O, Majewski J, Miskys C, Link A, Hermann M, Eickhoff M, Stutzmann M, Bernardini F, Fiorentini V, Tilak V, Schaff B. Pyroelectric properties of Al (In) GaN/GaN hetero-and quantum well structures. Journal of physics: condensed matter. 2002 Mar 22;14(13):3399.

58. Ribbe PH, Gibbs GV. The crystal structure of topaz and its relation to physical properties. American Mineralogist: Journal of Earth and Planetary Materials. 1971 Feb 1;56(1-2):24-30.

59. Altmann SL, Herzig P. Point-group theory tables. Oxford; 1994.

60. Dresselhaus MS, Dresselhaus G, Jorio A. Applications of group theory to the physics of solids.

61. Chowdhury S. Gallium nitride based power switches for next generation of power conversion. physica status solidi (a). 2015 May;212(5):1066-74.

62. Momida H, Oguchi T. Effects of lattice parameters on piezoelectric constants in wurtzite materials: A theoretical study using first-principles and statistical-learning methods. Applied Physics Express. 2018 Feb 28;11(4):041201.

63. Morkoç H. Handbook of Nitride Semiconductors and Devices, GaN-Based Optical and Electronic Devices, Volume. Wiley-VCH, Weinheim: Chichester; 2008.

64. Gleize J, Demangeot F, Frandon J, Renucci MA, Widmann F, Daudin B. Phonons in a strained hexagonal GaN–AlN superlattice. Applied physics letters. 1999 Feb 1;74(5):703-5.

65. Marmalyuk AA, Akchurin RK, Gorbylev VA. Theoretical calculation of the Debye temperature and temperature dependence of heat capacity of aluminum, gallium and indium nitrides. Teplofizika vysokikh temperatur. 1998;36(5):839-42.

66. Maxted EB. Ueber die Nitride von Eisen, Nickel und Kobalt: Ueber das Bleicoulometer. Ebering; 1911.

67. Frentrup M, Lee LY, Sahonta SL, Kappers MJ, Massabuau F, Gupta P, Oliver RA, Humphreys CJ, Wallis DJ. X-ray diffraction analysis of cubic zincblende III-nitrides. Journal of Physics D: Applied Physics. 2017 Sep 26;50(43):433002.

68. Ahmed R, Akbarzadeh H. A first principle study of band structure of III-nitride compounds. Physica B: Condensed Matter. 2005 Dec 15;370(1-4):52-60.

69. Johnson WC, Parson JB, Crew MC. Nitrogen compounds of gallium. iii. The journal of physical chemistry. 2002 May 1;36(10):2651-4.

70. S. Oktyabrsky, Defects Related to Zinc Blende and Wurtzite Phases in III-Nitride Heterostructures. Encyclopedia of Materials: Science and Technology. Elsevier, 2001.

71. Henini M, Razeghi M, Kamiyama S, Amano H, Akasaki I. Optoelectronic Devices: III Nitrides. Elsevier; 2004 Dec 17.

72. Zhang JM, Zhang Y, Xu KW, Ji V. Anisotropic elasticity in hexagonal crystals. Thin Solid Films. 2007 Jun 13;515(17):7020-4.

73. Tinkham M. Group theory and quantum mechanics. Courier Corporation; 2003 Dec 17.

74. Zhang J, Wang C. Effect of the electric field on the mechanical properties of gallium nitride nanowires. EPL (Europhysics Letters). 2014 Feb 10;105(2):28004.

75. Li X, Maute K, Dunn ML, Yang R. Strain effects on the thermal conductivity of nanostructures. Physical Review B. 2010 Jun 18;81(24):245318.

76. Davydov VY, Kitaev YE, Goncharuk IN, Smirnov AN, Graul J, Semchinova O, Uffmann D, Smirnov MB, Mirgorodsky AP, Evarestov RA. Phonon dispersion and Raman scattering in hexagonal GaN and AlN. Physical Review B. 1998 Nov 15;58(19):12899.

77. Kisielowski C, Krüger J, Ruvimov S, Suski T, Ager III JW, Jones E, Liliental-Weber Z, Rubin M, Weber ER, Bremser MD, Davis RF. Strain-related phenomena in GaN thin films. Physical review B. 1996 Dec 15;54(24):17745.

78. Allman GJ. Greek Geometry from Thales to Euclid. Hermathena. 1877 Jan 1;3(5):160-207.

79. Paufler P, Filatov SK. ES Fedorov promoting the Russian-German scientific interrelationship. Minerals. 2020 Feb;10(2):181.

80. Koster GF. Space groups and their representations. InSolid state physics 1957 Jan 1 (Vol. 5, pp. 173-256). Academic Press.

81. Nazzi F. The hexagonal shape of the honeycomb cells depends on the construction behavior of bees. Scientific reports. 2016 Jun 20;6(1):1-6.

82. Burckhardt JJ. Zur geschichte der entdeckung der 230 raumgruppen. Archive for History of Exact Sciences. 1967 Oct 4;4(3):235-46.

83. Kunert HW. Multi-phonon processes in C6V4 (P63mc) hexagonal semiconductors: GaN, ZnO, ZnS, BeO, CdS, and Al2O3–sapphire: D3d6 (R3c). physica status solidi (c). 2004 Feb;1(2):206-12.

84. Ambacher O. Growth and applications of group III-nitrides. Journal of physics D: Applied physics. 1998 Oct 21;31(20):2653.

85. Davydov SY. Evaluation of physical parameters for the group III nitrates: BN, AlN, GaN, and InN. Semiconductors. 2002 Jan;36(1):41-4.

86. McNeil LE, Grimsditch M, French RH. Vibrational spectroscopy of aluminum nitride. Journal of the American Ceramic Society. 1993 May;76(5):1132-6.

87. Pezzotti G, Sueoka H, Porporati AA, Manghnani M, Zhu W. Raman tensor elements for wurtzitic GaN and their application to assess crystallographic orientation at film/substrate interfaces. Journal of Applied Physics. 2011 Jul 1;110(1):013527.

88. Galsin JS. Crystal structure of solids. Solid State Physics. Elsevier, 2019:1-36.

89. Andiwijayakusuma D, Saito M, Purqon A. Density functional theory study: Electronic structures of RE: GaN in wurtzite Gα15RE1N16. InJournal of Physics: Conference Series 2016 Aug 1 (Vol. 739, No. 1, p. 012027). IOP Publishing.

90. Romanov AE, Baker TJ, Nakamura S, Speck JS, ERATO/JST UCSB Group. Strain-induced polarization in wurtzite III-nitride semipolar layers. Journal of Applied Physics. 2006 Jul 15;100(2):023522.

91. Yan Q, Rinke P, Scheffler M, Van de Walle CG. Strain effects in group-III nitrides: Deformation potentials for AlN, GaN, and InN. Applied Physics Letters. 2009 Sep 21;95(12):121111.

92. Reiner M, Pietschnig R, Ostermaier C. Tracking the effect of adatom electronegativity on systematically modified AlGaN/GaN Schottky interfaces. ACS applied materials & interfaces. 2015 Oct 21;7(41):23124-31.

93. Gillespie RJ. The valence-shell electron-pair repulsion (VSEPR) theory of directed valency. Journal of Chemical Education. 1963 Jun;40(6):295.

94. Seward WD, Narayanamurti V. Rotational degrees of freedom of molecules in solids. I. The cyanide ion in alkali halides. Physical Review. 1966 Aug 5;148(1):463.

95. Kunert HW. Allowed combinations and overtones of vibrational modes in wurtzite GaN. Applied surface science. 2003 May 15;212:890-6.

96. Ishioka K, Kato K, Ohashi N, Haneda H, Kitajima M, Petek H. The effect of n-and p-type doping on coherent phonons in GaN. Journal of Physics: Condensed Matter. 2013 Apr 25;25(20):205404.

97. Mitroy JA, Safronova MS, Clark CW. Theory and applications of atomic and ionic polarizabilities. Journal of Physics B: Atomic, Molecular and Optical Physics. 2010 Oct 4;43(20):202001.

98. Kozawa T, Kachi T, Kano H, Taga Y, Hashimoto M, Koide N, Manabe K. Raman scattering from LO phonon-plasmon coupled modes in gallium nitride. Journal of Applied Physics. 1994 Jan 15;75(2):1098-101.

99. Grille H, Schnittler C, Bechstedt F. Phonons in ternary group-III nitride alloys. Physical Review B. 2000 Mar 1;61(9):6091.

100. Herring C, Vogt E. Transport and deformation-potential theory for many-valley semiconductors with anisotropic scattering. Physical review. 1956 Feb 1;101(3):944.

101. Bardeen J, Shockley W. Deformation potentials and mobilities in non-polar crystals. Physical review. 1950 Oct 1;80(1):72.

102. Demangeot F, Frandon J, Baules P, Natali F, Semond F, Massies J. Phonon deformation potentials in hexagonal GaN. Physical Review B. 2004 Apr 30;69(15):155215.

103. Gleize J, Renucci MA, Frandon J, Bellet-Amalric E, Daudin B. Phonon deformation potentials of wurtzite AlN. Journal of applied physics. 2003 Feb 15;93(4):2065-8.

104. Darakchieva V, Paskov PP, Paskova T, Birch J, Tungasmita S, Monemar B. Deformation potentials of the E 1 (TO) mode in AlN. Applied physics letters. 2002 Apr 1;80(13):2302-4.

105. Sarua A, Kuball M, Van Nostrand JE. Deformation potentials of the E 2 (high) phonon mode of AlN. Applied physics letters. 2002 Aug 19;81(8):1426-8.

106. Wagner JM, Bechstedt F. Phonon deformation potentials of α-GaN and-AlN: An ab initio calculation. Applied Physics Letters. 2000 Jul 17;77(3):346-8.

107. Sarua A, Kuball M, Van Nostrand JE. Phonon deformation potentials of the E 2 (high) phonon mode of Al x Ga 1− x N. Applied physics letters. 2004 Sep 20;85(12):2217-9.

108. Anastassakis E. Strains and optical phonons in material systems. Acta Physica Hungarica. 1994 Mar;74(1):83-105.

109. Rudloff D, Riemann T, Christen J, Liu QK, Kaschner A, Hoffmann A, Thomsen C, Vogeler K, Diesselberg M, Einfeldt S, Hommel D. Stress analysis of Al x Ga 1− x N films with microcracks. Applied physics letters. 2003 Jan 20;82(3):367-9.

110. Yang S, Miyagawa R, Miyake H, Hiramatsu K, Harima H. Raman scattering spectroscopy of residual stresses in epitaxial AlN films. Applied physics express. 2011 Feb 24;4(3):031001.

111. Xie MY, Tasnadi F, Abrikosov IA, Hultman L, Darakchieva V. Elastic constants, composition, and piezolectric polarization in In x Al 1− x N: From ab initio calculations to experimental implications for the applicability of Vegard's rule. Physical Review B. 2012 Oct 12;86(15):155310.

112. Wagner JM, Bechstedt F. Properties of strained wurtzite GaN and AlN: Ab initio studies. Physical Review B. 2002 Sep 10;66(11):115202.

113. Pankin DV, Smirnov MB, Davydov VY, Smirnov AN. Elastic strains effect on frequencies of delocalized polar phonons in AlN/GaN superlattices. InAIP Conference Proceedings 2016 Jun 17 (Vol. 1748, No. 1, p. 050007). AIP Publishing LLC.

114. Wang X, Yoshikawa A. Molecular beam epitaxy growth of GaN, AlN and InN. Progress in crystal growth and characterization of materials. 2004 Jan 1;48:42-103.

115. Tekippe VJ, Ramdas AK, Rodriguez S. Piezospectroscopic study of the Raman spectrum of α-quartz. Physical Review B. 1973 Jul 15;8(2):706.

116. Sievers AJ, Page JB. A generalized Lyddane-Sachs-Teller relation for solids and liquids. Infrared physics. 1991 Jan 1;32:425-33.

117. Varga BB. Coupling of plasmons to polar phonons in degenerate semiconductors. Physical Review. 1965 Mar 15;137(6A):A1896.

118. Gleize J, Renucci MA, Frandon J, Demangeot F. Anisotropy effects on polar optical phonons in wurtzite GaN/AlN superlattices. Physical Review B. 1999 Dec 15;60(23):15985.

119. Zheng J, Li E, Yan J, Cui Z, Ma D. Electronic and optical properties of GaN/AlN core–shell nanowires. Modern Physics Letters B. 2020 Jan 20;34(02):2050021.

120. Lyddane RH, Sachs RG, Teller E. On the polar vibrations of alkali halides. Physical Review. 1941 Apr 15;59(8):673.

121. Huang K. On the interaction between the radiation field and ionic crystals. Proceedings of the Royal Society of London. Series A. Mathematical and Physical Sciences. 1951 Sep 7;208(1094):352-65.

122. Sun L, Shi LC, Wang C. Investigations of Phonons in Zinc-Blende and Wurtzite by Raman Spectroscopy. Applications of Molecular Spectroscopy to Current Research in the Chemical and Biological Sciences, IntechOpen, London. 2016 Oct 5:23-40.

123. Bungaro C, Rapcewicz K, Bernholc J. Ab initio phonon dispersions of wurtzite AlN, GaN, and InN. Physical Review B. 2000 Mar 1;61(10):6720.

124. Thakur JS, Haddad D, Naik VM, Naik R, Auner GW, Lu H, Schaff WJ. A 1 (LO) phonon structure in degenerate InN semiconductor films. Physical Review B. 2005 Mar 9;71(11):115203.

125. Huang Y, Chen XD, Fung S, Beling CD, Ling CC, Wei ZF, Xu SJ, Zhi CY. The depth-profiled carrier concentration and scattering mechanism in undoped GaN film grown on sapphire. Journal of applied physics. 2004 Jul 15;96(2):1120-6.

126. Butcher KS, Tansley TL. InN, latest development and a review of the band-gap controversy. Superlattices and Microstructures. 2005 Jul 1;38(1):1-37.

127. Lazić S, Gallardo E, Calleja JM, Agullo-Rueda F, Grandal J, Sanchez-Garcia MA, Calleja E. Raman scattering by longitudinal optical phonons in InN nanocolumns grown on Si (1 1 1) and Si (0 0 1) substrates. Physica E: Low-dimensional Systems and Nanostructures. 2008 Apr 1;40(6):2087-90.

128. Robins LH, Horneber E, Sanford NA, Bertness KA, Brubaker MD, Schlager JB. Raman spectroscopy based measurements of carrier concentration in n-type GaN nanowires grown by plasma-assisted molecular beam epitaxy. Journal of Applied Physics. 2016 Sep 28;120(12):124313.

129. Park M, Cuomo JJ, Rodriguez BJ, Yang WC, Nemanich RJ, Ambacher O. Micro-Raman study of electronic properties of inversion domains in GaN-based lateral polarity heterostructures. Journal of applied physics. 2003 Jun 15;93(12):9542-7.

130. Wetzel C, Walukiewicz W, Haller EE, Ager III J, Grzegory I, Porowski S, Suski T. Carrier localization of as-grown n-type gallium nitride under large hydrostatic pressure. Physical Review B. 1996 Jan 15;53(3):1322.

131. Mao Z, Fu C, Pan X, Chen X, He H, Wang W, Zeng Y, Ye Z. Raman-based measurement of carrier concentration in n-type ZnO thin films under resonant conditions. Physics Letters A. 2020 Mar 9;384(7):126148.

132. Hon DT, Faust WL. Dielectric parameterization of Raman lineshapes for GaP with a plasma of charge carriers. Applied physics. 1973 May;1(5):241-56.

133. Irmer G, Röder C, Himcinschi C, Kortus J. Raman tensor elements and Faust-Henry coefficients of wurtzite-type α-GaN: How to overcome the dilemma of the sign of Faust-Henry coefficients in α-GaN?. Journal of Applied Physics. 2014 Dec 28;116(24):245702.

134. Ramkumar C, Prokofyeva T, Seon M, Holtz M, Choi K, Yun J, Nikishin SA, Temkin H. Micro-Raman Scattering From Hexagonal GaN, AlN, and Al x Ga 1− x} N Grown on (111) Oriented Silicon: Stress Mapping of Cracks. MRS Online Proceedings Library. 2001 Dec;693(1):39-43.

135. Montagnac G, Hao J, Pedreira-Segade U, Daniel I. Detection of nucleotides adsorbed onto clay by UV resonant raman spectroscopy: A step towards the search for biosignatures on Mars. Applied Clay Science. 2021 Jan 1;200:105824.

136. Hooijschuur JH, Verkaaik MF, Davies GR, Ariese F. Will Raman meet bacteria on Mars? An overview of the optimal Raman spectroscopic techniques for carotenoid biomarkers detection on mineral backgrounds. Netherlands Journal of Geosciences. 2016 Jun;95(2):141-51.

137. Rull F, Martinez-Frias J. Raman spectroscopy goes to Mars.

138. Tammann G. Über Anlauffarben von metallen. Zeitschrift für anorganische und allgemeine Chemie. 1920 May 21;111(1):78-89.

139. Johansson CH, Linde JO. Röntgenographische Bestimmung der Atomanordnung in den Mischkristallreihen Au□ Cu und Pd□ Cu. Annalen der Physik. 1925;383(21):439-60.

140. Bethe HA. Statistical theory of superlattices. Proceedings of the Royal Society of London. Series A-Mathematical and Physical Sciences. 1935 Jul 1;150(871):552-75.

141. Owen EA, Edmunds IG. An X-ray study of the superlattice in certain alloys. Proceedings of the Physical Society (1926-1948). 1938 May 2;50(3):389.

142. Inoue M, Mahutte CK, Wang S. Electronic Polarons in Alkali Halides. Physical Review B. 1970 Jul 15;2(2):539.

143. Esaki L, Tsu R. Superlattice and negative differential conductivity in semiconductors. IBM Journal of Research and Development. 1970 Jan;14(1):61-5.

144. Enslin J, Mehnke F, Mogilatenko A, Bellmann K, Guttmann M, Kuhn C, Rass J, Lobo-Ploch N, Wernicke T, Weyers M, Kneissl M. Metamorphic Al0. 5Ga0. 5N: Si on AlN/sapphire for the growth of UVB LEDs. Journal of Crystal Growth. 2017 Apr 15;464:185-9.

145. Xu H, Jiang JA, Dai Y, Cui M, Li KH, Ge X, Hoo J, Yan L, Guo S, Ning J, Sun H. Polarity control and nanoscale optical characterization of AlGaN-based multiple-quantum-wells for ultraviolet C emitters. ACS Applied Nano Materials. 2020 May 6;3(6):5335-42.

146. Biswas RK, Pati SK. Exploring a Superlattice of SnO-PbO: A New Material for Thermoelectric Applications. ACS Applied Energy Materials. 2021 Feb 16;4(3):2081-90.

147. Huang Y, Yin S, Huang Y, Zhang X, Zhang W, Jiang G, Zhu H, Wan C, Fu W. Graphene Oxide/Hexylamine Superlattice Field-Effect Biochemical Sensors. Advanced Functional Materials. 2021 Jun;31(23):2010563.

148. Balmain WH. XLVI. Observations on the formation of compounds of boron and silicon with nitrogen and certain metals. The London, Edinburgh, and Dublin Philosophical Magazine and Journal of Science. 1842 Oct 1;21(138):270-7.

149. Mallet JW. XIII.—On aluminum nitride, and the action of metallic aluminum upon sodium carbonate at high temperatures. Journal of the Chemical Society. 1876;30:349-54.

150. Fischer F, Schröter F. Über neue Metall-Stickstoff-Verbindungen und ihre Stabilität an der Hand des periodischen Systems. Berichte der deutschen chemischen Gesellschaft. 1910 Apr;43(2):1465-79.

151. Kaneko M, Hirai K, Kimoto T, Suda J. Multi-cycle RHEED oscillation under nitrogen supply in alternative source supply AlN growth by rf-MBE. Applied Physics Express. 2020 Jan 9;13(2):025503.

152. Ptak AJ. Growth kinetics and doping of gallium nitride grown by rf-plasma assisted molecular beam epitaxy. West Virginia University; 2001.

153. Alexeev AN, Chaly VP, Krasovitsky DM, Mamaev VV, Petrov SI, Sidorov VG. Features and benefits of III-N growth by ammonia-MBE and plasma assisted MBE. InJournal of Physics: Conference Series 2014 Oct 27 (Vol. 541, No. 1, p. 012030). IOP Publishing.

154. Grandjean N, Massies J, Vennegues P, Leroux M, Demangeot F, Renucci M, Frandon J. Molecular-beam epitaxy of gallium nitride on (0001) sapphire substrates using ammonia. Journal of applied physics. 1998 Feb 1;83(3):1379-83.

155. Fireman MN, Bonef B, Young EC, Nookala N, Belkin MA, Speck JS. Strain compensated superlattices on m-plane gallium nitride by ammonia molecular beam epitaxy. Journal of Applied Physics. 2017 Aug 21;122(7):075105.

156. Agrawal M, Dharmarasu N, Radhakrishnan K, Ravikiran L. Structural properties of GaN grown on AlGaN/AlN stress mitigating layers on 100-mm Si (111) by ammonia molecular beam epitaxy. Thin Solid Films. 2012 Oct 1;520(24):7109-14.

157. Budde M, Remmele T, Tschammer C, Feldl J, Franz P, Lähnemann J, Cheng Z, Hanke M, Ramsteiner M, Albrecht M, Bierwagen O. Plasma-assisted molecular beam epitaxy of NiO on GaN (00.1). Journal of Applied Physics. 2020 Jan 7;127(1):015306.

158. Diez S, Mohanty S, Kurdak C, Ahmadi E. Record high electron mobility and low sheet resistance on scaled-channel N-polar GaN/AlN heterostructures grown on on-axis N-polar GaN substrates by plasma-assisted molecular beam epitaxy. Applied Physics Letters. 2020 Jul 27;117(4):042102.

159. Pérez-Caro M, Ramírez-López M, Hernández-Méndez S, Rodríguez BA, Casallas-Moreno YL, Gallardo-Hernández S, López-López M. Optical studies of nitrogen plasma for molecular beam epitaxy of InN. Journal of Applied Physics. 2020 Dec 7;128(21):215304.

160. McSkimming BM. High Active Nitrogen Flux Growth of (Indium) Gallium Nitride by Plasma Assisted Molecular Beam Epitaxy. University of California, Santa Barbara; 2015.

161. Ahmeda, K. *et al.* The role of SiN/GaN cap interface charge and GaN cap layer to achieve enhancement mode GaN MIS-HEMT operation. *Microelectronics Reliability* **115**, (2020).

162. Smallman RE, Ngan AH. Chapter 10-Surfaces, grain boundaries and interfaces. Modern physical metallurgy, Eighth Edition edn. Butterworth-Heinemann, Oxford. 2014:415-42.

163. Pandey A, Shin WJ, Gim J, Hovden R, Mi Z. High-efficiency AlGaN/GaN/AlGaN tunnel junction ultraviolet light-emitting diodes. Photonics Research. 2020 Mar 1;8(3):331-7.

164. Bishop SG, Hadden JP, Alzahrani FD, Hekmati R, Huffaker DL, Langbein WW, Bennett AJ. Room-temperature quantum emitter in aluminum nitride. ACS photonics. 2020 Jun 11;7(7):1636-41.

165. Lee HP, Perozek J, Rosario LD, Bayram C. Investigation of AlGaN/GaN high electron mobility transistor structures on 200-mm silicon (111) substrates employing different buffer layer configurations. Scientific reports. 2016 Nov 21;6(1):1-0.

166. Kim J, Kim Y, Oh S, Choi J, Lee DH, Cho K, Lee S, Ahn CH. A 20-W Wide Bandwidth GaN HEMT Power Amplifier for VHF/UHF Applications. IEEE transactions on industrial electronics. 2019 Dec 24;67(12):10905-10.

167. Li D, Jiang K, Sun X, Guo C. AlGaN photonics: recent advances in materials and ultraviolet devices. Advances in Optics and Photonics. 2018 Mar 31;10(1):43-110.

168. Knauer A, Kolbe T, Rass J, Cho HK, Netzel C, Hagedorn S, Lobo-Ploch N, Ruschel J, Glaab J, Einfeldt S, Weyers M. High power UVB light emitting diodes with optimized n-AlGaN contact layers. Japanese Journal of Applied Physics. 2019 Apr 16;58(SC):SCCC02.

169. Würtele MA, Kolbe T, Lipsz M, Külberg A, Weyers M, Kneissl M, Jekel MJ. Application of GaN-based ultraviolet-C light emitting diodes–UV LEDs–for water disinfection. Water research. 2011 Jan 1;45(3):1481-9.

170. Islam SM, Protasenko V, Lee K, Rouvimov S, Verma J, Xing H, Jena D. Deep-UV emission at 219 nm from ultrathin MBE GaN/AlN quantum heterostructures. Applied Physics Letters. 2017 Aug 28;111(9):091104.

171. Zhao S, Connie AT, Dastjerdi MH, Kong XH, Wang Q, Djavid M, Sadaf S, Liu XD, Shih I, Guo H, Mi Z. Aluminum nitride nanowire light emitting diodes: Breaking the fundamental bottleneck of deep ultraviolet light sources. Scientific reports. 2015 Feb 16;5(1):1-5.

172. Gorczyca I, Suski T, Strak P, Staszczak G, Christensen NE. Band gap engineering of In (Ga) N/GaN short period superlattices. Scientific reports. 2017 Nov 22;7(1):1-9.

173. Arita M, Le Roux F, Holmes MJ, Kako S, Arakawa Y. Ultraclean single photon emission from a GaN quantum dot. Nano letters. 2017 May 10;17(5):2902-7.

174. Clinton EA, Engel Z, Vadiee E, Carpenter JV, Holman ZC, Doolittle WA. Ultra-wide-bandgap AlGaN homojunction tunnel diodes with negative differential resistance. Applied Physics Letters. 2019 Aug 19;115(8):082104.

175. Shuvo AA, Islam MR, Hasan MT. Ultrawide-bandgap AlGaN-based HEMTs for high-power switching. Journal of Computational Electronics. 2020 Sep;19(3):1100-6.

176. Nakamura S, Senoh M, Iwasa N, Nagahama SI, Yamada T, Mukai T. Superbright green InGaN single-quantum-well-structure light-emitting diodes. Japanese Journal of Applied Physics. 1995 Oct;34(10B):L1332.

177. Bhuiyan AG, Hashimoto A, Yamamoto A. Indium nitride (InN): A review on growth, characterization, and properties. Journal of applied physics. 2003 Sep 1;94(5):2779-808.

178. Chaudhuri R, Bader SJ, Chen Z, Muller D, Xing HG, Jena D. Molecular Beam Epitaxy Growth of Large-Area GaN/AlN 2D Hole Gas Heterostructures. physica status solidi (b). 2020 Apr;257(4):1900567.

179. Herman MA, Richter W, Sitter H. Molecular beam epitaxy. InEpitaxy 2004 (pp. 131-170). Springer, Berlin, Heidelberg.

180. Fox M, Ispasoiu R. Quantum wells, superlattices, and band-gap engineering. in Springer Handbook of Electronic and Photonic Materials, 2017.

181. Gogneau N, Jamond N, Chrétien P, Houzé F, Lefeuvre E, Tchernycheva M. From single III-nitride nanowires to piezoelectric generators: New route for powering nomad electronics. Semiconductor Science and Technology. 2016 Sep 15;31(10):103002.

182. Shieh CC, Cui XY, Delley B, Stampfl C. Built-in electric fields and valence band offsets in InN/GaN (0001) superlattices: First-principles investigations. Journal of Applied Physics. 2011 Apr 15;109(8):083721.

183. Pankin DV, Smirnov MB. The applicability of Raman spectroscopy for estimation of interfaces thickness in the AlN/GaN superlattices. St. Petersburg Polytechnical University Journal: Physics and Mathematics. 2016 Jun 1;2(2):83-90.

184. Gorczyca I, Suski T, Christensen NE, Svane A. Band structure and quantum confined stark effect in InN/GaN superlattices. Crystal growth & design. 2012 Jul 3;12(7):3521-5.

185. Huang Q, Deng J, Li X, Zhang G, Xu F. Experimental investigation on thermally induced aluminum nitride based flexible composite phase change material for battery thermal management. Journal of Energy Storage. 2020 Dec 1;32:101755.

186. Paskov PP, Monemar B, Paskova T, Kamiyama S, Amano H, Akasaki I. Photoluminescence study of near-surface GaN/AlN superlattices. InGallium Nitride Materials and Devices III 2008 Feb 28 (Vol. 6894, p. 68940G). International Society for Optics and Photonics.

187. Jabbar HD, Fakhri MA, AbdulRazzaq MJ. Gallium Nitride–Based Photodiode: A review. Materials Today: Proceedings. 2021 Feb 10.

188. Cheng P, Wang Q, Li W, Jia Y, Liu Z, Feng C, Jiang L, Xiao H, Wang X. A Broadband Asymmetrical GaN MMIC Doherty Power Amplifier with Compact Size for 5G Communications. Electronics. 2021 Jan;10(3):311.

189. Rytov S. Electromagnetic properties of a finely stratified medium. Soviet Physics JEPT. 1956;2:466-75.

190. Moram MA, Vickers ME. X-ray diffraction of III-nitrides. Reports on progress in physics. 2009 Feb 20;72(3):036502.

191. Shen XQ, Takahashi T, Ide T, Shimizu M. Mechanisms of the micro-crack generation in an ultra-thin AlN/GaN superlattice structure grown on Si (110) substrates by metalorganic chemical vapor deposition. Journal of Applied Physics. 2015 Sep 28;118(12):125307.

192. Tripathy S, Chua SJ, Chen P, Miao ZL. Micro-Raman investigation of strain in GaN and Al x Ga 1− x N/GaN heterostructures grown on Si (111). Journal of Applied Physics. 2002 Oct 1;92(7):3503-10.

193. Soh CB, Chow SY, Tripathy S, Chua SJ. Reduction of V-pit and threading dislocation density in InGaN/GaN heterostructures grown on cracked AlGaN templates. Journal of Physics: Condensed Matter. 2008 Feb 8;20(9):095210.

194. Damen TC, Porto SP, Tell B. Raman effect in zinc oxide. Physical Review. 1966 Feb 11;142(2):570.

195. Thomas JM. The birth of X-ray crystallography. Nature. 2012 Nov;491(7423):186-7.

196. Holbrook RD, Galyean AA, Gorham JM, Herzing A, Pettibone J. Overview of nanomaterial characterization and metrology. InFrontiers of Nanoscience 2015 Jan 1 (Vol. 8, pp. 47-87). Elsevier.

197. Bellet-Amalric E, Amstatt B, Daudin B. AlN/GaN superlattices: strain relaxation. physica status solidi c. 2006 Jun;3(6):1691-4.

198. Thapa J, Liu B, Woodruff SD, Chorpening BT, Buric MP. Raman scattering in single-crystal sapphire at elevated temperatures. Applied optics. 2017 Nov 1;56(31):8598-606.

199. Davydov VY, Averkiev NS, Goncharuk IN, Nelson DK, Nikitina IP, Polkovnikov AS, Smirnov AN, Jacobson MA, Semchinova OK. Raman and photoluminescence studies of biaxial strain in GaN epitaxial layers grown on 6H–SiC. Journal of applied physics. 1997 Nov 15;82(10):5097-102.

200. Yamaguchi M, Yagi T, Azuhata T, Sota T, Suzuki K, Chichibu S, Nakamura S. Brillouin scattering study of gallium nitride: elastic stiffness constants. Journal of Physics. Condensed Matter. 1997 Jan 6;9(1):241-8.

201. Deger C, Born E, Angerer H, Ambacher O, Stutzmann M, Hornsteiner J, Riha E, Fischerauer G. Sound velocity of Al x Ga 1− x N thin films obtained by surface acoustic-wave measurements. Applied Physics Letters. 1998 May 11;72(19):2400-2.

202. Shimada K, Sota T, Suzuki K. First-principles study on electronic and elastic properties of BN, AlN, and GaN. Journal of Applied Physics. 1998 Nov 1;84(9):4951-8.

203. Reeber RR, Wang K. High temperature elastic constant prediction of some group III-nitrides. Materials Research Society Internet Journal of Nitride Semiconductor Research. 2001;6.

204. Deguchi T, Ichiryu D, Toshikawa K, Sekiguchi K, Sota T, Matsuo R, Azuhata T, Yamaguchi M, Yagi T, Chichibu S, Nakamura S. Structural and vibrational properties of GaN. Journal of applied physics. 1999 Aug 15;86(4):1860-6.

205. Kim K, Lambrecht WR, Segall B. Electronic structure of GaN with strain and phonon distortions. Physical Review B. 1994 Jul 15;50(3):1502.

206. Kolomys O, Tsykaniuk B, Strelchuk V, Naumov A, Kladko V, Mazur YI, Ware ME, Li S, Kuchuk A, Maidaniuk Y, Benamara M. Optical and structural study of deformation states in the GaN/AlN superlattices. Journal of Applied Physics. 2017 Oct 21;122(15):155302.

207. Ackland GJ. High-pressure phases of group IV and III-V semiconductors. Reports on Progress in Physics. 2001;64(4):483-516.

208. Tsubouchi K, Mikoshiba N. Zero-temperature-coefficient SAW devices on AlN epitaxial films. IEEE Transactions on Sonics Ultrasonics. 1985 Sep;32:634-44.

209. Ruiz E, Alvarez S, Alemany P. Electronic structure and properties of AlN. Physical Review B. 1994 Mar 15;49(11):7115.

210. Savastenko VA, Sheleg AU. Study of the elastic properties of gallium nitride. Physica status solidi (a). 1978 Aug 16;48(2):K135-9.

211. Darakchieva V, Valcheva E, Paskov PP, Schubert M, Paskova T, Monemar B, Amano H, Akasaki I. Phonon mode behavior in strained wurtzite Al N⁄Ga N superlattices. Physical Review B. 2005 Mar 29;71(11):115329.

212. Bansal A, Wang K, Lundh JS, Choi S, Redwing JM. Effect of Ge doping on growth stress and conductivity in AlxGa1-xN. Applied Physics Letters. 2019 Apr 8;114(14):142101.

213. Christy, D., Watanabe, A. & Egawa, T. Influence of strain induced by AlN nucleation layer on the electrical properties of AlGaN/GaN heterostructures on Si(111) substrate. AIP Advances. 2014; (4).